Simulation of mouse tibia resistance with and without bone tumor

Benjamin Delpuech

N°d'ordre NNT : xxx

THESE de DOCTORAT DE L'UNIVERSITE DE LYON
opérée au sein de
l'Université Claude Bernard Lyon 1

Ecole Doctorale N° 162
MEGA

Spécialité de doctorat : Biomécanique
Discipline : Mécanique

Soutenue publiquement le 26/09/2019, par :
Benjamin DELPUECH

Simulation de la résistance du tibia de souris avec et sans tumeur osseuse

---

Devant le jury composé de :

LAPORTE, Sébastien Professeur des Universités Arts et Métiers ParisTech

PAHR, Dieter Professeur, Université Technique de Vienne (Autriche)
BOUSSON, Valérie Professeure des Universités Praticien Hospitalier Université Paris 7, Hôpital Lariboisière (APHP)
LAPORTE, Sébastien Professeur des Universités Arts et Métiers ParisTech
CONFAVREUX, Cyrille Professeur des Universités Praticien Hospitalier Université Lyon 1, Hôpital Lyon Sud (HCL)

MITTON, David Directeur de Recherche IFSTTAR
FOLLET Hélène Chargée de Recherche INSERM

I. Abstract

The skeleton, being highly vascularized, is one of the most commonly affected site by metastatic. The development of bone metastases weakens the bone and can cause pathological fractures. However, the prediction of such fractures is difficult and there is a clinical need for better risk fracture assessment.

One possibility for creating a more powerful diagnostic tool would be finite element analyses (FEA). Studies have shown that patient-specific FEA is able to surpass the expertise of clinicians in the case of *ex vivo* studies with mechanically induced bone defects.

However, research on metastatic bone is hard to put in place as samples are rare. In order to overcome the difficulty, the mouse has been used as a skeletal model in several cases, including the bone strength with *ex vivo* metastases. Thus, in order to study the involvement of metastatic tissue in the overall bone resistance of real samples, we used this animal model to obtain bones with tumor.

Our goal was twofold: first, to quantify the contribution of the mechanical properties of metastasis in the overall bone strength. Secondly, to see if a simpler model than that proposed in the literature (based on purely elastic rather than elastoplastic properties) could improve the prediction of fractures.

The results obtained with our heterogeneous models (not taking tumor into account) showed a good consistency with the literature. The correlation between all the heterogeneous models (n = 43 legs) simulations and experimental fractures were R^2=0.65 and Root Mean Square Error = 3.3.

Then, the model taking into account the properties of the tumors did not improve the fracture prediction. The average differences between models taking tumor into account and experiments being of 30 ± 21% (n = 11 tumor limbs) compared to 12 ± 9% (n = 43 limbs) when using a heterogeneous model.

In addition, the specific model (taking into account the modulus of the tumors) being more difficult to obtain than the heterogeneous model (not requiring segmentation between bone and tumor), the first one does not seem to be useful in the prediction of mice tibia strength with bone lysis.

Finally, a detection criterion based on the difference between global and local ultimate load classifies the majority of the mechanical instabilities observed in this study (sensitivity of 85% and specificity of 100%). Another criterion, based on the ratio between individual weights and the local ultimate load predicted using FEA, correctly identifies all cases (100% sensitivity and specificity).

This result could be of great help for clinicians in patient care in the case of long bone with metastases.

Of course, before that, the road ahead is long, this result having to be clinically confirmed first (possibly through the study of a retrospective cohort, as has already been done in other studies).

This study has just been initiated in the case of the project MEKANOS (metacentric study in France) led by Professor Cyrille Confavreux (rheumatologist).

II. Introduction

Cancer describes a group of diseases that have in common unregulated cell growth caused by genetic mutation. As such, it has a genetic origin. The risk of developing cancer is increased by environmental factors (smoking, obesity, environmental pollutants…). It includes the malignant subset of neoplasms: a group of cells that undergo unregulated growth and form a mass of tissue: tumor. One of the principal characteristic of cancer is its possibility to migrate to other part of the body through metastases (migrating tumor).

The skeleton is the third most common organ to be affected by metastatic cancer (Du et al., 2010). Bone metastasis is not a random event, but an organized process that as several steps as tumor cells migration and survival in blood circulation transfer from the blood to the adjacent tissue, implantation and growth *in situ* and vascularization (Wong and Pavlakis, 2011). Most of the time, metastasis develop were the red marrow is. Its effect is of three types, “lytic”, “blastic” and “mixed”, the three terms referring to its radiological aspect (Wong and Pavlakis, 2011).

The occurring of metastatic bone pathological fracture in patients is difficult to predict, and far from automatic. In an 1800 patients study, a low occurrence (8%) of fracture in bone metastatic disease patients was showed, where 53% of this occurrence was among breast cancer patients (Higinbotham and Marcove, 1965). In another study, considering only breast cancer patients, incidence of pathologic fractures was way higher, reaching 57%. 29% of these fractures occurred in ribs and 9% for both vertebrae and in long bones (Scheid *et al.*, 1986). Finally, in a study gathering 37 prostate cancer patients with blastic lesions, all presented a pathological fracture (Wedin and Bauer, 2005).
This highlights that every type of metastatic lesions is problematic and needs particular attention from clinicians.

Indications for surgery vary among patients and surgeons (Attar *et al.*, 2012). Anyhow, most clinicians agree that the decision to make a patient undergo surgery depends on several aspects as location of tumor, expected morbidity, if the bone integrity is at risk, and patient expectation, among others (Attar *et al.*, 2012).

Metastases bone stability is difficult to quantify, even for experienced surgeon (Attar *et al.*, 2012).
In 1982, Mirels suggested a scoring system to predict failure risk in long bones (Mirels, 2003). It was developed based on a retrospective study on 78 metastatic long bone lesions. It lies on four criteria: lesion site, size, degree of sclerosis/lysis and pain (Mirels, 2003) Over time, Mirels’ score became a widely used and studied tool (Van der Linden *et al.*, 2004).

In order to test and improve Mirels’ score if necessary, Van der Linden led a retrospective study including 102 patients with metastases femora of whom 14 suffered a fracture during follow-up. Each patient lesion was rated using Mirels’s score. Among the considered cases, 84 (82%) would have been surgically over treated while 13% of the lesions without fracture were detected at low risk (Van der Linden *et al.*, 2004). Implementing a threshold on metastases axial cortical involvement reduced over-treatment to 42% (Van der Linden *et al.*, 2004).

Still, as surgical over treatment has a large impact on quality of life in patients who have a limited life expectancy (Van der Linden *et al.*, 2004), a more accurate failure risk predictor would be necessary.

Patient-specific finite element analysis (FEA) was widely studied in order to assess failure risk in osteoporosis, showing good results (among others: (Bessho *et al.*, 2009; Duchemin *et al.*, 2008; Keyak *et al.*, 2013; Kopperdahl *et al.*, 2014; Zapata *et al.*, 2017; Zysset *et al.*, 2013)).
As it shows good potential that is not met by other trails, it was more recently studied as a potential tool to improve failure prediction of metastatic bones (Benca et al., 2019, 2017; Derikx et al., 2012; Eggermont et al., 2018; Goodheart et al., 2015; Keyak et al., 2005; Tanck et al., 2009).
Ultimately, it was shown, in an *ex vivo* study with mechanically induced metastases, that FEA in this condition is out performing clinical experts (Kendall's tau of 0.78 for FEA against 0.5 ±0.03 in average for 6 clinical experts (Derikx *et al.*, 2012)).
However, these studies suffered a great limitation: comparison was based on an *ex vivo* study with mechanically induced defect, and there was no way to tell if the same results would be found on real patients.
That limitation was recently overcome, when a clinical retrospective study was led by the same team (Eggermont *et al.*, 2018). In this study, 39 patients with non-fractured femoral metastatic lesion were included. Each patient was followed for six month, until femur fracture or death (which ever occurred first) (Eggermont *et al.*, 2018).
Results agreed with previous studies, showing a better prediction with FE models (sensitivity (correctly identifying clinical fractures) of 89% versus 0% to 33% for clinical assessments). Even though the difference is incommensurate with previous cited result, it is to be noted that clinician scored a higher specificity than FE models (specificity (correctly identify cases that do not fracture) was 79% for the FE models versus 84% to 95% for clinical assessments), leaving room for improvement.

However, studies on metastatic bone are difficult to undertake, as samples are uncommon.
Mice has been widely used as a skeletal model (as example :Fritton *et al.* 2005), preclinical studies (as example Slosky, Largent-Milnes, and Vanderah 2015) and even biomechanical cancer study (Mann *et al.*, 2008) to create samples that are uncommon (as tumoral bones) and study parameters that are not possible in patients for various reasons.

To overcome this sample unavailability of tumoral bone, mouse was used as an animal model in this study.

Our aim was to find a more sensitive failure prediction tool on our animal model than the ones already existing, in order to provide new ways to improve failure prediction in clinical practice.

III. State of the art

1. *The Human body*

The organization of the body is often discussed in terms of six distinct levels of increasing complexity, from the smallest chemical building blocks to a unique human organism. It goes from the molecular level to the organism level, covering the cellular level as well as the organ level. The aim of the present thesis being to study the strength of a whole long bone, mostly organ level will be furtherly discussed.

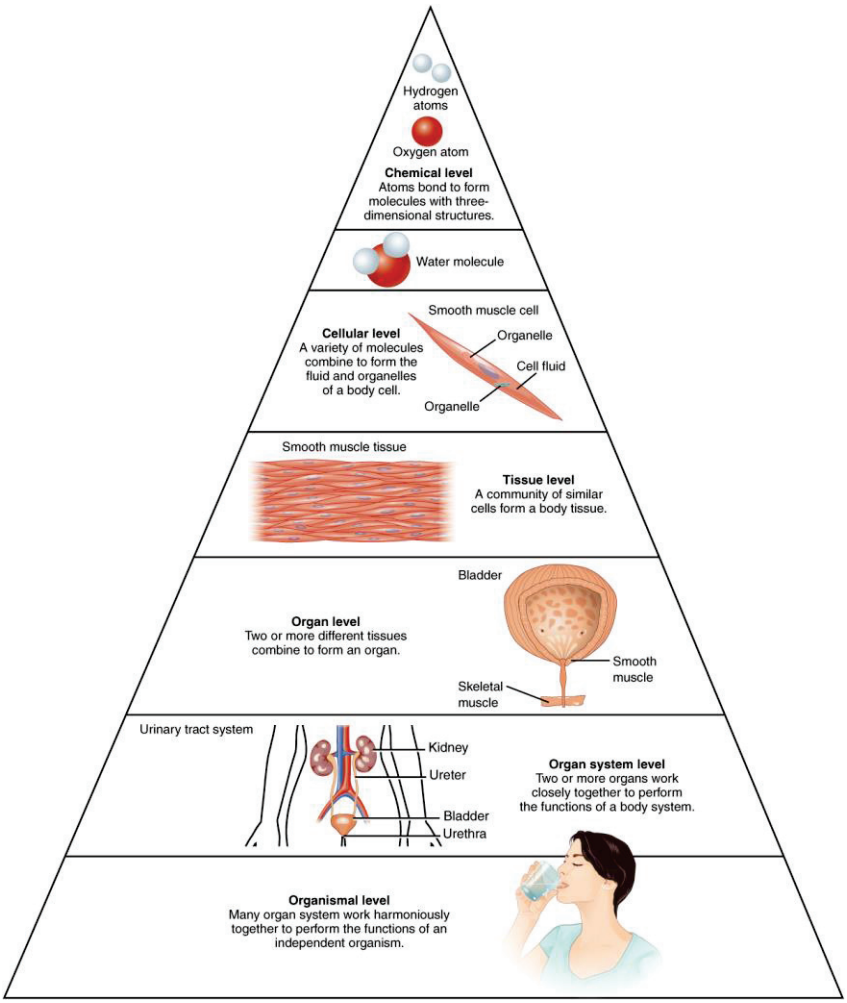

Figure 1: Levels of Structural Organization of the Human Body (https://courses.lumenlearning.com/nemcc-ap/chapter/overview-of-anatomy-and-physiology/)

From a mechanical point of view, Human tissues are separated into two classes: hard tissue and soft tissue.
While hard tissues are defined as mineralized tissues that have a firm intercellular matrix (as bone, tooth enamel, dentin, and cementum), soft tissues are defined as the tissues that connect, support or surround hard tissues (as tendons, ligaments, fascia, skin, fibrous tissues, fat, and synovial membranes).

2. *The Skeleton*

The human adult skeleton is composed of 206 bones ("Anatomy and Physiology | Simple Book Production,"). They are dense connective tissues and compose most of the adult skeleton. In the areas where the bones move (as joints) cartilage, a semi-rigid connective tissue provides smooth surfaces in order to enable movement between bones.

The skeleton function is five folded. Two of these functions could be categorized as cellular function, whereas the three others as organism level function.
On a cellular level, the skeleton (thought bone marrow) carries out the production of blood cells (hematopoiesis) and allows the storage and release of minerals and fat. On the organism level, it provides a support for the body as well as a protection for its organs. Finally, it facilitates movement, as it allows muscle insertion (via tendons) thus enabling movement.

a. Bones

Bones composing the human skeleton (as well as all vertebrate) are divided into five types depending on their aspect ratio (representing the relation between height and width):

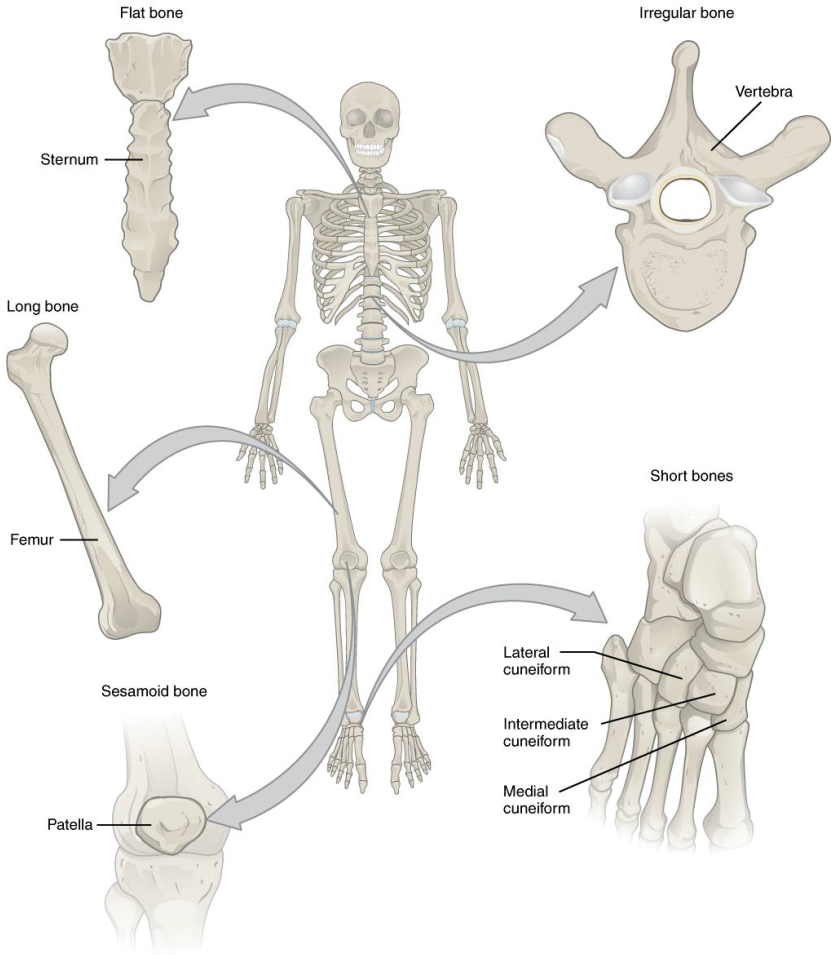

Figure 2: Illustration of the different bones found in the human body (https://courses.lumenlearning.com/nemcc-ap/chapter/bone-classification/)

- **Long bones**, categorizing the cylindrical in shape bones, longer than wide. They are mainly found in upper and lower limbs (humerus, ulna, radius for arms, femur, tibia, fibula for legs) and in the hands and feet (respectively metacarpals, phalanges and metatarsals, phalanges). Long bones function as levers, they move when muscles contract.
- **Short bones**, cubic in shape, approximately equal in length width and thickness. Only found in the carpals of the wrists and the tarsals of the ankles. They provide support and stability as well as limited movement.
- **Flat bone**, typically thin and often curved. Examples cover, non-exhaustively, the cranial skull, the sternum and the ribs. Their aim is to serve as attachment point, usually along with protecting internal organs.
- **Sesamoid bone**, small round bones. Formed in tendons, where a great deal of pressure is generated in a joint. Their numbers vary depending on the person. The only one found in common with every person being the patella. Their function is to protect the tendons, helping them to withstand compressive forces.
- **Irregular bone**. The only ones not characterized by their shape. It tends to have complex shapes, like vertebrae protecting the spinal cord. Many facial bones, as the ones containing sinuses, are classified as irregular bones.

As long bones allow the best visualization of its different components, it will be taken as an example for the rest of this section.
A long bone can be divided into two parts: the diaphysis and the epiphysis.
The diaphysis is the tubular shaft that is between the proximal and distal ends of the bone. The hollow region of the diaphysis is filled with yellow marrow. The walls of the tube forming the diaphysis are composed of cortical bone (hard bone), described in the following part.
The wider ends of the bone are called epiphysis. The epiphysis are filled with trabecular bone (spongy bone), described in the following part.

Bone contains a relatively small number of cells entrenched in matrix of collagen fibers. Three different types of cells are found in bone tissue: osteoblasts, osteocytes and osteoclasts (“Anatomy and Physiology | Simple Book Production”). Their respective roles will be furtherly discussed in the section “bone modeling”.

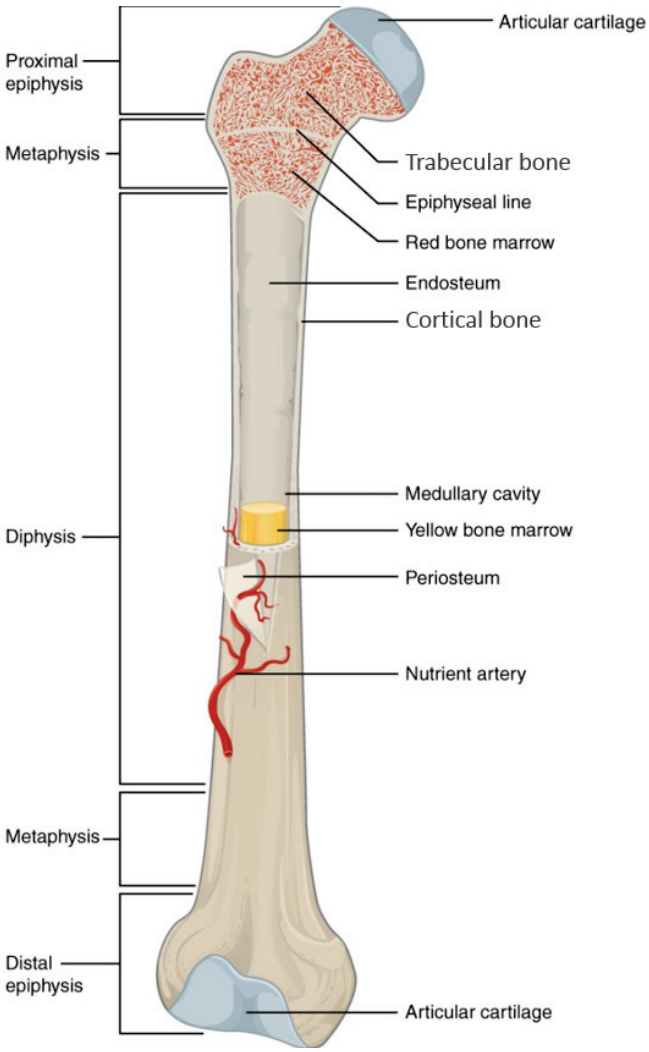

Figure 3: Illustration of a component of a long bone (https://courses.lumenlearning.com/nemcc-ap/chapter/bone-classification/)

3. *Cortical and trabecular bone*

Most bones contain cortical (compact) and trabecular (or cancellous) bone. Their distribution depends on the whole bone function.

a. Cortical bone

Cortical bone is the denser, the stronger of the two types. Its aim is to support the body weight and protect the weaker type and it is therefore found on the outlaying part of bones. Nevertheless, as one of the role of bones is to product blood cells (through bone marrow), it has to let veins go through, making it a pierced hollow material (Figure 4).

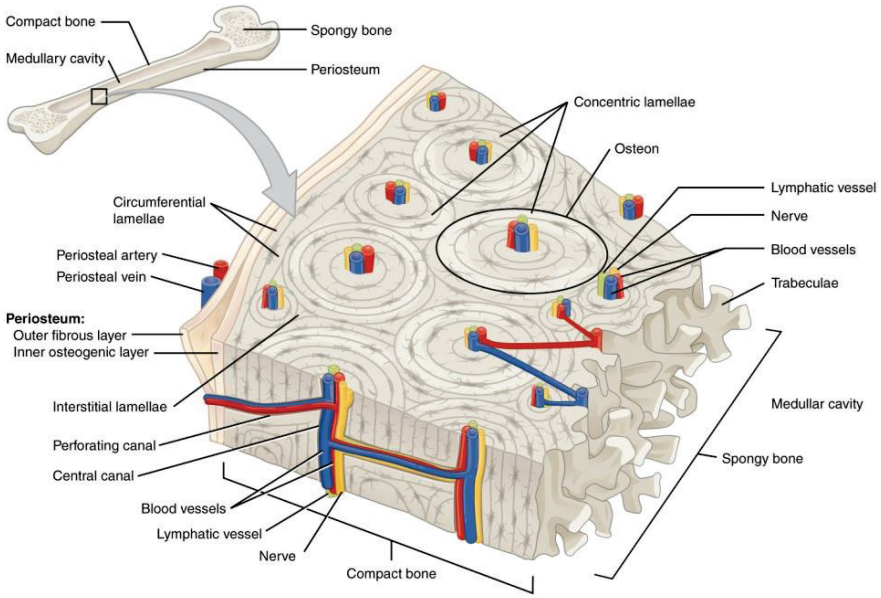

Figure 4: Representation of cortical bone (https://courses.lumenlearning.com/nemcc-ap/chapter/bone-classification/)

At the microscopic scale, each unit of compact bone is called osteon, forming the Haversian system. These osteons are formed of concentric rings composed of calcified matrix called lamellae.

b. Trabecular bone

Unlike compact bone, trabecular bone is arranged in a lattice-like network of matrix rods and plates called trabeculae. In long bones, its arrangement is not random, in fact each trabecula forms along lines of stress to provide strength to the bone. This arrangement allows making bone lighter, bringing balance to dense and heavy compact bone, facilitating muscle action and thus movement of the skeleton (Figure 5).
Finally, spaces between trabeculae contain red marrow, where blood cells formation occurs.

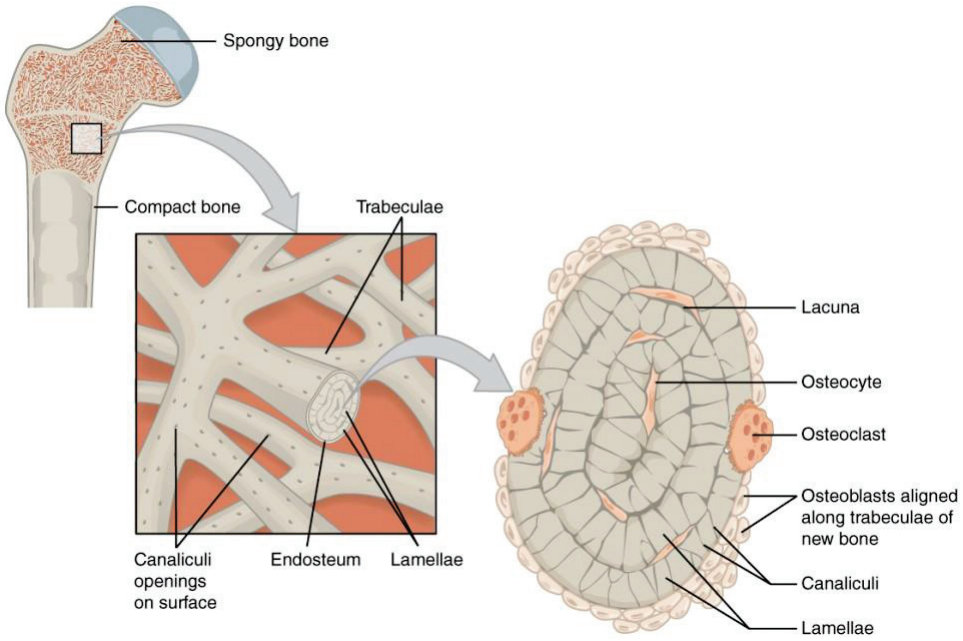

Figure 5: Representation of trabecular bone (https://courses.lumenlearning.com/nemcc-ap/chapter/bone-classification/)

c. Bone remodeling

During life of all vertebrate, bone rearranges itself, in order to be able to withstand different stresses of daily life. Remodeling can be triggered by injury, exercises… This process allows resorption of old or damaged bone, to be replaced at the same place by new bone.

To understand bone remodeling, knowledge of the cell types found in bone is needed:

- Osteoclasts, bone-resorbing cells. Osteoclasts are large, multinucleate cells that are descended from stem cells in the bone marrow.
- Osteoblasts, bone-forming cells. These cells, found on bone surface are connective tissue cells that can be stimulated to proliferate and differentiate as osteocytes.
- Osteocytes, bone cells. Osteocytes manufacture collagen and other substances that make up the bone extracellular matrix. They are found enclosed in bone.

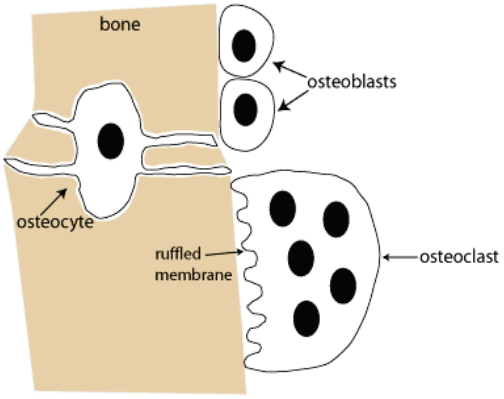

Remodeling cycle consists of three consecutive phases: resorption, reversal, and formation.

Resorption begins with the migration of mononuclear pre-osteoclasts to bone surface where they merge to form multinucleated osteoclasts.

Figure 6: Bone cells illustration (https://courses.washington.edu/conj/bess/bone/bone2.html)

The reversal phase is when mononuclear cells appear on bone surface. These cells prepare bone surface for the formation phase and signal for osteoblast differentiation and migration (“Bone Remodeling,”).
The formation phase follows when the signaled osteoblasts cells lay in bone until the resorbed bone is completely replaced by new bone (“Bone Remodeling,”).
Length of these different phases differs from about two weeks for resorption, four to five weeks for reversal and can continue for four months for the formation (“Bone Remodeling,”).
It is known that, even without exercises or injuries, 5 to 10% of the skeleton is renewed annually (“Bone Remodeling,”).

4. *Cancer*

Cancer describes a group of diseases that have in common unregulated cell growth caused by genetic mutation (“Boundless Anatomy and Physiology | Simple Book Publishing,”).
As such, it has a genetic origin. The risk of developing cancer is increased by environmental factors (smoking, obesity, environmental pollutants…).
It includes the malignant subset of neoplasms: a group of cells that undergo unregulated growth and form a mass of tissue: tumor.
One of the principal characteristics of cancer is its possibility to migrate to other part of the body through metastases (migrating tumor).
Treatments depend on tumor type, location and patients, but usually include surgery, chemotherapy (administration of toxin targeting quickly dividing cells) and radiotherapy (bombarding specific target with ionizing radiation) (“Boundless Anatomy and Physiology | Simple Book Publishing,”).

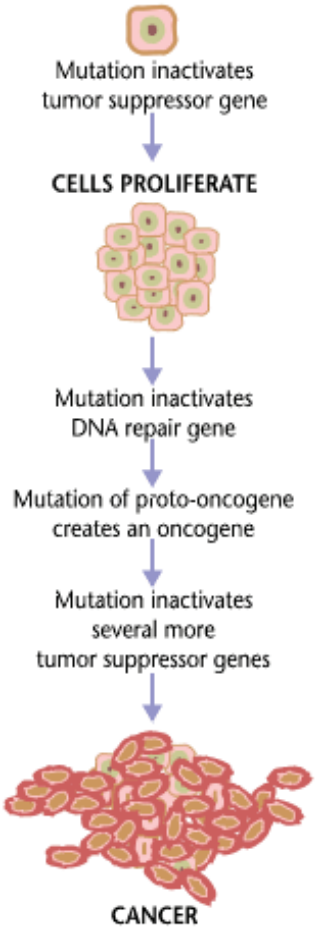

Figure 7: Pathway of cancer development (https://courses.lumenlearning.com/boundless-ap/chapter/overview-of-cancer/)

a. Bone metastasis

The skeleton is one of the three most common organ to be affected by metastatic cancer (Du et al., 2010). This is due, firstly, to bone high vascularization, secondly, to its dysregulation in acidity, oxygen and calcium level, making a good implantation site. Finally, bone harbors many growth factors, which are vital to cancer cell survival and proliferation, making it a fertile land for metastases. It is estimated that patients develop metastatic bone disease in 80% of cases of both breast and prostate cancers (Coleman, 1997).

Bone metastasis is not a random event, but an organized process that as several steps as tumor cells migration and survival in blood circulation transfer from the blood to the adjacent tissue, implantation and growth *in situ* and vascularization (Wong and Pavlakis, 2011).

Most of the time, metastasis develops where the red marrow is. Its effect is of three types, “lytic”, “blastic” and “mixed”. In lytic lesions, bone resorption predominates, and there is little bone formation so bone destruction happens and the lesions have a lytic appearance (Wong and Pavlakis, 2011). Lytic lesions are most common in myeloma, melanoma, and breast cancer (Coleman, 1997). Whereas, in blastic lesion, osteoblastic activity is increased, giving the lesion a blastic (or sclerotic) aspect (Coleman, 1997). Blastic lesion ensues breast and lung metastases, among others (Coleman, 1997). Still, this classification is simplistic and both lesion types lead to an acceleration of both phenomena. For instance, it was shown that despite the blastic nature of prostate metastases, the value of resorption markers in this lesion was as high as those find for breast metastases lytic lesion (Urwin *et al.*, 1985).
In mixed lesions, both osteoblastic and osteoclastic phenomenons are highly activated, giving evidence of increased osteoclast activity and resorption cavities (Urwin *et al.*, 1985). Therefore, in all types of metastatic lesions, both osteoblastic and osteolytic phenomena are boosted, breaking the balance between bone resorption and formation. The type of lesion is then defined by which phenomenon has taken over the other. This increased osteoclastic activity weakens the bone and thus reduces its load bearing capabilities either way. In lytic lesion, bone weakens due to its resorption. In blastic lesion, it becomes increasingly brittle and prone to fracture, and in mixed lesion, it is too disorganized to suit its purpose. It results in all cases firstly in trabecular disruption and micro fractures. A total loss of bone integrity follows (Coleman, 1997).
Bone metastases develop most commonly in axial skeleton (Figure 8). However, long bone fracture causes more disability.
The occurring of metastatic bone pathological fracture in patients is hard to predict, and far from automatic.
In an 1800 patients study, including all metastatic cancer in bone cases from 1931 to 1965 observed in Memorial Sloan-Katering Cancer Center (New-York), a low occurrence (8%) of fracture in bone metastatic disease patients was showed. Fifty three percent of this occurrence was among breast cancer patients (Higinbotham and Marcove, 1965).
In another study (Scheid et al., 1986), considering only breast cancer patients, incidence of pathologic fractures was way higher, reaching 57%. This study included 195 patients presenting bone metastases (48% osteolytic, 14% osteoblastic and 38% mixed) with the most common sites being dorsal spine (62%), lumbosacral spine (72%) and pelvis (79%). Twenty-nine percent of these fractures occurred in ribs and 9% for both vertebrae and in long bones (Scheid *et al.*, 1986).

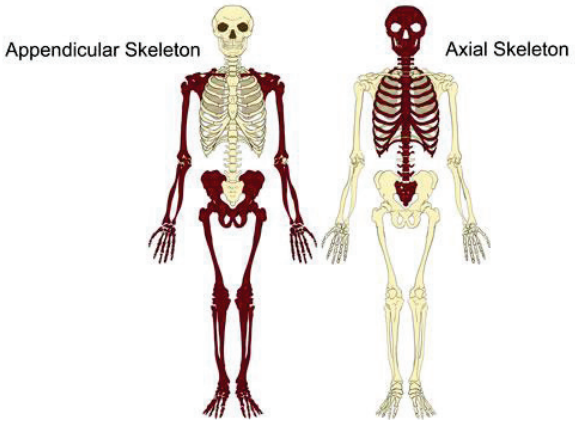

Figure 8: Definition of axial and appendicular skeleton (http://www.teachpe.com)

Finally, in a study gathering 142 patients (all patient diagnosed with metastatic bones between 1996 and 2003 at Karolinska university hospital, Sweden), 37 prostate cancer patients with blastic lesions,

all presented a pathological fracture (Wedin and Bauer, 2005). Authors report that a possible explanation could be that sclerotic bone became brittle and prone to fracture (Wedin and Bauer, 2005).
This highlights that every type of metastatic lesions is problematic and needs particular attention from clinicians.

b. Bone metastases treatment

It is considered that when metastases colonize bone, that cancer is incurable (Wong and Pavlakis, 2011). Thus, bone metastases treatment is not a recovery treatment, but aims to prevent any further skeletal events (fracture or other sites development) and to provide patients with a restoration of weight bearing and function that will outlast them (Wedin and Bauer, 2005).
As it was previously said, bone metastases activate both osteoclasts and osteoblasts, so the first clinical answer is to stop this anomaly. To do so, a bisphosphonate treatment can be used (Hoskin, 2003). It was reported to reduce the frequency of skeletal-related events and to reduce bone pain felt by patients (Hoskin, 2003).
Bisphosphonate inhibit bone degradation and reabsorption resulting in a decrease in bone turnover which is paralleled by a decrease in the number of osteoclasts and inhibition of activity of remaining osteoclasts(Hoskin, 2003). Still, as much as bisphosphonates reduce risk of fracture, it does not prevent new metastases development (Hoskin, 2003).
Another drawback of this kind of drugs is that as it stops bone development it produces an effect of “frozen bone” (Wong and Pavlakis, 2011), creating micro damage and decreasing bone toughness, as bone does not renew itself anymore.
Another aspect of bone metastases to stop is bone pain (Wong and Pavlakis, 2011). To do so radiotherapy is an established treatment (Wong and Pavlakis, 2011). Efficiency of radiotherapy on bone pain is partially understood, although it surely has effect via reducing metastases, it seems to have an effect through osteoclast inhibition too (Wong and Pavlakis, 2011). Bone pain is treated with anti-inflammatory and opioids alongside with radiotherapy (Wong and Pavlakis, 2011).
To prevent bone failure, different consolidative techniques exists. Their aim is to obtain the reinforcement of bone defect through percutaneous injection of polymethylmethacrylate cement (Cazzato et al., 2018). Many of these reinforcements can be achieved *via* interventional radiology.
In last resort when the lyses are too spread or interventional radiology is not suitable (as in long bones), surgery is led, giving way to specificities that are detailed bellow.

c. Surgical intervention on metastatic bone

Surgical indications

Indications for surgery vary among patients and surgeons (Attar *et al.*, 2012). Anyhow, most clinicians agree that the decision to make a patient undergo surgery depends on several aspects as location of tumor, expected morbidity, if the bone integrity is at risk, life expectancy and patient expectation and pain, among others (Attar *et al.*, 2012).

Surgical intervention goal is to decrease pain assuring bone stability and thus improving mobility, bone function and patient quality of life (Attar *et al.*, 2012). It implies the patient to be fit and recovery time should not exceed patient life expectancy while providing a solution that is beyond it. This notion is tricky as it is based on multiple factors as age, comorbidities and extent of visceral and skeletal disease (Katagiri *et al.*, 2005).

Nevertheless, even a patient with low life expectancy could benefit pain relief from the stabilization of a bone allowing less painful bed-to-chair transfers (Attar *et al.*, 2012).

Therefore surgery is indicated when painful lesion is housed in weight bearing bone that did not respond to radiation therapy or if the mechanical stability is judged too low (Attar *et al.*, 2012).

Mechanical stability evaluation

Metastatic bone stability is hard to quantify, even for experienced surgeon (Attar *et al.*, 2012). Several medical technics can provide insight on it, as plain radiographs, Magnetic Resonance Imaging (MRI) scans and Computed-Tomography (CT) - scans.
Plain radiographs provide information on bone structural integrity while CT scans define cortical architecture and MRI scans show intramedullary extent of tumor extension (Attar *et al.*, 2012). As most classic guidelines were developed on plain radiographs, surgeons place more trust in them while asserting mechanical stability (Attar *et al.*, 2012). Despite the absence of absolute guidelines, different studies provided criteria to help clinical judgment and radiographic interpretation.

In 1973 Fidler suggested that a long bone lesion with more than 50% cortical destruction should be stabilized (Fidler, 1973). In 1982, Harrington summarized the trend at the time specifying that a stabilization of metastases femora should be taken when the lesion either is larger than 2.5cm, has caused destruction of more than 50% of the cortical or is causing pain even after radiotherapy trial (Harrington, 1982).

Finally, in 1982, Mirels suggested a scoring system to predict failure risk in long bones (Mirels, 2003). It was developed based on a retrospective study on 78 metastatic long bone lesions. It lies on four criteria: lesion site, size, degree of sclerosis/lysis and pain (Mirels, 2003). Each criterion is rated between one and three giving a sore rated on twelve. If the resulting score is less than 7, the probability of fracture is supposed to be low. A score of 9 or more is associated with a high fracture risk. The score of 8 presents a dilemma as it is slightly suggestive of an impending fracture (Mirels, 2003).

Parameter	Score		
	1	2	3
Site	Upper limb	Lower limb	Peritrochanter
Pain	Mild	Moderate	Severe
Lesion	Blastic	Mixed	Lytic
Size	<1/3	1/3–2/3	>2/3

Figure 9: Table illustrating Mirels' score

Over time, Mirels' score became a widely used and studied tool (Van der Linden *et al.*, 2004). However, Mirels's study was based on bones that mostly had presented a fracture or had undergone prophylactic osteosynthesis (Van der Linden *et al.*, 2004). In order to test and improve Mirels' score if necessary, Van der Linden led a retrospective study including 102 patients with metastases femora of whom 14 suffered a fracture during follow-up. Using Mirels's score, Van der Linden rated all femora and compared the result to the fracture events during a follow-up.

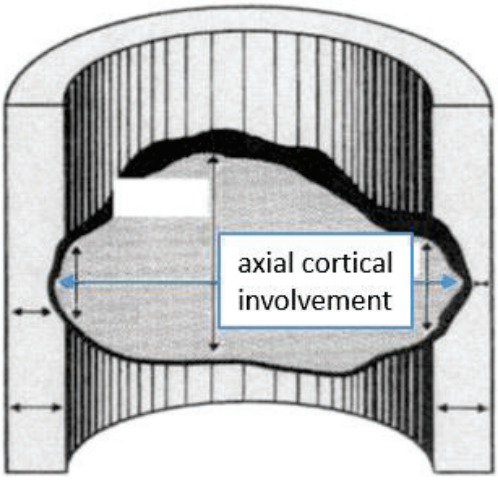

Figure 10: axial cortical involvement as defined by Van der Linden. Van der Linden et al 2004

Out of 102 patients, 84 (82%) would have been surgically over treated while 13% of the lesions without fracture were detected at low risk (Van der Linden *et al.*, 2004). Therefore, a size of 30mm (Figure 10) on axial cortical involvement was used, reducing supposed over-treatment to 42% (Van der Linden *et al.*, 2004).

Still, as surgical over treatment has a large impact on quality of life in patients who have a limited life expectancy (Van der Linden *et al.*, 2004), a more accurate failure risk predictor would be necessary. In order to provide such a tool, more advanced imaging technics are used. For example, a study quantified structural rigidity based on CT scans on children. This rigidity was quantified on both limbs of said children, one of which suffered benign bone tumor (Leong *et al.*, 2010).
Another study similarly applied these methods to quantitative CT, MRI and dual-energy x-ray in order to estimate the relative fracture risk of trabecular defects in vertebral bodies (Hong *et al.*, 2004).
Among other trail to improve failure risk assessment, one leads toward patient-specific finite element analysis (FEA) models, whose investigations have started in the nineties (Cheal *et al.*, 1993). This trail will be furtherly discussed in the next section.

5. *Biomechanics basics*

Biomechanics has its own terminology that is based on mechanical engineering. Before anything, this part aims to define parameters that will be used in the present study.

The concept of stress and strain are fundamental to bone biomechanics (Turner and Burr, 1993). Stress is defined as force per unit area and may be classified as compressive, tensile or shear, depending on how loads are applied (Figure 11). Strain is defined as percentage in length or relative deformation (Figure 11). The relationship between stress applied and corresponding strain is called stress-strain curve (Figure 11). It can be divided into two regions: the elastic strain region and the plastic strain region. Within the elastic region, bone reacts like a spring and the strain in the bone

increase linearly with the increasing stress (Turner and Burr, 1993). At this point, if stress is to be relived, bone would come back to its original form (Turner and Burr, 1993) without damage.

The slope linking stress to strain is called the Young's modulus; it is a measure of the intrinsic stiffness, expressed in Pa (Turner and Burr, 1993) that is bone geometry independent.

As soon as plastic region is reached, if the stress was to be relived, a permanent strain should appear, following the slope of the Young's modulus , thus implying a subsequent strain, even when load is totally released(Turner and Burr, 1993). The point linking elastic and plastic parts of the curves is called yield point.

The same curve can be traced between force and displacement. In this curve, the slope linearly linking force to displacement will be the structural stiffness, expressed in N/mm, which is a measure of the stiffness of the tested structure (Turner and Burr, 1993).

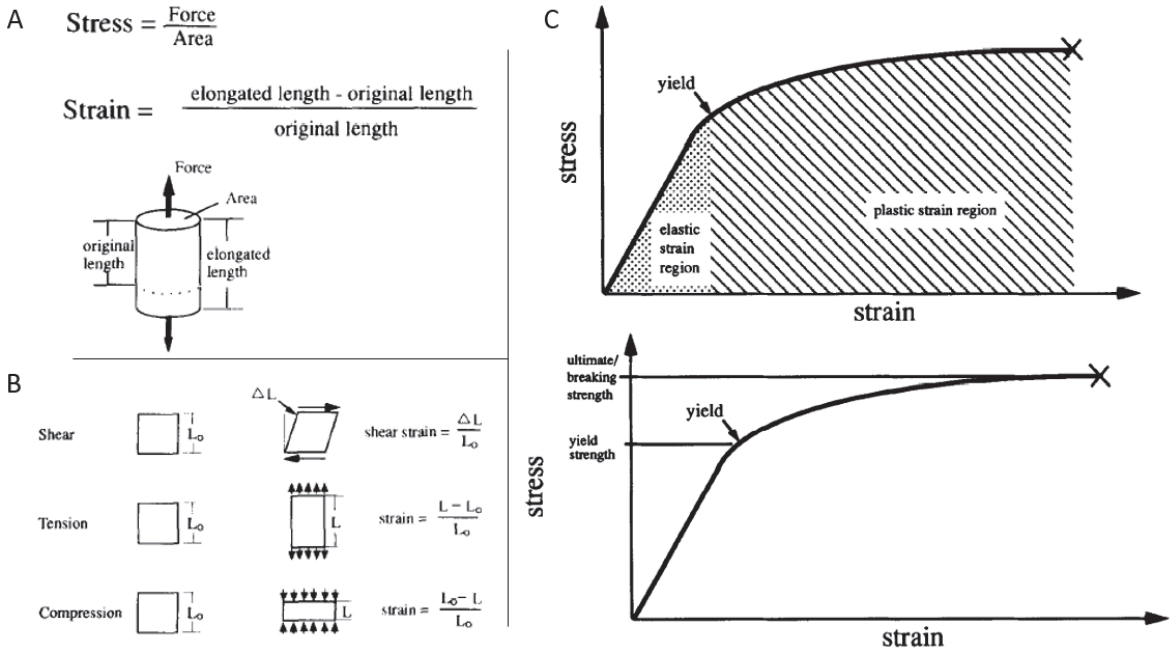

Figure 11: A Stress strain definition, B strain type definition, C Stress-strain curve, all three from Turner *et al.* 1993

6. *Finite Element Analysis in Biomechanics*

a. Finite Element Analysis: a quick introduction

Briefly, Finite Element Analysis (FEA) is a numerical method to solve engineering and mathematical physics problems (Logan, 2012). Typical problem areas of interest that are solvable using FEA include structural analysis, heat transfer, fluid flow, mass transport and electromagnetic potential (Logan, 2012).

For instance, finite element method is often used in mechanical engineering field to calculate stiffness, strength, or even internal strains and stresses of complicated structures subjected to external forces (Zysset et al., 2015)

FEA allows to solve problem without analytical solution for the whole body (Logan, 2012). Analytical solutions are those given by mathematical expression that yields the values of the desired unknown quantities at any location in the body (Logan, 2012). Therefore, these solutions are valid for an infinite number of locations in the body.

Analytical solutions generally require of ordinary or partial differential equations, which are not usually obtainable for complex geometries, loading, and material properties (Logan, 2012).

In order to overcome these difficulties, finite element formulation results in a system of simultaneous algebraic equations for solution, rather than requiring solution of differential equation (Logan, 2012). This allows to obtain approximate values of the unknown at discrete numbers of points in the continuum (Logan, 2012).

Thus, FEA is starting with a discretization step that consists in modelling a body by dividing it into an equivalent system of smaller and simpler bodies (giving the name: finite elements) interconnected at points common to two elements (nodes) and/or boundary lines or surface (Logan, 2012).
Then, instead of solving the problem for the entire body in one operation, equations for each element is formulated and then combine to obtain the solution of the whole body (Logan, 2012).
As bone-loading simulation could be considered as a structural loading, it uses the same springs. The solution of those problems typically refers to determining the displacements at each node and the stresses within each element constituting the structure that is subjected to applied loads (Logan, 2012).

b. Finite Element Analysis used on bone

Experimental testing on human participants and cadaveric specimens provides researchers in biomechanics and orthopedics with valuable insights on how human bones and body reacts to loading scenarios (Burkhart *et al.*, 2013). However, experimental testing on humans is not always feasible in order to ensure participants safety compelling to limit loads to sub maximal and non-invasive techniques. Testing on cadavers, while allowing more flexibility, can become costly and are inherently destructive (Rogge *et al.*, 2002).

In comparison, Finite Element (FE) models provide a feasible alternative for predicting bone response in a variety of loading conditions and have become a popular and powerful tool among biomechanics and orthopedics researchers (Chevalier *et al.*, 2007; Verhulp *et al.*, 2006; Viceconti *et al.*, 2008).

In the bone field, two modeling technics exists. µFE models and homogenized FE models, are each used on different types of images. In fact, µFE require high spatial resolution images so that the elements of the mesh contain bone material only (Figure 12, Zysset et al., 2015). Main drawback being that needed resolution for this particular model cannot be reach *in vivo* for spine and hip (Zysset et al., 2015). Currently, images at a resolution that is good enough to resolve the trabecular microstructure can only be obtained for peripheral skeleton (van Rietbergen and Ito, 2015).
On the other hand, Homogenized FE models Figure 12 are created based on images obtained on whole-body clinical CT scanners (Zysset *et al.*, 2015). Then, material properties of the bone/marrow mixtures are determined though a homogenized averaging process, giving the method its name.

It is generally agreed that an optimal mesh density exists, allowing to have the most accurate solution with the smallest possible amount of elements (Burkhart *et al.*, 2013). It is commonly determined through the use of a convergence study (Burkhart *et al.*, 2013).

It was reported that there has been a 6000% increase in the number of FE modeling papers published between 1980 and 2009 (Erdemir *et al.*, 2012), but attention to mesh quality and model validation was not adequately kept with general use of FEA approach (Lund *et al.*, 2012).

In order to improve the situation, Burkhart et al. edited guidelines from which several parts are of particular interest for the current study (Burkhart *et al.*, 2013).

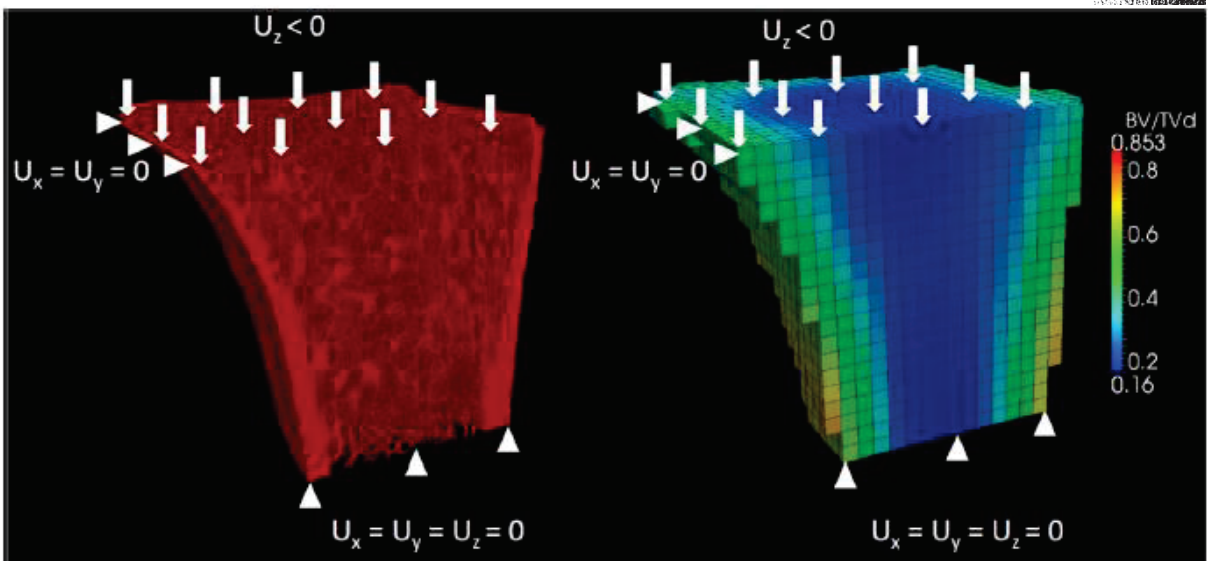

Figure 12: µFE and homogenized FE models illustration from Zysset et al. 2015

As accuracy and efficiency of FE simulation is highly predisposed to the quality of FE mesh, it should be an object of particular interest (Knupp, 2001). Given complex geometry associated with human bones, elements with large distortions can occur and are potential sources to low accuracy or solution instability (Burkhart *et al.*, 2013).
There are two elements shapes that are chosen to discretize the geometry of bone: tetrahedral and hexahedral (Burkhart *et al.*, 2013). In general, hexahedral elements are considered to be more accurate and efficient than tetrahedral elements, especially when performing dynamic simulation (Burkhart *et al.*, 2013) (such as a fall for example).

There are three metrics to optimize when coming to mesh shape. The first being aspect ratio (AR) (Burkhart *et al.*, 2013). AR is calculated by dividing the longest edge or diagonal of an element by the shortest in hexahedrons, and by dividing the longest edge length by minimum altitude of the smallest side (Burkhart *et al.*, 2013).

The most accurate solutions are achieved when ARs are close to one (Burkhart *et al.*, 2013). However, bones contain sections that tend to result in unavoidably thin elements (Fellipa, 2012). Thus, it has been suggested that ARs for hexahedral elements having AR within 1 and 3 are acceptable, within 3 and 10, are to be treated with caution and with alarm if superior to 10 (Fellipa, 2012). Less has been reported for tetrahedral elements, it has be found that AR between 1 and 4 produced smallest errors (Pistoia *et al.*, 2002). Burkhart *et al.* on their part recommend having the percentage of ARs greater than 3 below 5%.
The second metric is the angle idealization. Elements whose interior angles deviate too far from ideal angle (90° for hexahedrons and 60° for tetrahedrons) can produce unrealistic deformation responses (Burkhart *et al.*, 2013). Therefore, it is suggested that elements angle idealization may be considered satisfactory providing less than 5% of internal angle deviation exceeding 70° (El-Hamalawi, 2000; National Academies of Sciences, 2011; Quenneville and Dunning, 2011). Even if less documented,

tetrahedral elements appears to be acceptable if their internal angle is between 30° and 150° (Klingner and Shewchuk, 2008).

The third and last is the Jacobian ratio. It is defined as a measure of volume distortion from an ideally shaped element and represents the determinant of the Jacobian matrix. Literature suggests that assessment of hexa and tetrahedrons is the same and can be described by the following criteria:

- Be positive in value (Fellipa, 2012)
- Preferably greater than 0.2 in magnitude (Quenneville and Dunning, 2011)
- Less than 5% of all Jacobians should fall a magnitude below a magnitude of 0.7 (National Academies of Sciences, 2011)

As these metrics can influence the simulation results and results stability, it is to be thoughtfully investigated.

Despite its promising results, patient-specific FEA is not yet clinically used in routine, due to the fact that automatic model creation is hard to reach and clinical validation process is long.

Parameters used in presented studies are summarized in Table 1

7. *Patient-specific finite element analysis model in order to predict failure, in case of bone metastasis*

Patient-specific finite element analysis was widely studied in order to assess failure risk in osteoporosis, showing good results (among others: (Bessho *et al.*, 2009; Duchemin *et al.*, 2008; Keyak *et al.*, 2013; Kopperdahl *et al.*, 2014; Zysset *et al.*, 2013).

Because of the advantages of this method compared to other trails, it was more recently studied as a potential tool to improve failure prediction of metastastic bones (Derikx *et al.*, 2012; Eggermont *et al.*, 2018; Goodheart *et al.*, 2015; Keyak *et al.*, 2005; Tanck *et al.*, 2009). Indeed patient-specific FE models do not need a contralateral limb that did not developed lesion, which is imperative for CT-based rigidity method previously cited. Moreover, it allows different load types and therefore could be more suited to clinical practice where clinicians would like to advise the patient which activity is safe and which is at risk regarding their lesions (Derikx *et al.*, 2015).

Cheal *et al.* (Cheal *et al.*, 1993) were among the first to try FEA for this purpose. Anyhow, due to technical limitation at that time, their FE model was based on average anatomy and material behavior data (Cheal *et al.*, 1993), preventing them to capture biomechanical contrast. This led to a large difference between simulated failure load and experimental failure load.

Later, another group has assessed FEA to predict fracture risk in bone cancer (Keyak et al., 2001). Through a large study,(Keyak et al., 2007, 2005, 2001) Keyak *et al.* developed a full workflow for patient-specific FE modeling based on CT scans. A relationship between CT values (attenuation) and bone mechanical properties (Young's modulus) was empirically developed (Keyak *et al.*, 1996). Then *ex-vivo* mechanical failure tests were proceed and found good agreement with FEA results (r=0.97) (Keyak *et al.*, 2005). Furthermore this workflow was used on femurs with reproduced and real

metastatic lesions and, once again, showed good agreement (r=0.98 with induced defect and r=0.94 for real metastatic defect) (Keyak *et al.*, 2007).

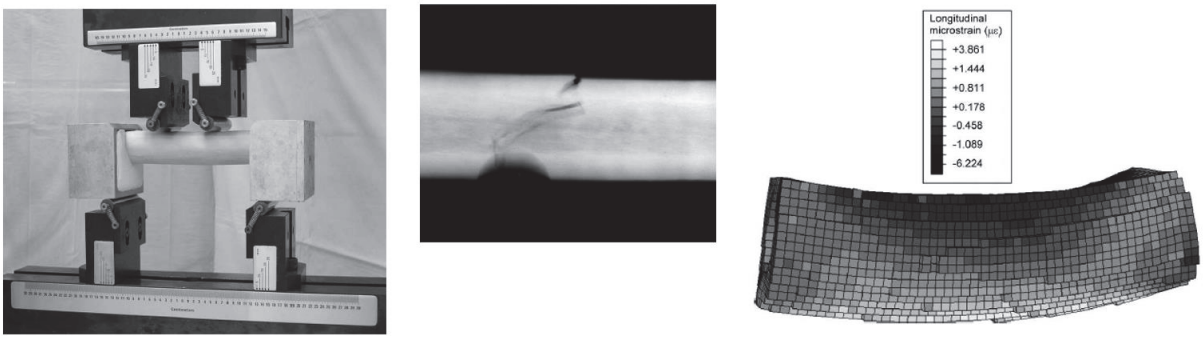

Figure 13: Four-point bending mechanical test, CT image of fractured tested bone and FE simulation from Keyak et al 2005

Building on this work (Keyak *et al.*, 2005), Derikx *et al.* developed and validated a workflow for generating subject-specific FE models (Derikx *et al.*, 2012; Eggermont *et al.*, 2018; Tanck *et al.*, 2009).

The two first studies (Derikx *et al.*, 2012; Tanck *et al.*, 2009) aimed to develop, validate and compare the results given by FE patient-specific models to clinician expertise. Briefly, defects were mechanically induced on cadaveric femurs. They were CT-scanned and clinical like plain radiographs were created and given to clinicians (3 orthopaedic surgeons,2 oncologists and 1 radiologist) for evaluation. This evaluation was based on a combination of techniques, depending on professional background of each clinician. In the same time, the bones were mechanically tested in a configuration mimicking single leg stance. Finally, FEA was proceeded in order to evaluate agreement of failure load with experimental tests.

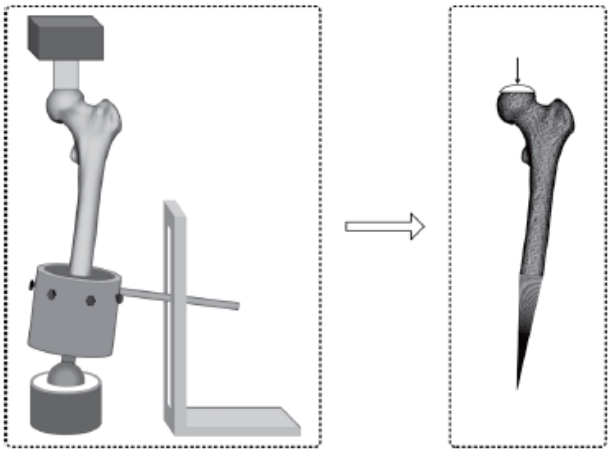

Figure 14: Diagrams showing the experimental set-up (left) and the same conditions mimicked in the finite element model (right) in both studies (Tank *et al.* 2009 and Derikx *et al*. 2012).

To assess this load, elastoplastic behavior was implemented to FE models, and a controlled displacement was applied though a cup to the femoral head, thus mimicking perfectly experimental test (Figure 14). Failure load was assumed to be the highest reaction force. Both studies showed that, under those simple loading condition, FEA models can outweigh the performance of clinical experts (Figure 15).

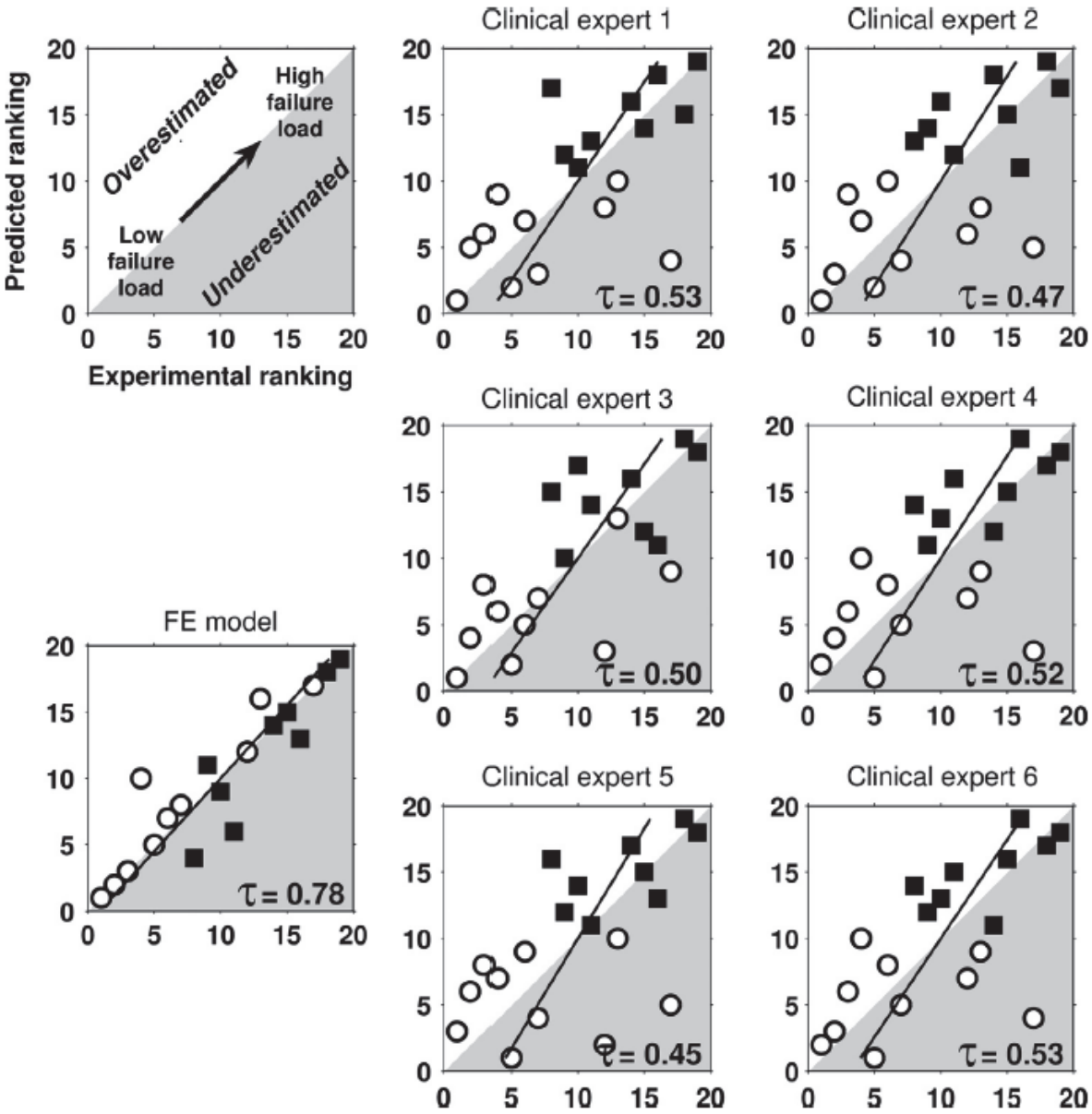

Figure 15: Results from Derikx *et al.* 2015 comparing fracture prediction for six clinical experts and FE model Intact femurs (squares) and femurs with artificial lyticlesions (circles).

However, these studies suffered a great limitation: comparison was based on an *ex-vivo* study with mechanically induced defect, and there was no way to tell if the same results would be found on real patients.

That limitation was recently overcome, when a clinical retrospective study was led by the same team (Eggermont *et al.*, 2018).

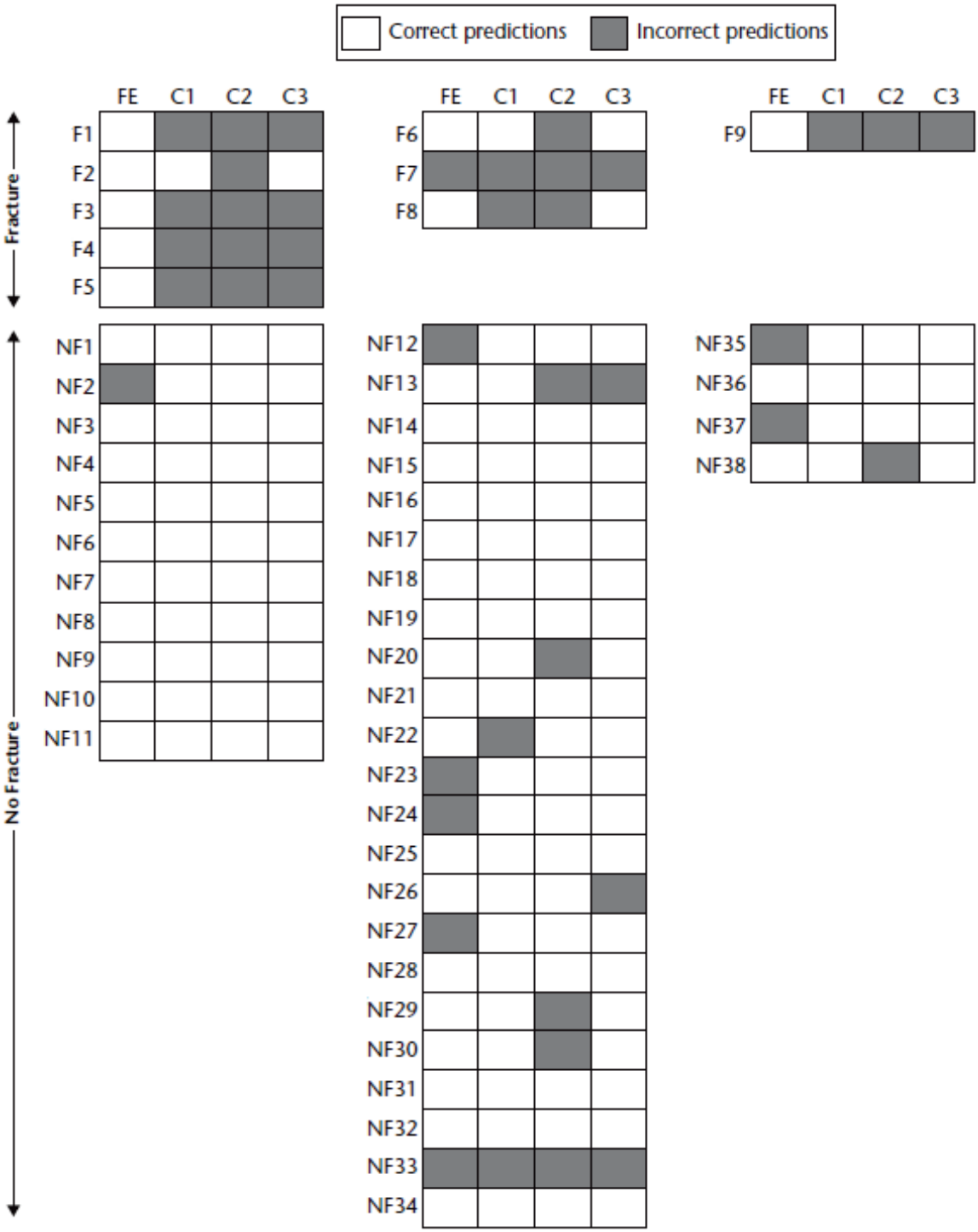

Figure 16: Results from Eggermont *et al.* 2018, showing prediction and its relevance with event that actually happened

In this study, 39 patients with non-fractured femoral metastatic, either lytic or mixed lesion were included based on the criteria presented in Figure 17. Each patient was followed for six month, until femur failure or death (which ever occurred first) (Eggermont *et al.*, 2018).

Inclusion criteria
Proven malignancy
Karnofsky[16] performance status ⩾60
No clinical or radiological evidence of pathological fracturing of the femur
No prior palliative surgery for the current treatment site of the femur
No planned surgical intervention of the femoral bone
No systemic radiotherapy 30 days prior to entry into the study
No previous radiotherapy to the current treatment site of the femur
Patient is able and willing to fill out baseline and follow-up forms on pain and quality of life
Patient is willing to undergo additional CT scans for the femoral region

Figure 17: Inclusion criteria from Eggermont *et al.* 2018

Same workflow was applied in order to obtain patient-specific FEA models. Using the same approach, femurs were stated at risk or not. After 6 months, it was compared to what actually happened and to clinician's expertise. Results agreed with previous studies, showing a better prediction with FE models (Figure 16, sensitivity (correctly identifying clinical fractures) of 89% versus 0% to 33% for clinical assessments).

Even though the difference is incommensurate with previous cited result, it is to be noted that clinician scored a higher specificity than FE models (specificity (correctly identify cases that do not fracture) was 79% for the FE models versus 84% to 95% for clinical assessments), leaving room for improvement.

Another team has worked on the possibility to clinically predict fracture (Goodheart *et al.*, 2015). In the first steps, their work was applied on animal model (those will be discussed in a following section). Briefly, a series of patients with metastatic femoral lesions had CT scans, were followed prospectively for four months. They were categorized in 3 groups: fractured (n=5), non-fractured (n=28) and stabilized (n=11).
From the CT scans, voxel-based FE models were created.
Different Young's moduli were implemented using two density-modulus power laws. Three different load cases were applied accordingly to Figure 18. A Hoffman's failure model was used with differential compressive (0.667%) and tensile (0.4%) yield strains (Niebur *et al.*, 2000).

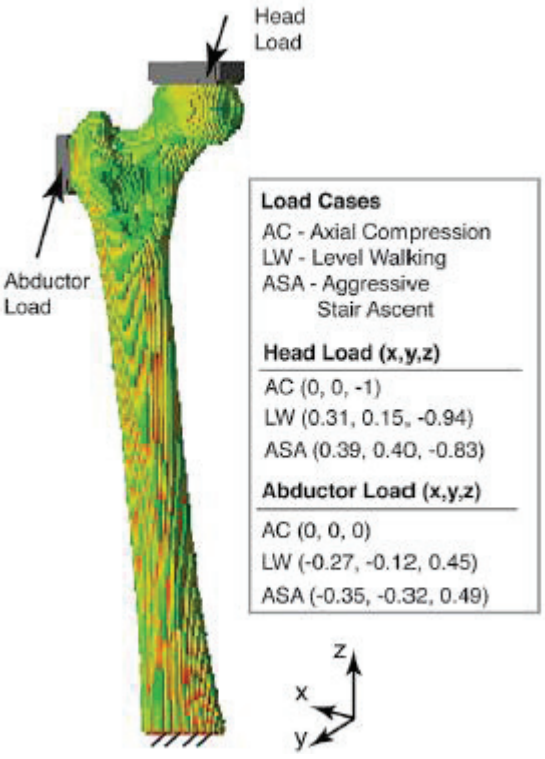

Figure 18: load case defined by Goodheart *et al.* 2015

Results were of the same order as the FE-LW model (see Figure 18 for denominations) had a specificity of 86% (over 43% for Mirels's score for same bones). Sensitivity was lower than in the previous study (50%) but only relying on five cases.
Nonetheless, patient-based studies have inherent limits. Indeed, the patients' recruitment for retrospective study is a difficulty, in addition to the time needed to perform it. Limitation are the same for *ex-vivo* study, as samples, even without real metastatic defect, are hard to find, making studies rely on few samples (20 femora for Derikx *et al.* 2012 (Derikx *et al.*, 2012), 10 for Tanck *et al.* 2009 (Tanck et al., 2009), 12 for Keyak *et al.* 2005 (Keyak *et al.*, 2005)).

These limitations could be overcome using an animal model in order to create as much metastatic bones as necessary, plus creating tumor tissue in order to test it and implement it in the simulation, which is a limitation to previously quoted studies.

All parameters used in the studies presented in the current section are presented in Table 1

Table 1: recapitulative table of parameters used in FEA on human bone in studies presented in the current section and 6.b. section)

Studies	Clinical or *Ex-vivo* study	Bone Considered	Sample/patient number	Cancer Study (Yes/No) (Real/Drilled lesion)	Mesh element type	Model type (elastic/elasto-platic…)	Validation on experimental tests (Yes/No)	Type of failure Criterion used	Apprent density/ young's modulus correlation law type
Cheal et al. 1993	*Ex-vivo*	Fermora	17 pairs	Yes (Drilled)	Hexahedrons	Elastic orthotropic (cortical bone) and elastic isotropic (trabecular bone)	Yes	Based on strain	Empirical values
Rogge et al. 2002	*Ex-vivo*	Radius	5	No	Hexahedrons	Isotropic Linear elastic	Yes	Based on strain	Power law
Pistoia et al. 2002	*Ex-vivo*	Radius	70	No	Hexahedrons	Isotropic Linear elastic	Yes	Based on strain	Constant
Keyak et al. 2005	*Ex-vivo*	Fermora	12 +6	Yes (12) and No (6) (Drilled)	Hexahedrons	Isotropic Linear elastic	Yes	Based on stress	Linear law
Verhulp et al. 2006	*Ex-vivo*	Fermora	2	No	Hexahedrons	Isotropic Linear elastic	No	N/A	Constant and power law
Chevalier et al. 2007	*Ex-vivo*	Femora	6 trabecular sample comming from 3 femora	No	Hexahedrons	Isotropic Linear elastic	Yes	Von Mises stress	N/A
Duchemin et al. 2008	*Ex-vivo*	Femora	40	No	Hexahedrons	Isotropic Linear elastic	Yes	Based on stress and continuity	Linear law
Tanck et al. 2008	*Ex-vivo*	Femora	5 pairs	Yes (Drilled)	Hexahedrons	Isotropic elastoplastic	Yes	Max strength	Linear law
Besho et al. 2009	Clinical	Femora	42	No	Tetrahedrons	bi-linear elastoplastic	No	Based on strain	Linear law
Quenneville et al. 2011	*Ex-vivo*	Tibia	7 pairs	No	Hexahedrons	Isotropic Linear elastic	Yes	Empirical limit values in stress	Constant
Derikx et al. 2012	*Ex-vivo*	Femora	10 pairs	Yes (Drilled)	Tetrahedrons	Isotropic elastoplastic	Yes	Max strength	Linear law
Keykak et al. 2013	Clinical	Fermora	377	No	Hexahedrons	Isotropic elastoplastic	No (retrospective study)	von Mises stress failure criterion	Power law
Kopperdahl et al. 2014	Clinical	Femora and Vertebrae	167(Vertebrae) + 171 (Fermora)	No	Hexahedrons	Isotropic elastoplastic	No (retrospective study)	Based on bone mineral density	Linear law
Goodheart et al. 2015	Clinical	Femora	44	Yes (Real)	Hexahedrons	Isotropic Linear elastic	No (retrospective study)	Based on strain	Power law
Eggermont et al. 2018	Clinical	Femora	39	Yes (Real)	Tetrahedrons	Isotropic elastoplastic	No (retrospective study)	Max strength	Linear law
Benca et al. 2019	*Ex-vivo*	Femora	16 pairs	Yes (Drilled)	Hexahedrons	Isotropic elastic-damage	Yes	Max strength	Linear law

8. Mice, a skeletal animal model

Mice has been widely used as a skeletal model (among others : (De Souza et al., 2005; Fritton et al., 2005a; Gardner et al., 2006; Holguin et al., 2013; Lynch et al., 2010; Patel et al., 2014; Pereira et al., 2015; Prasad et al., 2010; Yang et al., 2014)). Most of this research aims to study bone remodeling under mechanical stimulation.

To do so, researchers used a conservative cycling loading protocol that was previously developed on rat ulna (Robling *et al.*, 2001). As much as the loading protocol is the same (Figure 19) for the study evaluating bone remodeling ((De Souza et al., 2005; Fritton et al., 2005a; Gardner et al., 2006; Holguin et al., 2013; Lynch et al., 2010; Patel et al., 2014; Pereira et al., 2015; Prasad et al., 2010; Yang et al., 2014)), the way its effect on bone is evaluated vary a lot among them.

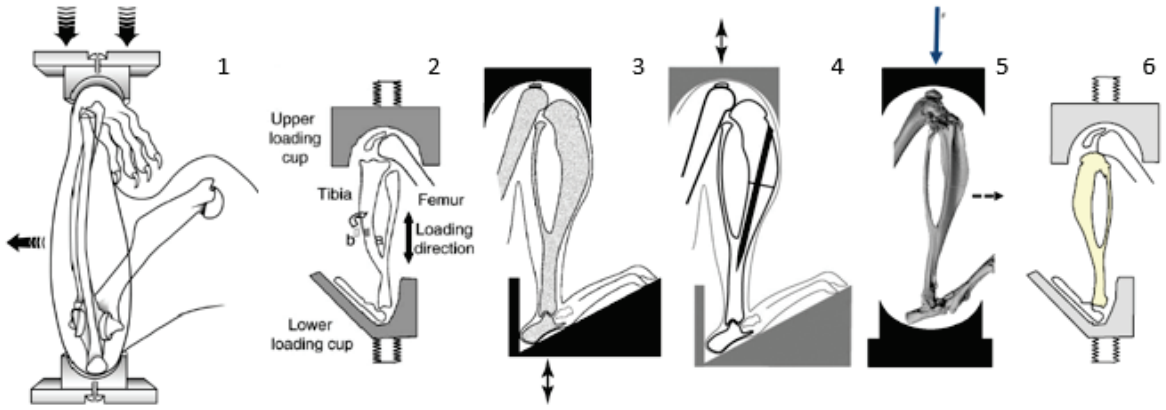

Figure 19: Loading fixtures descripted by Robling *et al.* 2001 (1), re-adapted and reused on mice tibia by De Souza *et al.* 2005 (2), Fritton *et al.* 2005 (3), Gardner *et al.* 2006 (4), Patel *et al.* 2014 (5), Pereira *et al.* 2015 (6).

For instance, one of the sub-cited study used histology as a comparative technic (De Souza *et al.*, 2005).While two quantified bone architecture transformation though QCT acquisition (Fritton et al., 2005a; Gardner et al., 2006) and another histomorphometry (Lynch *et al.*, 2010). Two other built FEA models using CT scans (Patel *et al.*, 2014; Pereira *et al.*, 2015). The last one both used whole bone compressive until failure test and bone architecture assessed though CT scan (Holguin *et al.*, 2013).

This underlines that even if mice have imposed itself as a bone animal model, and even if the way to stimulate bone remodeling in mice model has made a large consensus, the way to quantify the provoked change did not.

9. Mice model in cancer study

Rodent models predominate preclinical studies (Slosky et al., 2015a). The use of mice or rats is mostly decided though three factors: ease of use, recapitulation of human pathology and technologies available (Iannaccone and Jacob, 2009).

Rats have larger bones than mice, that facilitates intramedullary implantation of tumor cells (Slosky et al., 2015a). Moreover, rats presents similarities with human on hormone responsiveness and premalignant stages, which makes it an excellent animal model to study breast cancer (Iannaccone and Jacob, 2009).

Nonetheless, mouse model is more amenable to genetic manipulation. Transgenic animal that over or under express a protein of interest are particularly useful to investigate cells mechanism-based research question (Geis *et al.*, 2010).

In fact, there is a lot of murine models of cancer metastasis to bone, each with its individual limitations and benefits (Wright *et al.*, 2016). Because spontaneous metastases to skeleton from primary tumor in animals is rare (Mundy, 2002), and no model reproduces all cancer mechanisms observed in human, researchers must select a model (or a combination of models) best suiting the aspect of metastatic disease that is to be investigated (Wright *et al.*, 2016). However, the non-spontaneity to develop metastases underlines the need to inject tumor cells to animal to develop tumors.

Prior to 1999, there existed only two strategies for generating *in vivo* models of solid tumor-induced bone destruction (Mantyh, 2013).

The first strategy involves injecting tumor cells into the left ventricle of the heart in rodent (Slosky et al., 2015a) (Figure 20). Inoculation directly in the blood stream provides a good tool to investigate processes associated with cancer cell homing, colonization, subsequent metastatic tumor growth and lesion formation in bone (Wright *et al.*, 2016). Once injected, these cells spread to multiple sites around the body, including bone marrow. Then tumor cells locally proliferate, resulting in the formation of a solid tumor within the intramedullary space and destruction of surrounding bone (Arguello *et al.*, 1988; Yoneda *et al.*, 1994). To summarize, this technic results in tumor cell dissemination in the arterial vascular system and homing primarily to long bones, spine, jaw and lungs (Ottewell *et al.*, 2015, 2014).

But intra-cardiac inoculation has its drawbacks too, as it creates a large inter-animal variability in site and size of metastases (Mantyh, 2013), making development site uncontrolled. Furthermore, unwanted and uncontrolled visceral metastases, particularly to the lung, can significantly decrease mouse survival span, limiting the time frame of skeletal metastases *in vivo* study (Wright *et al.*, 2016)

The second way consists in direct intra-tibial injection (Figure 20) of cancer cells, resulting in the development of lesions in the injected bone with minimal impact to bone marrow, engraftment (Fathers *et al.*, 2012; Ottewell *et al.*, 2009; Werbeck *et al.*, 2014).

This model bypasses early stages of metastasis including homing in the bone micro-environment (Wright *et al.*, 2016). Therefore, it is useful for a more direct tumor-bone interaction assessment (Wright *et al.*, 2016).

It has to be noted that, in the case of a comparative study using the contralateral limb as a control, the second limb is to be injected using phosphate buffered solution (PBS) in order to create a sham

limb (Wright *et al.*, 2016). As it will be discussed further, the current work allowed to confirm this necessity (Delpuech *et al.*, 2017).

Since 1999, other technics has been developed such as intra-arterial injection (Wright *et al.*, 2016) or intramammary pad injection (Slosky et al., 2015a), responding to different specificity and interests.

As it was previously said, tumor cells has to be injected to develop cancer in murine due to non-spontaneity of these animals to develop metastasis from primary tumor (Mundy, 2002).

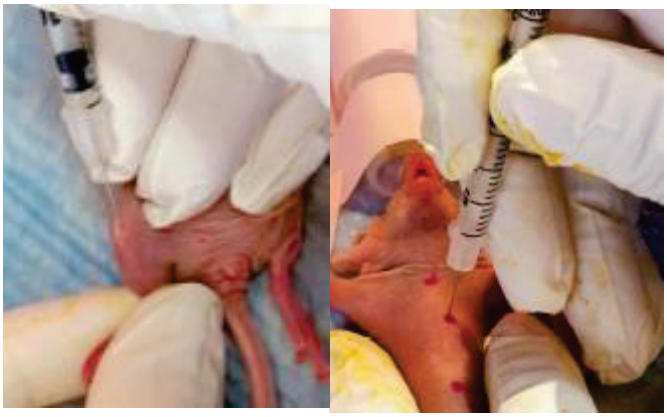

Figure 20: intra-tibial and intra-cardiac injection Wright *et al.* 2016

Here there are two choices: either injects human tumor cells into immune compromised mice (as BALB/c nude or MF1 nude), either injects immune competent mice with murine-derived cell lines 4T1 (Wright *et al.*, 2016).
Once again, this choice comes with advantages and drawbacks. Injecting immune compromised mice assures more chance of a successful metastases development, but there is no reaction of these animals immune system, as it is in patients (Wright *et al.*, 2016). Thus, injecting rodent with murine derived cell allow to have a more realistic model, injecting immune-compromised rodent with human cell allow to study said cells in a very permissive host environment, but maybe too permissive (Wright *et al.*, 2016).

At last one study is of particular interest to put back mice model utility in its context. As it was investigating mechanical stimulation on bone in the case of metastases development, it is using the knowledge that were discussed in both the current and previous sections (Lynch *et al.*, 2013). To do so, 46 immune-deficient mice (SCID) were randomized into tumor (n=24) and control (n=22) groups. Tumor group was intratibially injected with human cancer cells. PBS alone was injected to control group. The day after injection, both groups were divided in two, tumor group 1 (n=12) was subjected to mechanical loading in there right limb 5 times a week for 2 weeks (n=6) and 6 weeks (n=6) along with control group 1 (n=5+5). In the meantime, non-loaded mice (tumor group 2, (n=12) and control group 2 (n=12)) only underwent anesthesia for the time other animals were anesthetized to allow tibia loading.
It is to be noted that in the previously cited study (Fritton et al., 2005a) the non-loading effect was quantified using animals contralateral limb, but it was decided here to use other animal's to prevent any tumor migration (Lynch *et al.*, 2013).

After 2 weeks both groups 1 were sacrificed while both groups 2 were kept in the same routine for four more weeks (6 weeks in total). After sacrifice, µCT imaging and histology were performed on all loaded tibia. As it can be seen on Figure 21, results were drastic as both µCT and histology revealed that all non-loaded tibia contained histologically detectable tumors and nearly all were completely

degraded (71% of the animals) (Lynch *et al.*, 2013). In comparison, tumor tibia that underwent compression had tibia features similar to sham injected animals (Lynch *et al.*, 2013).

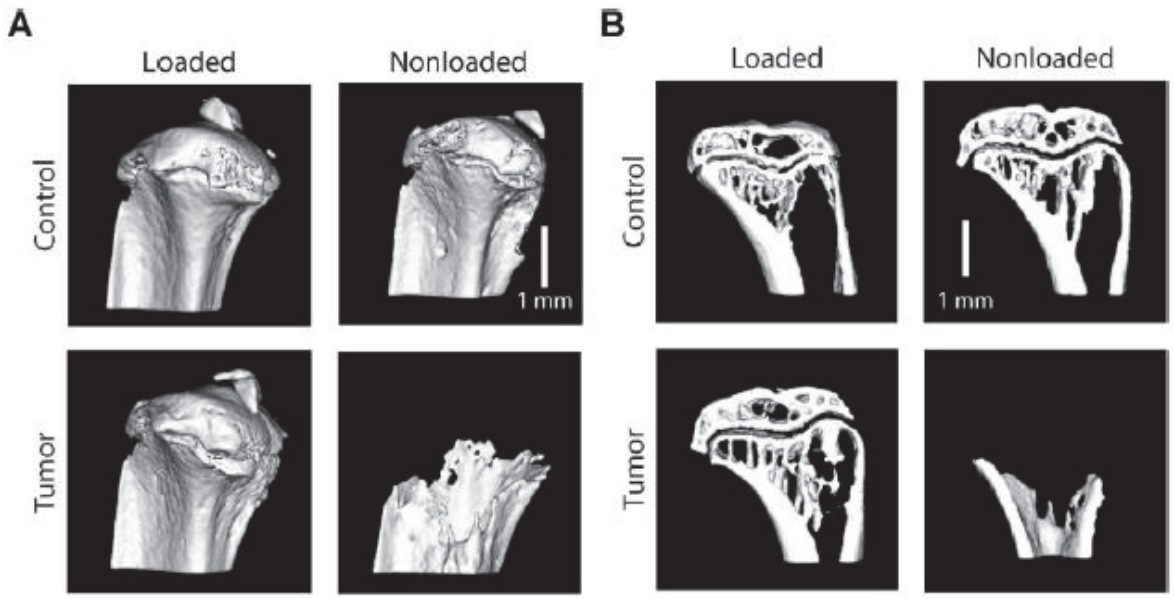

Figure 21: (A) 3D µCT reconstruction and (B) sagittal µCT sections of sham control and tumor tibia after 6 weeks from Lynch *et al.* 2013

This result emphasizes the use of animal model study. In fact, such a study would have thankfully been unconceivable on human. But mostly, it underlines the use of a better diagnostic on bone stability in bone cancer, as mechanical stimulation (thus physical activity) seems to inhibit metastases development.

a. FEA simulation on mice

As mice became a model for skeletal application and FEA became increasingly performed, it was logical that FEA would be used on mice.

As things mostly are at their beginnings, it started off confusedly.
In fact, FEA was used for a lot of different purposes. As an example, in previously cited study that investigated bone remodeling mechanism, it has been used to assess strain environment of cancellous and cortical bone for *in vivo* mouse loading (Lynch *et al.*, 2010; Pereira *et al.*, 2015; Prasad *et al.*, 2010; Yang *et al.*, 2014). But it was used too to understand mechanical cues that is driving bone adaptation to mechanical stimulation (Pereira *et al.*, 2015).
Other studies used it to examine effect of collagen orientation in hyperlipidemia mice model (Ascenzi *et al.*, 2014), to characterize changing in strain with age while loading (Razi *et al.*, 2015) and even the possibility to predict fracture in tumor bone (Mann *et al.*, 2008), as well as the implication of radiotherapy on bone brittleness too (Wernle *et al.*, 2010).
This variation in purpose induced different FEA model types.

One thing seemed to make consensus, all studies use linear elastic models (Lynch *et al.*, 2010; Patel *et al.*, 2014; Pereira *et al.*, 2015; Prasad *et al.*, 2010; Razi *et al.*, 2015; Wernle *et al.*, 2010; Yang *et al.*, 2014, 2014), even though one uses poro-elastic model on epiphysis due to their investigation specificity's (Pereira *et al.*, 2015). Half of these studies used hexahedrons elements (Lynch *et al.*, 2010; Mann *et al.*, 2008; Patel *et al.*, 2014; Prasad *et al.*, 2010; Wernle *et al.*, 2010) while the other half used tetrahedrons (Ascenzi *et al.*, 2014; Mann *et al.*, 2008; Razi *et al.*, 2015; Yang *et al.*, 2014). Most of them used a voxel to element conversion (Lynch *et al.*, 2010; Mann *et al.*, 2008; Patel *et al.*, 2014; Prasad *et al.*, 2010; Razi *et al.*, 2015; Wernle *et al.*, 2010), others meshed bone volume with non-constant elements (Ascenzi *et al.*, 2014; Pereira *et al.*, 2015; Yang *et al.*, 2014). For mechanical properties determination, a third of the studies used a constant modulus for all the elements (Young's modulus = 20GPa). Another third used a linear law linking hydroxyapatite degree with Young's modulus (Geis *et al.*, 2010; Mann *et al.*, 2008; Wernle *et al.*, 2010), and the last third linked it with either a power law or several linear laws (Pereira *et al.*, 2015; Razi *et al.*, 2015; Yang *et al.*, 2014).

All these studies worked on long bone, 6 on tibia (Lynch *et al.*, 2010; Patel *et al.*, 2014; Pereira *et al.*, 2015; Prasad *et al.*, 2010; Razi *et al.*, 2015; Yang *et al.*, 2014), 3 on femur (Ascenzi *et al.*, 2014; Mann *et al.*, 2008; Wernle *et al.*, 2010).

Facing this heterogeneity in FEA mice specific models without consensus, Nyman *et al.* decided to lead a comparative study in order to be able to choose models specificity to answer to their problematic and more precisely, while predicting bone failure (Nyman *et al.*, 2015).

To do so, 35 L6 vertebral bodies from 13 (n=15) and 17 (n=20) weeks of age coming from mice used for other studies were used (Edwards *et al.*, 2010; Yang *et al.*, 2004). Models were created from voxel to FEA elements conversion, creating 12µm elements (Nyman *et al.*, 2015).
Two different methods were used to apply mechanical values to elements.
Firstly, two models of each bone were created with constant Young's modulus (respectively 10 GPa and 18 GPa).
Secondly three others were created using three different laws linking hydroxyapatite to Young's modulus, two power laws (Easley *et al.*, 2010; Renders *et al.*, 2008) and a linear one (Wagner *et al.*, 2011).
Finally, Pistoia's criterion, that was found to strongly correlate with experimental failure force on human cadaveric radii was used as a failure criterion (Pistoia *et al.*, 2002). It states that failure should occur when 2% of the model volume exceed 0.007 in strain (Pistoia *et al.*, 2002). This criterion is commonly used in µFEA on mouse bone (Boyd *et al.*, 2011; Spatz *et al.*, 2013). To adapt the criterion both to short bone and mice, different failure volumes were tested for the model with a constant Young's modulus (failure volume varying from 0.1% failure volume to 10%) and for Wagner's *et al.* power law (Wagner *et al.*, 2011) (failure volume from 0.1 to 20%).
To assess different models' accuracy, root mean square error (RMSE) between experimentally measured peak force versus the predicted failure force of each and R^2 of each model were compared.
In a second time, failure strain was changed to optimized RMSE and R^2 for each conversion law.

Best results were obtained for a constant modulus of 18 GPa and Wagner *et al.* linear law (Wagner *et al.*, 2011), even though the results of the last were really close to Easley's *et al.* (Easley *et al.*, 2010) (Figure 22).

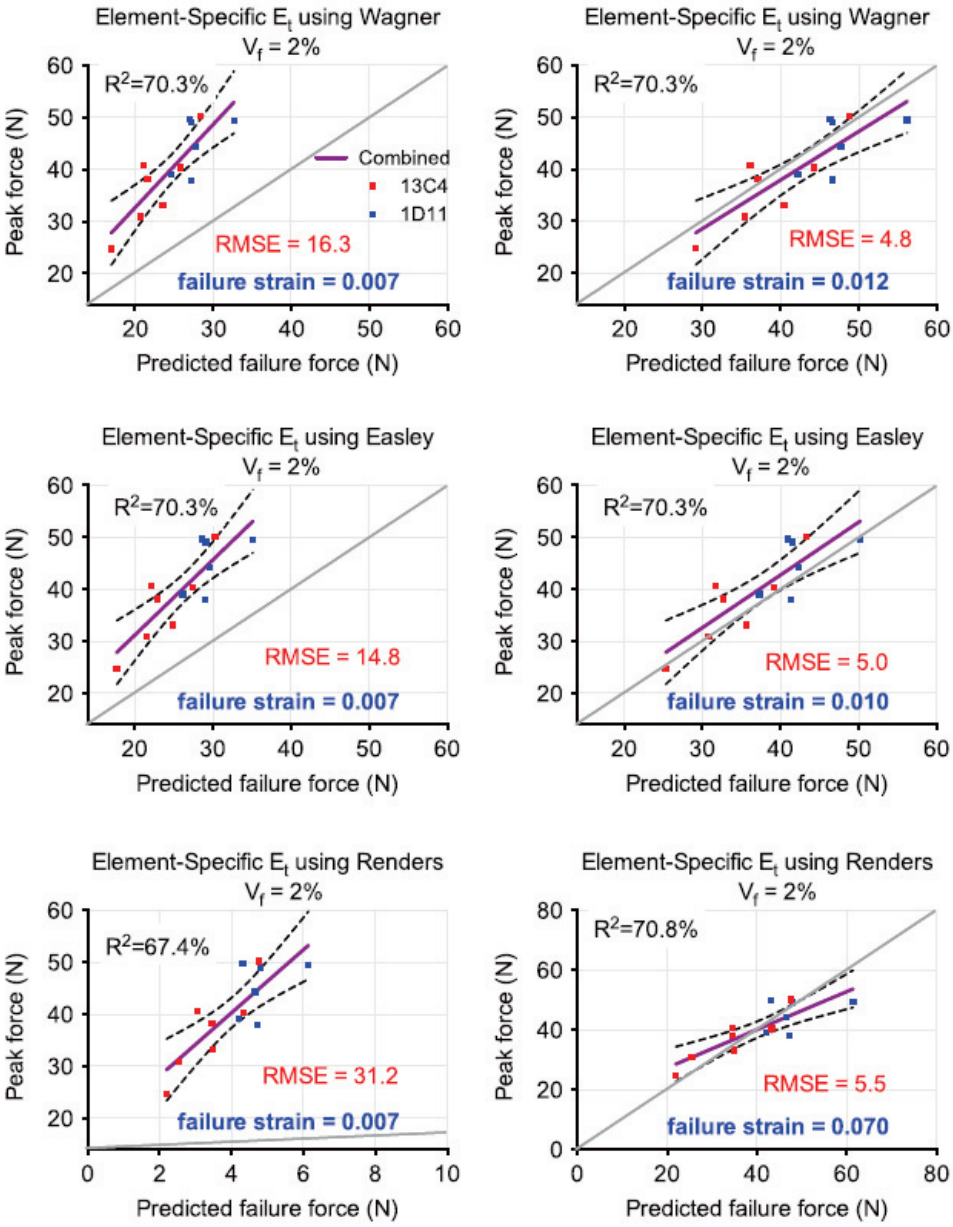

Figure 22: Results from Nyman *et al.* 2013, obtained for each material law on failure force using Pistoia's criterion native values (left) and a custom strain to optimize RMSE

It has to be noted that Easley's power law was used by Yang *et al.* on mice tibia and showed good local strain prediction (slop near 1 and R^2=0.6) (Yang *et al.*, 2014).

Finally, a study that was cited in this part is of particular interest for the current one. Indeed, Mann *et al.* used a mice model to see if fracture prediction could be improved using FEA way ahead of other teams, as the paper was published in 2008 (Mann *et al.*, 2008).

For this, 20 immuno-compromised 8-weeks old mice were injected in the femur with human breast cancer cells in their right limb, their left limb being untouched.
A custom conversion linear law between HA and Young's modulus was developed lying on a non-destructive 3- point bending test.
Femur were scan at 12µm resolution, voxels converted to FEA hexahedrons elements, the model being linear elastic.
To assess fracture with this model, the authors looked at the volume fraction of each FE models that had a strain over 1% (based on another study (Niebur *et al.*, 2000)) when the experimental ultimate load was apply for all control limbs. The average volume fraction was used as a failure volume in the fashion of Pistoia's criterion to all tumoral limbs.

The FEA results showed good agreement with experimental tests, with a R^2=0.91 and a slope of 1.02 (figure 20).

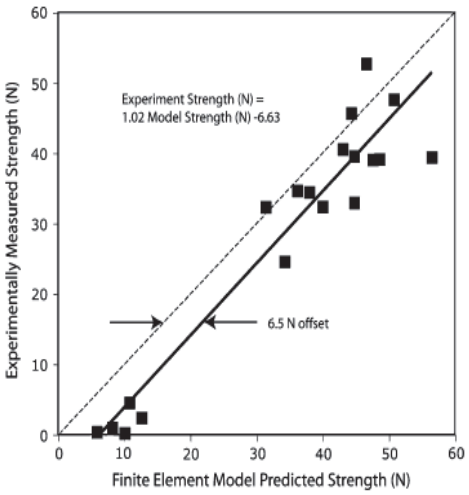

Figure 23: Finite element model predicted strength against experiment from Mann *et al.* 2008

Two years later, the same team published another paper investigating if FEA mice-specific models could as efficiently predict bone failure if mice were subjected to radiotherapy (Wernle *et al.*, 2010).

The exact same methods were used, the only difference being that two FEA models were created. The first using same power law as previous study, the second a non-linear HA density strength relationship (embrittled model).

Results were not as good as the one obtained in the previous study.

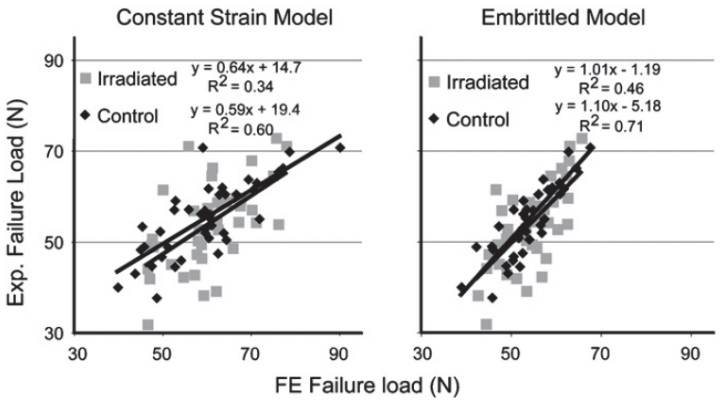

Figure 24: Finite element model predicted strength against experimental one for both constitutive laws from Wernle *et al.* 2010

In fact, control limbs showed a weaker correlation between FE and experimental failure load (R^2=0.6 for the previous FE model, 0.71 for embrittled model, Figure 24).

Correlation between irradiated bone failure loads was even lower (R^2=0.34 for the previous FE model, 0.46 for embrittled model, Figure 24).

10. Conclusion and PHD specific aim

To conclude, models that accurately predicted bone failure in patient that developed metastases in bone were either voxel based (composed of a lot of elements, (Goodheart *et al.*, 2015) or elasto-plastic models (Eggermont *et al.*, 2018). Moreover, metastases tissues were not taken into account in these models.

Furthermore, mice tibia was mostly used as a model for bone remodeling, inducing FEA models aiming to accurately predict strain, and not bone failure. However, Nyman *et al* 2015 predicting mice vertebral body failure and Wernele *et al. 2008* predicting mice femur failure in the case of metastasis both used a failure criterion in strain. For instance, Nyman *et al.* used a modified Pistoia's criterion and Wernele *et al* used a custom criterion in strain. This plus the fact that strain was locally validated in mice tibia (Yang et al., 2014) should make Pistoia's criterion available to detect mice tibia failure in our case.

Based on these facts and on the state of the art, our aim was twofold. First, we wanted to know if a FE model that would take into account specific tumor properties would help to better predict failure of tumoral bone. Second, we aimed to test whether a simpler model (linear elastic) could help on the mechanical stability evaluation as it would be quicker to solve, which could be important in clinical practice.

In order to test those hypotheses, the workflow presented in Figure 25 was implemented.

IV. Methods development

1. *Introduction*

This part presents all the development of the methods that were developed and used to achieve the goals of the current project.

First, mice were injected subcutaneously with tumor cell. Resulting tumors were resected and subjected to a rheological test so as to implement in our FE model the mechanical properties of the tumors thus obtained.

Simultaneously, other mice were intratibially injected with tumor cell in their right leg and with PBS in their left leg. After some times, animals were sacrificed and a first µCT of each bone was performed. They were then tested in compression and once again scanned.

Wanting to assess results on both lytic and mixed lesion, in addition to witness possibly different results between the two lesion types, cells provoking each lesion type were considered using the same protocol.

Based on the first µCT acquisition, FE models of each bone were created, tumor was manually segmented from bone and mechanical properties of tumor tissue obtained by rheometry was implemented in the FEA. Then the simulation results were compared to the experimental tests.

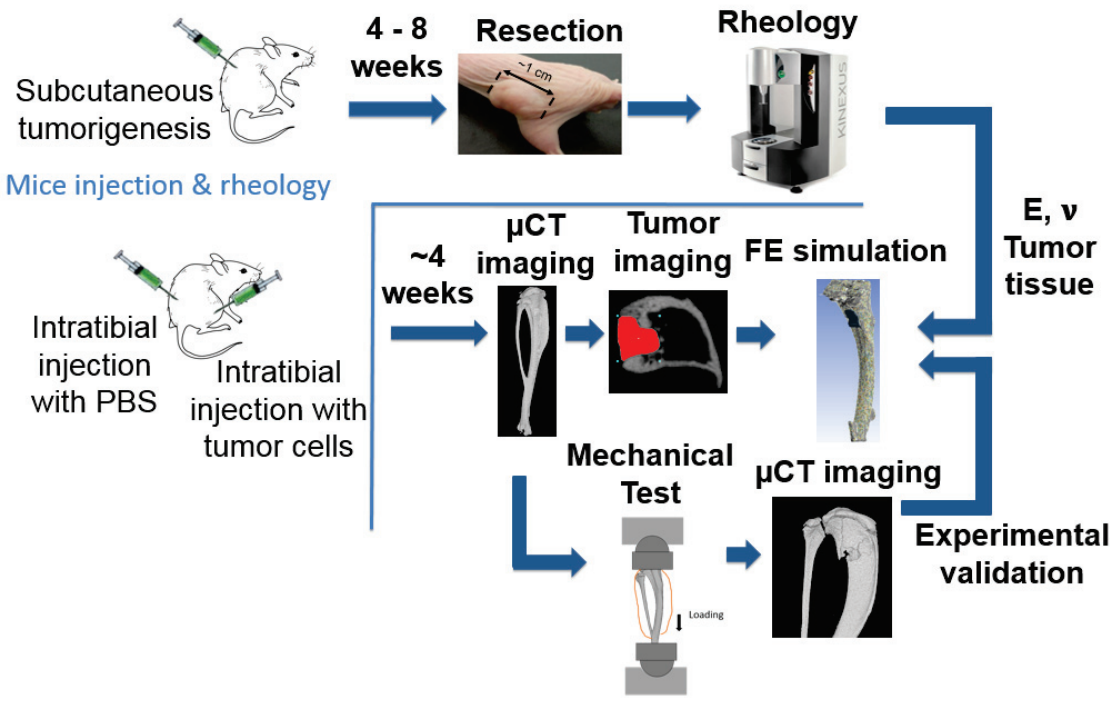

Figure 25: Global workflow of the project

2. *Mice injection (performed by Lamia Bouazza & Sandra Geraci)*

Mice injections followed protocols already in use in our group. They were of two types, subcutaneous to create testable tumor tissue samples, and intra-tibial in order to create tumor limbs. In anyway, animals had a week stabling before injection. This protocol received approval of University Claude Bernard Lyon I Ethical Comity for Animal Experimentation.

As tumor cells injected are coming from human stems, immunocompromised BALB/c nude mice (Janvier Laboratories®) were exclusively used in this study.

a. Tumor sample creation

After stabling, mice were anesthetized (induction box with a 1L air/min stream, 3% isoflurane concentration, then animals maintained with a mask at with the same stream, 2% isoflurane). They were then subcutaneously injected with human tumor cells (10^6 cells in 100µL PBS solution using 1mL syringe, Myjector (070151, Terumo Japan). The same technician performed all injections in order to ensure repeatable gestures. During injection, growth plate was taken as a reference point for needle injection depth.
After injection, tumor development was followed up though palpation, and as soon as possible, tumor measuring with a caliper. When the tumor reached about 1 cm in diameter without apparent necrosis, or when tumor growth stopped (in order to prevent necrosis), animals were anesthetized using once again isoflurane, sacrificed via cervico-dislocation, tumor was excised and stored in liquid azote to be tested on the same day.
The tissues surrounding the tumor (skin, fat, muscle) were also excised and tested in a similar way in order to compare the mechanical properties of these different tissues.

Human cells injected were of two types. First a lytic stem that is well studied in the lab (B02 GFP Bgal luc, breast cancer cells, called later on B02) and a mixt stem (CMET, H1993 MET luc 2, prostate cancer cells, called later on CMET). Mixed and lytic lesion type were studies to ensure that detection would be efficient on both lesion type

b. Tumor limbs creation

Among the different injection methods detailed in the state of the art part, the intra-tibial injection was chosen since, along with being well mastered in the lab, it allows creating a late stage of cancer, which is what we want to study. Moreover, it allows to the limit spreading to other bones and limbs and concentrate tumor development of a dedicated studied bone.

After their stabling week, 6 weeks old mice were anesthetized (induction box with a 1L air/min stream, 3% isoflurane concentration, then animals maintained with a mask at with the same stream, 2% isoflurane). Then mice were injected with different cell concentration depending on tumor cells in 15µL of PBS.
Number of tumor cells injected per stem was determined through a pre-study were different mice were iteratively injected with different concentration in order to obtain a repeatable lyse after around 30 days. Given this constrain, concentration injected were set at 10^6 cells for B02 stem and $8*10^6$ for CMET's.

Once gestation time reached, tumor development was assessed on plain radiographs, mice were sacrificed and limbs were excised *en bloc*, to be stored at -20°C until mechanical test.

3. *µCT imaging*

a. Acquisition

Micro CT imaging were performed on a Bruker Skyscan 1176 (Kontiche, Belgium) with a 10µm nominal resolution. Each limb was scanned at 10µm isotropic resolution (50kV, 500 µA, 0.5mm Aluminum filter, 0.6° rotation step on 180°).

Acquisitions were performed in air, in polystyrene sample holders. To prevent samples from drying during scanner time (approximately 8 minutes) they were surrounded with soaked in PBS gaze.

b. Reconstruction

Reconstruction was performed using scan constructor software (Nrecon 1.7.0.4, Bruker, Kontiche, Belgium) with a smoothing, ring artefacts correction and beam-hardening correction (parameters respectively set at 2, 6 and 20%, Figure 26).

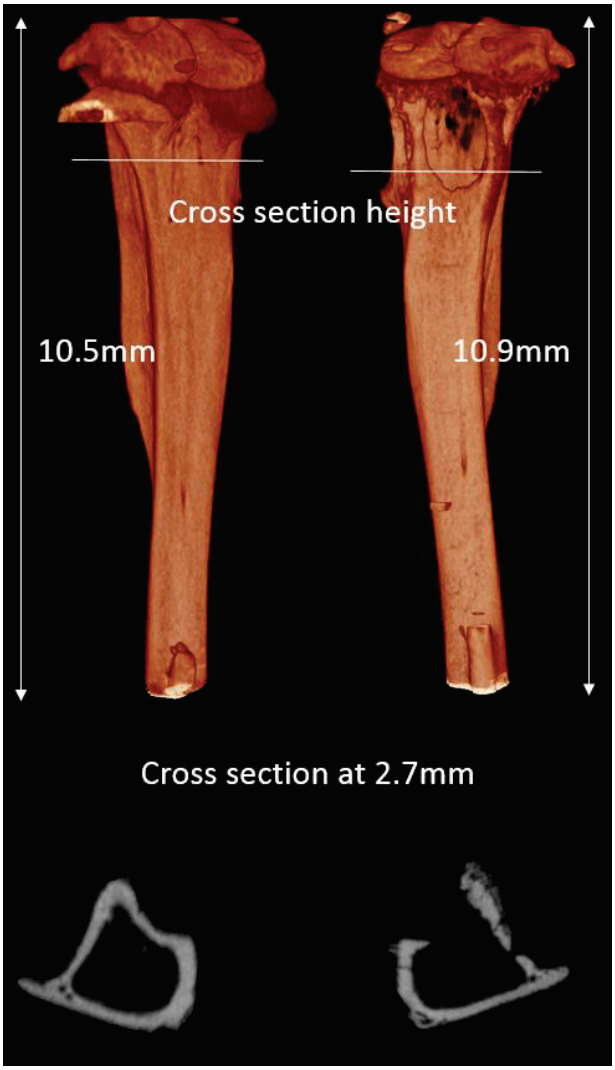

Figure 26: Reconstruction and cross section example (Mouse 6 Sham and Tumor limbs)

c. Images calibration

To ensure density/bone mineral density (BMD, g/cm^3) correlation, a classical phantom created by scanner manufacturer (Skyscan Brukker, Kontiche, Belgium) was used, providing two cylinders with known densities (0.25g/mm^3 and 0.75 g/mm^3). It was scanned in the same condition as the samples were, meaning in gaze soaked in PBS and in polystyrene sample holders and with the same parameters (50kV, 500 µA, 0.5mm Aluminum filter, 0.6° rotation step on 180°, 10µm resolution). Known densities were then linked to greylevels into the software during the analysis (CTAn, Skyscan).

4. *Mechanical tests*

a. Rheological tests on tumor and soft tissues (performed by Stéphane Nicolle)

Six BALB/c nude mice (Janvier Laboratories®) were subcutaneously injected following previous prescriptions, four with B02 cells and two with CMET cells (one tumor per mouse). When tumor reached the expected size, mice were anesthetized, sacrificed and tumor was excised along with other tissue samples (skin fat and muscles). All tissues were maintained in PBS until test.

Once resected, subcutaneous tumors were tested on the same day. Each tumor (~1cm in diameter ball) was sliced into 800µm thick slices using a home-made double-scalpel. Each slice was then placed between two glass slides equipped with a variable gap in order to precisely measure the thickness and the surface of the slice.
Each sample was then placed in a custom rheometer and subjected to a small-displacement harmonical shearing between 0.1 and 10 000 Hz. This kind of test allows to determine the frequency-dependent shear modulus (dynamic shear modulus) of the tissue.
Due to tumor size variation, number of slices varies among harvested tumor. In fact, first B02 tumor allowed slicing 4 slices, second allowed to slice 6, third 1 slice and fourth 2. CMET tumors respectively allowed obtaining one and two slices. Results on skin, muscles and fat respectively lie on 17, 15 and 7 slices, all mice included.

Obtained results are presented in Figure 27 (B02) and Figure 28 (CMET).

Interestingly, B02 tumor tissue showed stronger mechanical properties as its dynamic modulus (G*, quantifying the ratio of stress to strain under vibratory conditions) reached ten times fat one and two times skin and muscle ones.
Conversely, CMET tumor showed a slightly superior to fat dynamic modulus and roughly ten times inferior to muscles and skin.

Assuming that the deformation process is quasi-static during the test and that the tumor tissue has a linear elastic behavior in a first approximation, the low frequency modulus was chosen to characterize each tumor tissue in our specific FE models. Since Young's modulus is required in FE software when using a linear elastic law, the dynamic shear modulus was thus converted to Young's modulus by assuming that the tumor tissue is quasi-incompressible (Poisson ratio = 0.499) as it is usually assumed for other soft biological tissues. In this case, it is demonstrated that Young's modulus is equal to three times the shear modulus. The value of Young's moduli used for B02 tumors and CMET tumors in our specific FE models was then 0.0225 MPa and 0.00225 MPa respectively.

It is noteworthy that it was decided to determine tumor materials in dynamic in order to be able to perform more sophisticated simulation (as falls) if necessary later. However, converting a soft tissue dynamic modulus into a purely elastic module should not be a limitation as it was theorized by Fung (Fung, 1993). In fact, Fung specifies that "we can borrow the method of the theory of elasticity to

handle inelastic material" and "we can treat the [living tissue] material as one elastic material in loading" (p294)

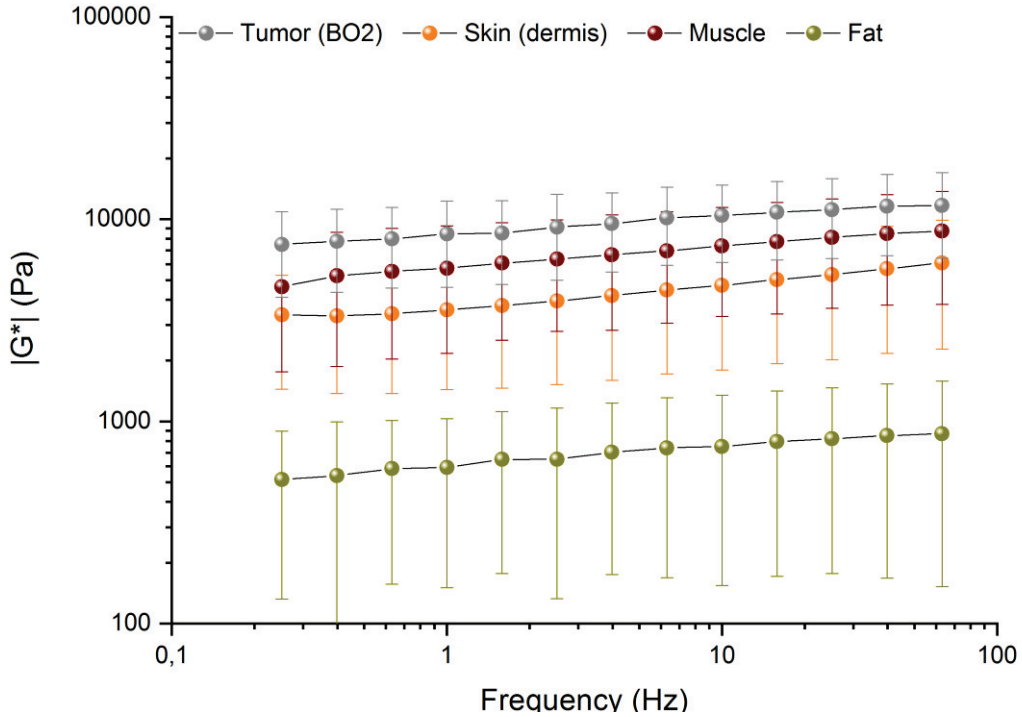

Figure 27: Dynamic modulus obtained for B02 tumor tissue (13 slices), skin (17 slices), muscle (15 slices) and fat (7 slices) of same mice.

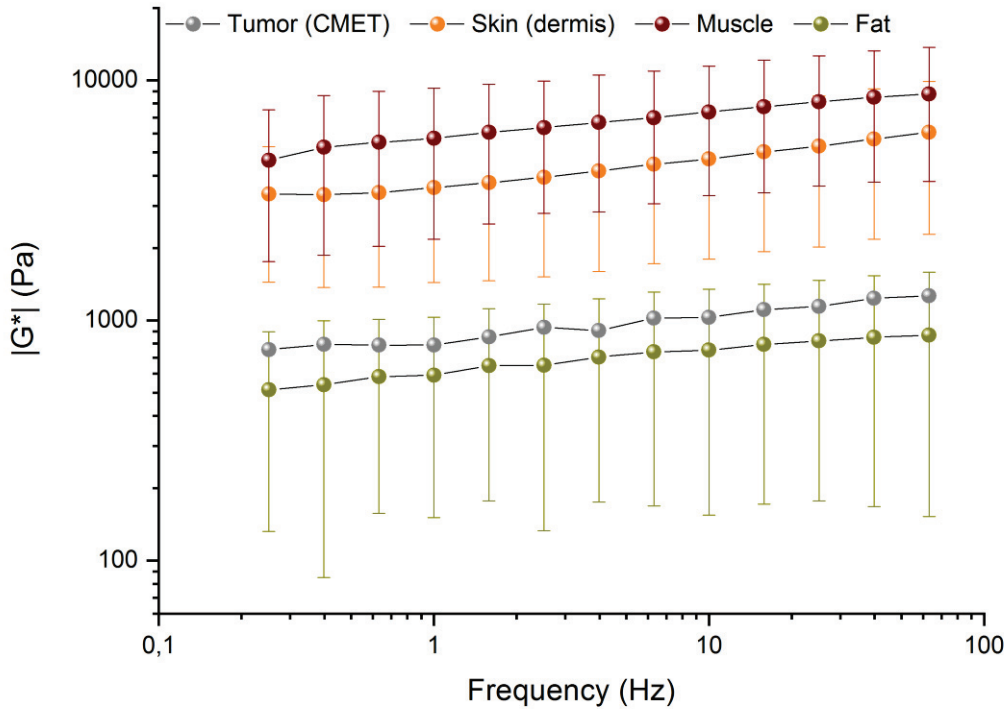

Figure 28: Dynamic modulus obtained for CMET tissue (3 slices), skin (17 slices), muscle (15 slices) and fat (7 slices) of same mice.

In addition, a Myeloma was resected on a bone cancer-suffering patient. This resection was operated during a hip stabilization, directly in resected bone, which could involve a light presence of bone. Thirteen slices were removed from the tumor. These slices were tested in the same way as those from mice. The measurement and the analysis were also similar (Figure 29).

The dynamic shear modulus of myeloma (0.3 MPa) was 10 times superior to that obtained for B02 tumor that grew up subcutaneously. This could reveal differences due to growing sites and thus limit the usability of modulus obtained on subcutaneous grown tumor samples. Alternatively, this could only be due to the differences in the tumor types.

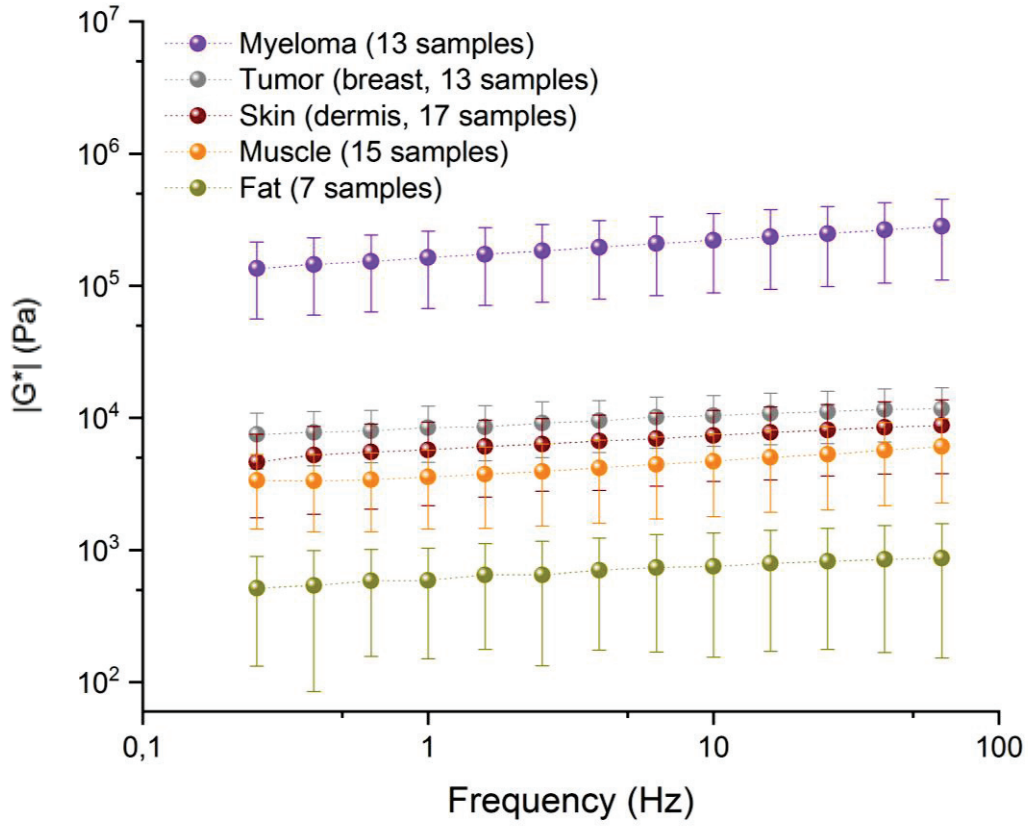

Figure 29: Dynamic modulus obtained for Myeloma tissue (3 slices), B02 tumor tissue (13 slices) skin (17 slices), muscle (15 slices) and fat (7 slices) of same mice.

b. Compression tests on tibia

Sample preparation

Once animal sacrificed, rear limbs were excised *en bloc* and frozen at -20°C in gauze soaked in PBS until the day prior to mechanical test. The day before the test, limbs were thawed at ambient temperature for half an hour. After this time laps, tibia was separated from the femur at the knee junction, and from the foot at the ankle, thus removing all tendons linking tibia muscle to other bones. Finally, the attachment between tibia and fibula was cut, but soft tissues surrounding tibia were kept in place in order to limit any possible damage to the tibia or tumor tissue. To avoid an excessive buckling, length of tibia was reduced and cut at half its height plus two millimeters and scanned using protocol previously detailed, letting a sample of approximately 8mm in length.
After scanning, the proximal end of the tibia was molded using fast epoxy paste (Pattex, Ref 1875423) and the distal end was imbedded by 2mm in the same paste and left to dry in soaked gaze for the night at 4°C.

The day after, proximal part mold was then glued to upper loading plateau while distal part was put in a custom metal piece, allowing sample to rotate.

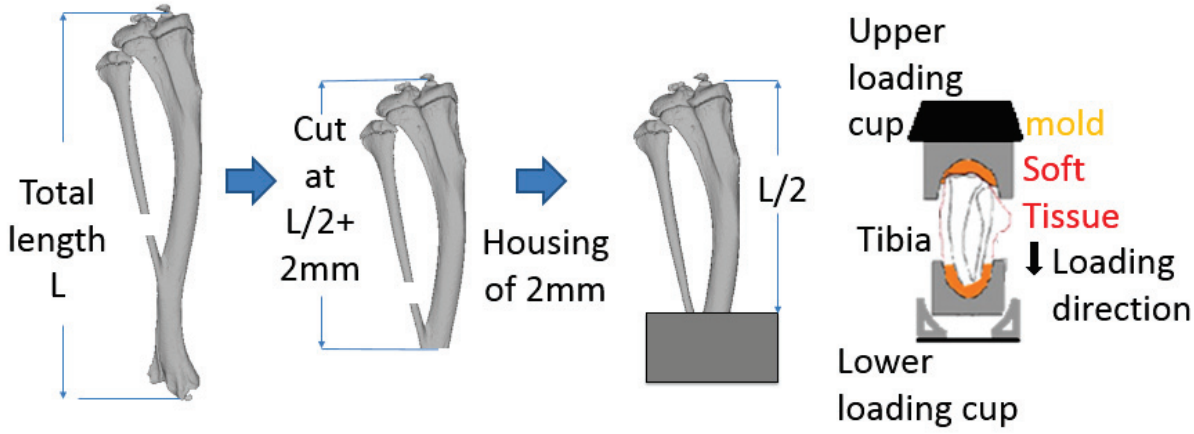

Figure 30: Sample preparation, tumor limb test V1. L~16mm

Once in place, the sample underwent a sinusoidal pre-cycling -0.5N and -2N for 30 cycles at 0.5Hz. The destructive test was conducted immediately after pre-cycling by compressing the tibia at a rate of 0.03 mm/s until failure using an electromagnetic testing machine (Bose Corporation, Eden Prairie, MN: 5500). Load-displacement data were recorded at 60 Hz (WinTest® Digital Control System) with a one-axis transducer (10 µm accuracy in displacement, 0.04 N in load). Load-displacement curves were analyzed to determine stiffness and ultimate load of each bone. To do so, a custom Python program was developed. Briefly, stiffness was determined by using the derivative of the experimental curve. It was determined using a linear regression on the longest interval where the derivative function variation was under ±5 N/mm (Figure 31). Ultimate load was defined as the maximum load measured by the load cell.

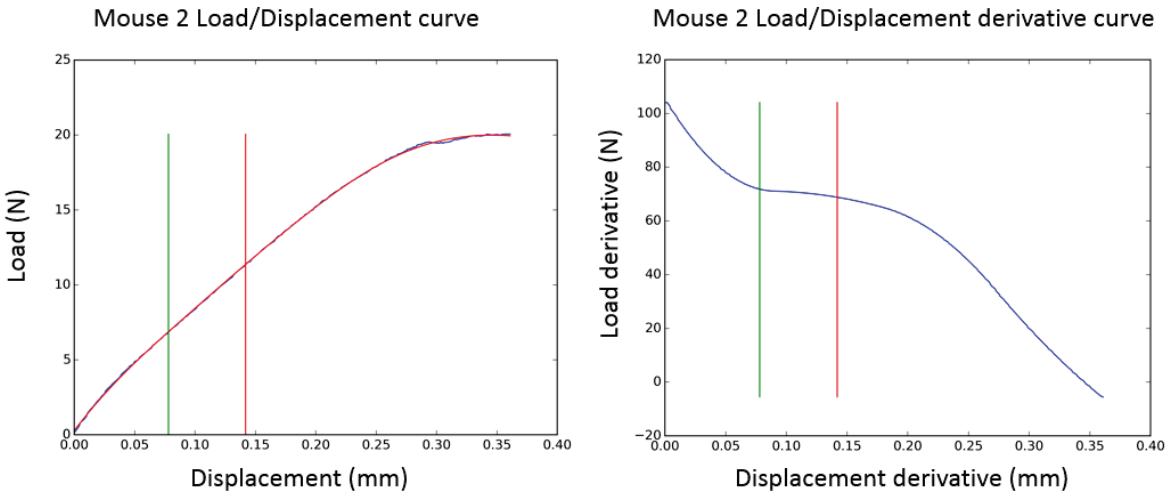

Figure 31: Mouse 2 load/displacement curve, load/displacement derivative curve and segment use to assess stiffness between vertical bars

5. *Necessity to inject contralateral limb with PBS*

A dedicated workflow was put in place in order to investigate the necessity to inject the contralateral limb and use it as a sham control in a comparative study (Figure 32). In fact, it is advised to do so (Wright et al., 2016, see chapter III part 9), but no investigation was apparently led. It was thus decided to add this research question to the present study.

To investigate this question, thirteen one-month-old female BALB/c nude mice (Janvier Laboratories®) were used, after the approval of University Claude Bernard Lyon I Ethical Comity for Animal Experimentation. Mice were divided into 3 groups.

Group 1 (n=4) was injected intratibially with PBS in both limbs, group 2 (n=4) was not injected, and group 3 (n=5) was injected intratibially with PBS in their right limb only (Figure 32).

At day 30, mice were anesthetized then euthanized by cervico-dislocation, both limbs were excised *en bloc* and stored in gaze soaked with PBS at -20°C until mechanical testing.

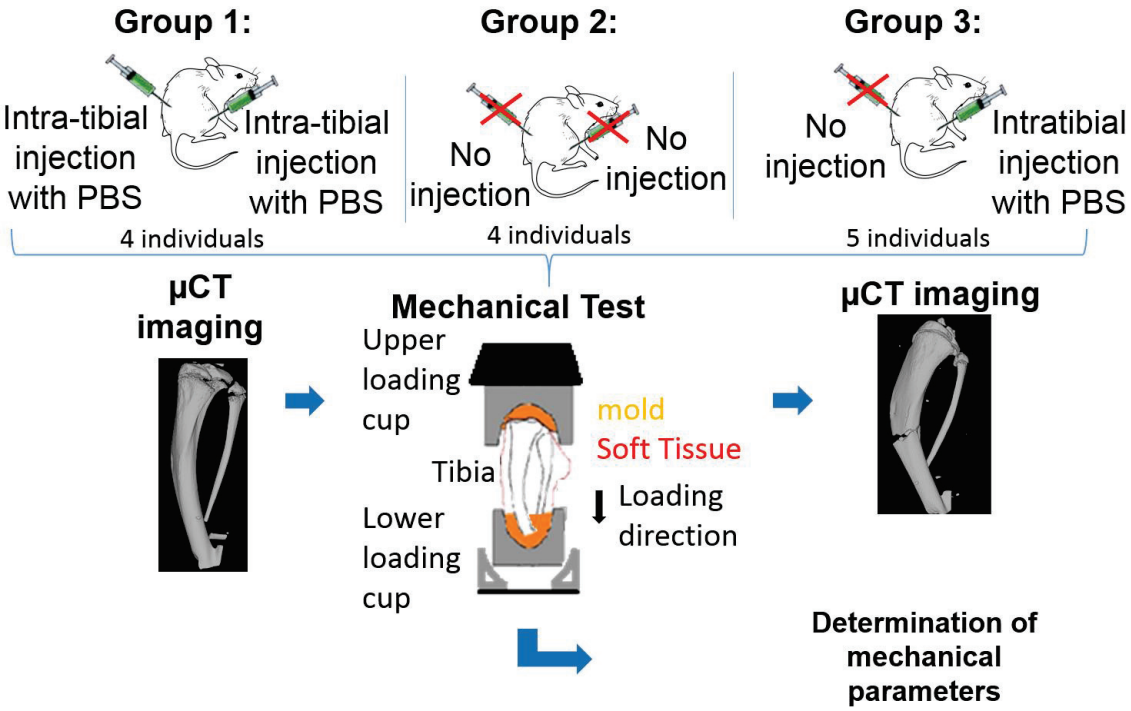

Figure 32: Necessity to inject contralateral limb with PBS workflow

Mechanical and imaging protocol detailed before were thoughtfully applied to each limb, and stiffness and ultimate load were obtained as previously mentioned.

To assess the impact of the injection on the mechanical properties, a Wilcoxon's test was performed on group 3, and a Mann-Whitney's test was performed on group 4 (=group1 + group2 + group3).

All the results are presented in table 1.
No difference between the right and left tibia of each individual was found for group 1 and 2 (respectively p=0.068 and 0.715 for the stiffness and 0.068 and 0.715 for the ultimate load). A significant difference was only found for ultimate load in group 3 (p=0.043).

Therefore, to increase the statistical power and show the effect of the injection, group 4 was formed with 3 cases: injected bone from both right and left tibia from group 1, non-injected bone from both right and left tibia from group 2 and only right tibia injected from group 3. Resulting in 13 injected limbs (8+5) and 13 non-injected limbs (8+5),

A significant difference was found between limbs for group 4 (p=0.029).

In order to improve significance of the difference between injected and non-injected limb, results were analyzed using Jepsen *et al.* guidelines (Jepsen *et al.*, 2015).

Quickly, a General Linear Model (GLM) was performed, with corrector parameter as a covariate. Jepsen *et al.* advise to use weight; however, in our case mouse weight did not show statistical agreement with the studied parameters. Thus, Bone Volume was quantified on constant 4mm zone for each bone (images were modified in order to ensure that bone were straight, then region of interest was set between the 210th and 617th images starting from tibial plateau), assuming a bone/background threshold at 0.63 HA g/mm^3.

Table 2: Mean stiffness, max load of each group, statistical significance of tests for each group and parameters;
inj.: injected; L: left; R:Right; n: number of mice.

	Group 1		Group 2	
n	4		4	
Tibia	inj. L	inj R	L	R
Ult. load (N)	19.9±1.9	14.4±2.2	22.9±3.9	21.3±3.7
p	0.068		0.715	
Stiffness (N/mm)	29.7±7.3	20.4±2.6	33.3±5.8	32±5.4
p	0.068		0.715	

	Group 3		Group 4	
n	5		13	
Tibia	inj.limb	non inj. Limb	inj.limb	non inj. Limb
Ult. load (N)	**23±3.4**	**26.7±5.1**	**19±4.5**	**23.9±4.7**
p	**0.043**		**0.029**	
Stiffness (N/mm)	31±7.2	29.6±4.8	27±7.5	31.5±5.1
p	0.686		0.158	

Unfortunately, due to an acquisition software instability, µCT scans of 4 bones were lost, allowing us to make the comparison on only 9 mice (18 tibia), of which 10 were injected and 8 were not.
Nonetheless, this test allowed to increase significance ($p<0.001$), showing a difference of 34% on ultimate load, the difference on the stiffness staying non-significant.

However, this study presents several limitations, the first one being that the muscles were not removed and could impact the results. This decision was made in order to respect the protocol of our main study, where muscles dissection is prohibited to avoid a discard of the tumor implanted in soft tissue. However, as all the ligaments and tendons were cut, this should not have a major impact. Another limitation is that we assumed from a statistical result on low effectives that there were no differences between each right and left limb. But, as the pooled groups for the Mann-Whitney's test were composed of 9 right limbs and 4 left for the injected group and 4 right limbs and 9 left for the non-injected one, this should avoid any unwanted repercussions on the results.
Moreover, the geometry differences could influence the results, but as the paired test on group 3 showed the same results as the impaired one of group 4, we can legitimately assume that this does not affect our results.
Lastly, a limitation was detected months later, as small variation in the loading led to a high variation on bone stiffness that could explain the non significance on the stiffness. This had less impact on the ultimate load and partially provoked changes in the protocol detailed in the next section.

In conclusion, this pre-study showed that the injection of contra lateral limb is mandatory in our comparative study, as the injection itself induces a 34% reduction of the ultimate load.

As previously said in state of the art part, these results were published in a supplement issue of Computer Methods in Biomechanics and Biomedical Engineering (Delpuech *et al.*, 2017).

a. Sample preparation and loading fixtures changes

Following the investigation of the necessity to inject contro-lateral limbs with PBS, mechanical protocol was improved in several ways.

First, 5mm classic bolt were replaced with 5mm one-eyed bolt. This allowed to keep the bone intact, while keeping the same resulting sample height as one-eyed bolt are deeper than there classical counterpart. Both compression plateau were countersink, creating a double ball joint.

Epoxy paste used for the housing was replaced with methacrylate glue with quicker take (VariDur ref 10-1027, Buehler, USA), speeding test to a day against two (sample preparation on the first day and test the day after).

Finally, the first scan was performed after housing of the tibia, allowing having its exact length once housed along with its orientation.

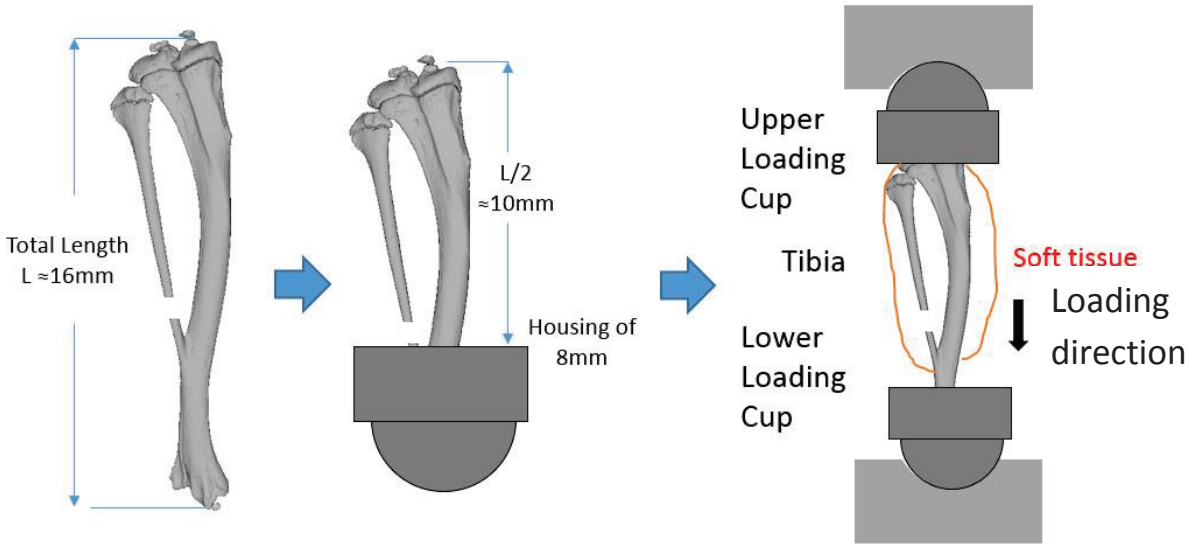

Figure 33: Sample preparation, tumor limb test V2

It is to be noted that the first version of the sample preparation and loading fixtures (presented in part 5.b.) was used only for the tests led to prove the necessity of the injection of the contralateral limb, while the ones presented in the present section was used for all subsequent samples aiming to answer our hypothesis. Apart from sample preparation changes and loading fixtures that were presented in this part, mechanical test modality stayed the same as in first version.

6. *FEA simulation*

a. Model creation

Each step of the FE model creation is presented in Figure 34.

First, based on reconstructed and straightened µCT scans, the volume occupied by each bone was converted to generic surface mesh (STL files) using scanner manufacturer software (CTan 1.16.4.1+, Skyscan Bruker, Kontiche, Belgium) and an open source software (3DSlicer 4.8.1, various developers). This surface mesh was then converted to a volume and meshed using tetrahedron elements on a FEA software (Ansys 19.0, Ansys inc., Canonsburg, Pennsylvania, USA). Academically developed software was then used to correlate bone density to Young's modulus of each element of the model (Bonemat, Istituto Ortopedico Rizzoli, Bologna, Italy). To finish, volume mesh with implemented Young's modulus were taken back to Ansys, in order to perform FEA.

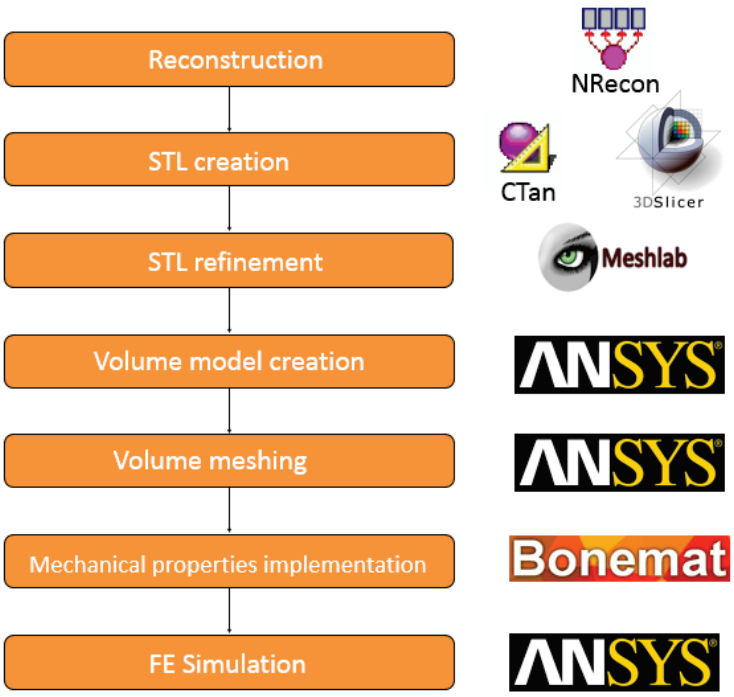

Figure 34: FE model creation process

b. Model creation specificities

First to intervene in the process, CTan was used to automatically segment bone from background, thanks to a custom macro that was developed in the laboratory. Providing better images/stl conversion than CTan, 3DSlicer was then used to create the surface mesh from the segmented images.

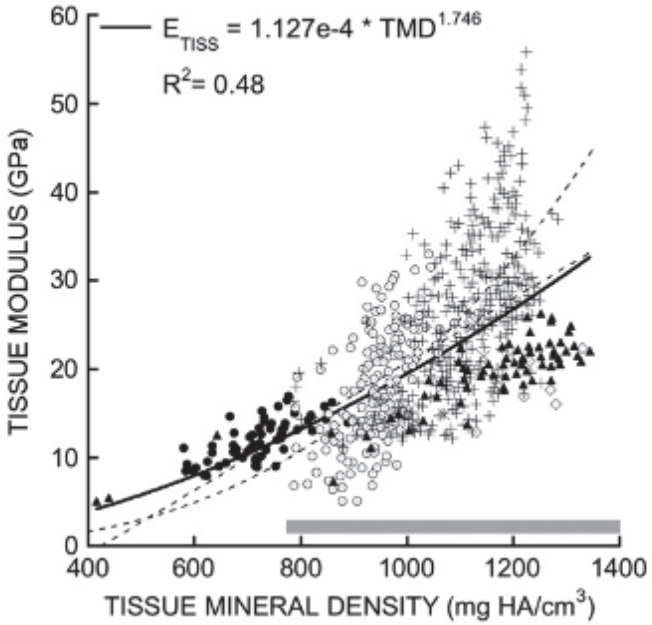

Figure 35: Easley et al. equation to convert apparent density to Young's modulus

This surface file was then refined on MeshLab, a STL modification dedicated software, to reduce process time while converting surface to volume in Ansys, allowing volume meshing of the bone. The subsequent mesh element Young's modulus was correlated to Young's modulus using a conversion equation from literature. This power law was developed on various species bone sample by Easley *et al.* (Easley *et al.*, 2010) and validated on mice tibia by Yang *et al.* (Yang *et al.*, 2014) while functioning quite as good on mice vertebrae as equation chosen by Nyman *et al.* (Nyman *et al.*, 2015). This equation is presented in Figure 35 and implies a purely elastic behavior for the model. Finally, the model was taken back to Ansys in order to perform FEA, which specificities will be overviewed in the next section.

c. FEA specifications

In order to mimic the experimental test, the first millimeter of the bone was selected and set as a rigid body. In the first step, an axial force equal to the ultimate load was applied to this selection while the distal bone elements were fixed, to get as close as possible to an imbedding.

From this first simulation, stiffness is assumed to be the slope linking the origin to the point representing the maximum displacement due to the applied load. Most of the time, this stiffness was far from the one that was obtained experimentally. The force was then modified, implementing contribution on X and Y axes, information not measured during the experiments (uniaxial force sensor). The limit for those contributions was set at 20% of the axial force for the sum of the loads on X and Y axes. Iterating loads, experimental stiffness was identified. The failure was then assessed using a modified Pistoia's criterion (Figure 37, see next section for failure criterion parameters).

Identification of stiffness on experiments implies that results obtained are tuned only for this particular model.

Then, two different types of model were created, one converting grey levels in the images into tumor mechanical properties as proposed in the literature (Keyak *et al.*,

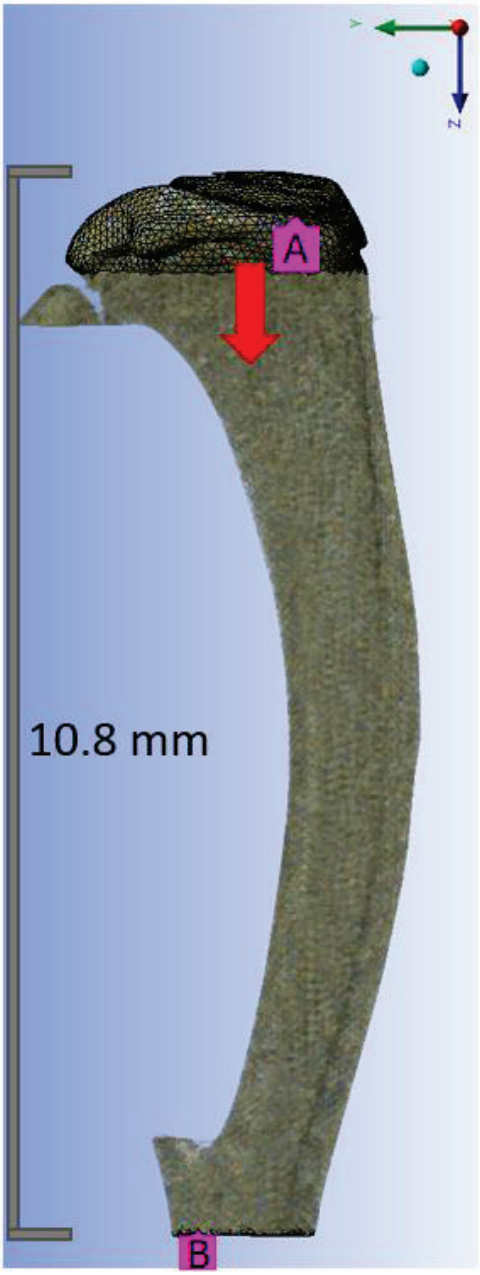

Figure 36: Boundary condition application. A, elements on which the load is applied, B, elements on which the displacement is forbidden to mock an imbedding.

2005), called “heterogeneous”, the other taking into account tumor tissue mechanical properties (obtained by rheometry) called “specific”. Both will be discussed in the next section.

d. Heterogeneous model

Models that will be called “Heterogeneous models” in this study are the ones that followed Keyak *et al.* workflow (Keyak *et al.*, 2005). In this model, no separation between tumor and bone was made, and all Young’s moduli were given to each elements according the previous power law (Easley *et al.*, 2010). Only a threshold at 0.31 HA g/mm^3 was applied in order to prevent unrealistic Young’s modulus in the shaft due to beam hardening effect. These models were created for all bone categories of this study.

e. Specific model

Unlike their heterogeneous counterpart, “Specific models” were created exclusively for tumor bone. The first specific step of their creation (once bone segmented) was to segment tumor from the bone, assuming that tumor tissue would be where the bone disappeared. The resulting volume was subtracted to the bone volume and both were meshed independently.

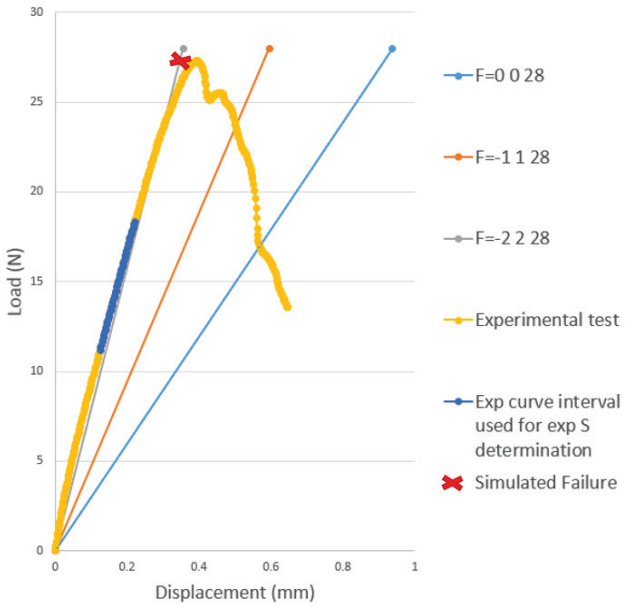

Figure 37: Example of a few iterations and determination of failure via simulation on a sham limb. Load applied expressed as F=(X,Y,Z) in N

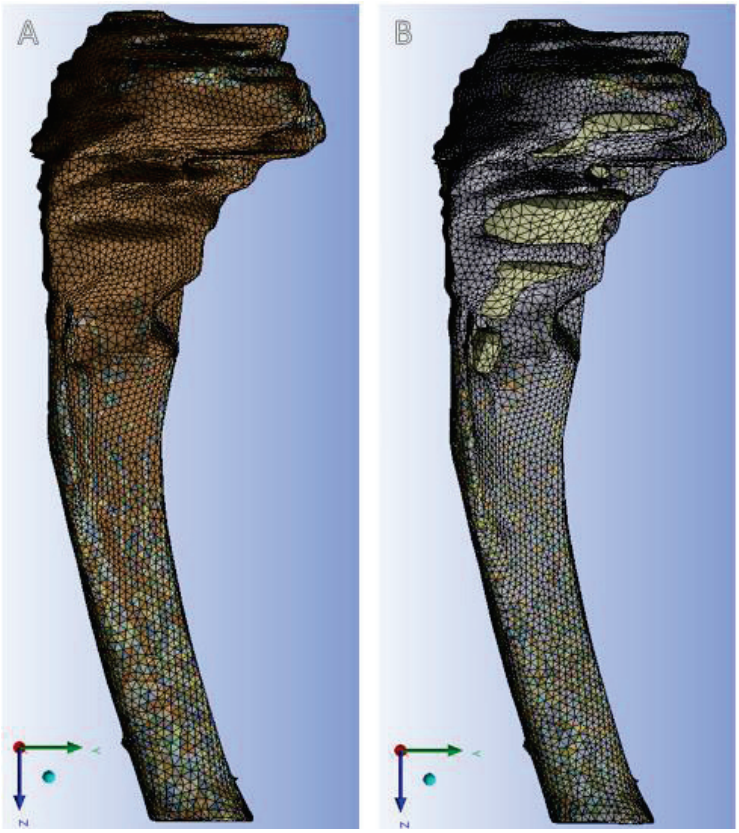

Figure 38: Heterogeneous (A) and Specific (B) model of the same tumor bone, tumor in light green

Bone volume mesh elements were given Young's modulus the exact same way heterogeneous model did, but the tumor was implemented with its own properties obtained via rheological test described in part "Mechanical tests".

f. FEA quality assessment

Various aspects of our FEA had to be assessed in order to ensure models answer quality and are developed below.

Mesh element size convergence study

As it was said, it is generally agreed that an optimal mesh density exists, allowing to have the most accurate solution with the smallest possible amount of elements (Burkhart *et al.*, 2013). It is commonly determined through the use of a convergence study (Burkhart *et al.*, 2013).

This convergence study was led on the same bone, meshed with a different number of elements. Studied models included 10 K, 100 K, 200 K, 300 K, 400 K and 500 K elements. Bonemat, that did not support finer models, imposed the finest model. To prevent a double variation due to variation in element size between models and variation in mechanical properties, a constant Young's modulus of 20GPa was applied with a threshold at 0.31HA g/mm^3. First, the sensitivity was led on ultimate load calculated with Pistoia's criterion (failure assessed when 2% of the total volume reaches 0.007 strain). Unfortunately, as it can be seen on Figure 39, ultimate load proved to be too stable.

As Pistoia's criterion is based on strain, the same work was led on average strain energy density, which is more sensible and gave more interesting results (Figure 39).

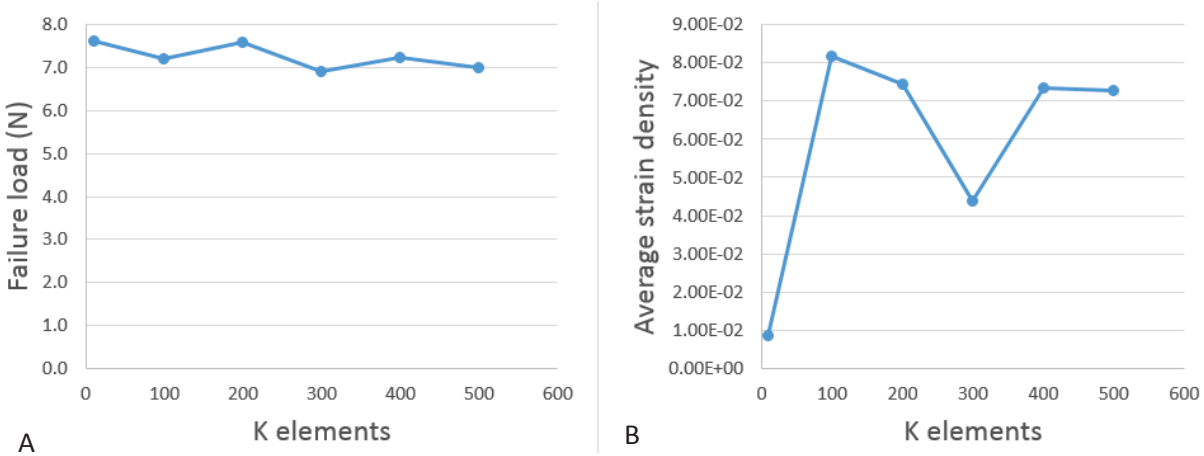

Figure 39: Sensitivity study on Failure load (A), and strain energy density (B).

As the 200K element model was quite close from the 500K one (8% of difference on failure load and 2% on average strain density) and was way lighter to manipulate, it was chosen based on these results. On what is left free of mice tibia with our protocol, this gives elements of average 0.0001mm^3 in volume, a mean surface element of 0.018mm² and an average edge of 0.18mm.

The difference that can be noted on the 300K elements model regarding average strain energy density may be due to poor quality elements that strained more in said model than others.

Number of materials sensitivity

As it was left alone on the previous sensitivity study, the effect of materials number in the model was quantified at a constant number of elements, which is 200K according to the previous result.

Three different number of material were tested, 10, 80 and 190 (on the interval of 22 to 2.3 GPa that bone presented after thresholding). The results were stable and as 190 materials was manageable, it was selected. It has to be noted that Bonemat does not allow giving a number of materials but a span between two materials, thus the gap was set at 150 MPa, in order to obtain approximately 200 materials, depending on grey scale repartition.

Failure criterion parameters determination and validation against experimental test

As our model is purely elastic, no damage to the elements is recorded and a criterion is needed to assess failure. Pistoia *et al.* proposed such a criterion on human radii, and defined failure to be reached when 2% of the bone meshed volume reach 0.007 in strain or more (Pistoia *et al.*, 2002). Nyman *et al.* reworked it in order to adapt it to mice vertebrae (Nyman *et al.*, 2015).

Using the same idea, all heterogeneous models were pooled (n=43) and the criterion parameters were changed in order to identify the one allowing the best agreement between experimental and simulated ultimate load. To do so, failure volume (FV) was set at 2, 4 and 6% while failure strain (FailStrain) was set at 0.007, 0.0085, and 0.01.

The same way Nyman *et al.* did, RMSE is to be minimized, while R^2 has to be as close as one as possible. One parameter was added to the comparison: the slope that has to be as close as one as possible in order to avoid under or overestimations on failure load. Global results are shown on Figure 40.

Lowest RMSE (3.2) was witnessed for FV=4% and FailStrain =0.0085, however, FV=2% FailStrain =0.01 RMSE was really close (3.3) and showed a better R^2 and slope (respectively 0.65 against 0.63 and 0.70 against 0.62). Accordingly, the parameters for assessing our failure load will be set at 2% for FV and 0.01 for FailStrain. Same parameters were reported to be the most suitable to assess mouse vertebrae failure using Easley *et al.* equation by Nyman *et al.*, showing agreement with literature.

To conclude this part, our FEA showed stability as well as good agreement with both experiments and literature.

g. Statistical analyses

Statistical analysis was performed in R (R 3.5.1, R Development Core Team (2005)) using a significance level of 5 %.
All tests were two-tailed. Results are reported as scattergram and Bland-Altman representation. Bland-Altman differences were calculated as Experimental ultimate load−Numerical ultimate load

values. Orange lines represented the lower and higher limit of agreement (95 % confidence interval (CI) of limits of agreement: average difference ± 2 standard deviation of the difference) and the mean line was set in grey. Statistical correlations between experimental and FEA ultimate loads were assessed using the Spearman's rank correlation ($\rho_{spearman}$) test while belonging to the same group was ascertained by the Mann-Whitney unpaired test.

The ability of FEA to predict sample ultimate load was ascertained by linear regression to determine the intercept, the slope and the Root Mean Square Error (RMSE, representing the square root of the differences between experimentally measured peak force and simulated failure load of each tibia.

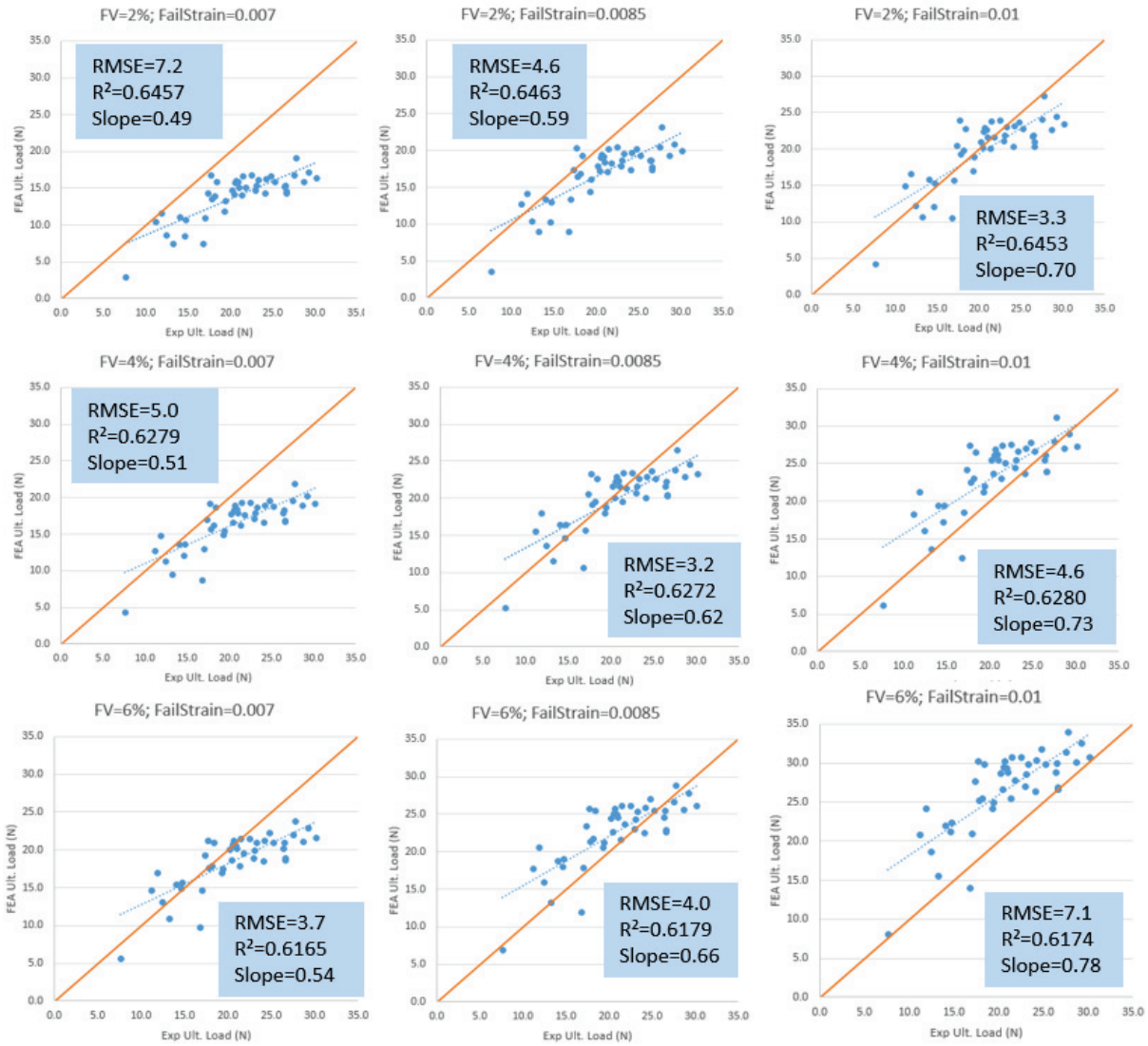

Figure 40: Sensitivity study on failure criterion parameters, FV (Failure Volume) exceeding Failstrain (strain at failure).

7. *Methods summarizing*

- **Mice injection**

  - **Tumor sample**

    After one week stabulation, 6 Balb/c nude mice were anesthetized and injected with different tumor cells. 4 were injected with B02 (lytic) tumor cells and 2 with CMET (mixed) tumor cells. Once tumor reached 1cm in diameter, animals were sacrificed and tumor tested using rheology

  - **Tumor limbs**

    After one week stabulation, 16 Balb/c nude mice were anesthetized and intratibially injected with different tumor type in their right limb and with PBS in their left. Half were injected with B02 tumor cells in their right limbs and the other half with CMET. After 4 weeks, animals were sacrificed and limbs were kept at -20°C in PBS soaked gaze until mechanical tests.

- **µCT imaging**

  - **Acquisition**

    All µCT imaging were performed on a Bruker Skyscan 1176 (Kontiche, Belgium) with a 10µm nominal resolution. Each limb was scanned at 10µm isotropic resolution (50kV, 500 µA, 0.5mm Aluminum filter, 0.6° rotation step on 180°).

  - **Reconstruction**

    Reconstruction was performed using scan constructor software (Nrecon 1.7.0.4, Bruker, Kontiche, Belgium) with a smoothing, ring artefacts correction and beam-hardening correction (parameters respectively set at 2, 6 and 20%).

- **Mechanical Tests**

  - **Rheological tests on tumor**

    Rheological tests were performed on biologically induced tumor samples and a myeloma sample from a patient. Said tests allowed finding dynamic shear modulus that was then converted to Young's modulus. Found values were of 0.0225 MPa for B02 tumor, 0.00225 MPa for CMET tumor and 0.3 for myeloma.

  - **Mechanical tests on tumoral limbs**

    Following dynamic pre-cycling (sinusoid between -0.5N and -2N for 30 cycles at 0.5Hz), samples were tested until failure in compression in quasi-static (0.03 mm/s). Load-displacement data were recorded at 60 Hz from these tests, using a one-axis transducer (10 µm accuracy in displacement, 0.04 N in load).

- **Necessity to inject contralateral limb**

  Necessity to inject contralateral limb (with PBS) in a comparative study was proven during this project (Delpuech *et al.*, 2017).

- **FEA simulation**

  - **Model creation**

    Model creation consisted in a bone segmentation, followed by a geometrical meshing creation and a correlation between each element Young's modulus and local bone density (Easley *et al.*, 2010).

  - **FEA specifications**

    The first millimeter of the bone (tibia plateau) was set as a rigid body and ultimate load was applied on elements constituting this rigid body.
    The last element raw (distal part) were set with no displacement.
    These two boundary conditions allowed recreating mechanical test.

  - **Model types**

    Two different models were created, one for all limbs types (injected with PBS or tumor cells): Heterogeneous model. This model correlated elements Young's modulus with bone local density for the entire structure (no differentiation of potential tumors). The second: Specific model, was dedicated for tumor limbs. In this model, bone was segmented from tumor and bone elements were correlated with bone local density, while tumor elements were implemented with tumors Young's modulus.

  - **FEA validation**

    Various aspects of FEA parameters had to be validated. Optimal elements number was set at 200 000 after a convergence study. Number of materials was set around 200 (using a step of 150MPa between two materials) after the same step.
    Lastly, failure criterion was optimized in a comparative study, assessing failure when 2% of the elements volume reached 0.01 in strain.

V. Lytic tumor limbs

1. *Introduction*

As stated at the end of the literature review, the aim of this part is twofold. First, we wanted to know if a FE model accounting for specific tumor properties would help to better predict failure of tumoral bone on lytic lesions. Second, we aimed to test if a simple FE model (linear elastic) could help on the mechanical stability evaluation of bones with lytic lesion.

2. *Material and methods*

Two groups were created (Figure 41). First, Eight BALB/c nude female mice were injected with tumor cells (B02, human tumor cells) in their right limbs and PBS in their left to create sham limbs. Secondly, in order to provide indisputable sham limbs, eight other BALB/c nude mice female were injected in both limbs with PBS. This way the results of this batch would not be affected by any tumor cell migration, and bone would develop in a non-cancer fitting body. For convenience, this last eight animals batch will be furtherly referred to as “control” limbs, while contralateral PBS injected limbs will be referred to as “sham” limbs. Bone injected with tumor will logically be referred as “tumor” bone.

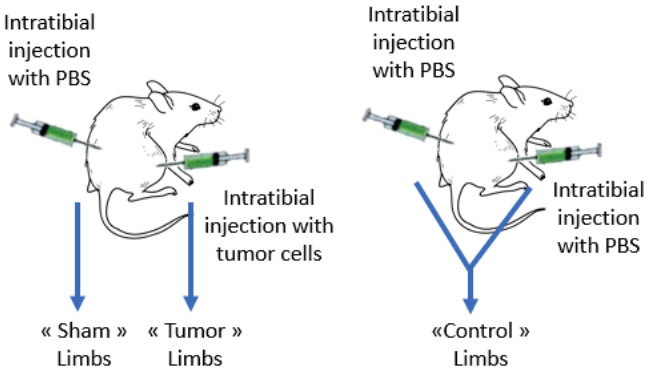

Figure 41:Mice batch denomination depending on injection type

Animals were injected, and thoughtfully monitored for four weeks. After four weeks they were sacrificed and rear limb were excised *en block* and frozen at -20°C in PBS soaked gaze. Limbs were only unfrozen on the day they were tested and scanned prior to and after experimental test (see chapter III for experimental details). Unfortunately, Mouse 9 left limb experienced a fall from the experimental machine plateau and was thus taken off the study.

Once limbs tested, numerical models were created lying on µCT scans acquired before test. Only one model (heterogeneous) was created for control and sham limbs, were bone Young’s modulus was correlated to hydroxide apatite concentration (Easley *et al.*, 2010). The same model (heterogeneous) was created for tumor bone not taking care of tumor tissue (Keyak *et al.*, 2005). A second model was created for tumor tissue were bone was segmented from tumor manually, the bone received Young’s modulus the same way heterogeneous model did, while tumor was implemented with tumor specific Young’s modulus, obtained via rheology (specific model).

These two models being purely elastic, failure was assessed with a failure criterion inspired by Pistoia *et al.* (Pistoia *et al.*, 2002) and supposed to occur when 2% of the meshed bone volume exceed 0.01 in strain (see part 9 of the present chapter).

Finally, wanting to quantify FEA accuracy on each injection case, simulations were assessed against experimental ultimate load for each injection case.

3. *Comparison between B02 sham and control limbs*

After observation, images of sham limbs did not show any propagation of lyse from contralateral tumor limbs.

In order to detect differences between the two groups (sham and control), that would not appear on visual images comparison the experimental ultimate load of the two groups were compared. As the exact load, identified via FEA, is different for each sample (see chapter III part 6 c, and Figure 37), the ultimate load should not be comparable by itself and should need a correcting parameter.

Unfortunately, samples ultimate loads were not correlated with the identified norm of the strength on Y and X, neither were they with each force by itself (Spearman' test non significant for each parameter).

Therefore, it was decided to see if the X and Y norms were significantly different for the two groups (sham and control), which they were not (Mann-Whitney's test non-significant). This allowed us to consider that the load shift was randomized enough to not have a repeatable effect on ultimate load and thus, compare them without correction.

Hence, ultimate load of the two groups were directly compared using a Mann-Whitney's test. The said test was non-significant (Figure 42), finally allowing us to pool the two groups and to validate their simulation as a whole.

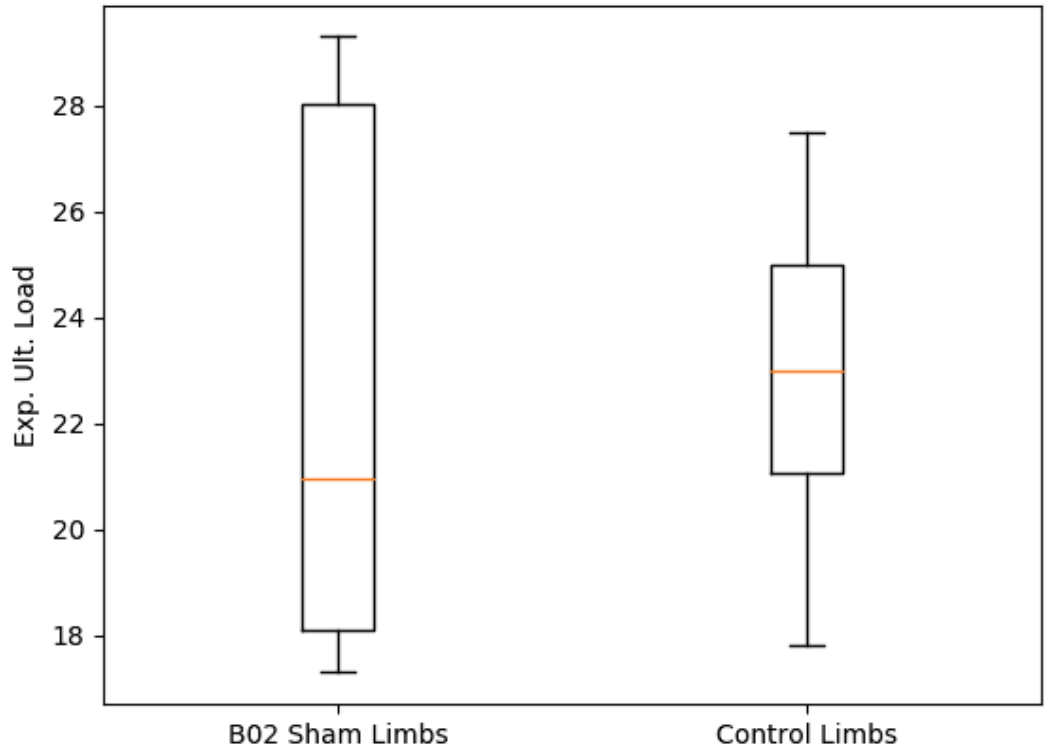

Figure 42: Box plot of sham and control ult. load and Mann-Whitney comparison test result

4. *Heterogeneous model results for sham control limbs*

Failure results for sham and control limbs for experimental tests and simulation are presented in Table 3.

It has to be noted that all mice from the control batch were ordered at the exact same time (that is not the case of other mice constituting a batch). In addition mice were injected only with PBS (no different development due to individual differences). Thus, all failure load values are close from each other.

Table 3: Experimental and simulation (heterogeneous) results for each control and sham limbs

	Mice	Experimental Ult. Load (N)	FEA Ult. Load (N)	Difference percentage between exp and FEA (%)
Sham limbs	Mouse 1, L. limb	19.4	17.0	12
	Mouse 2, L. limb	17.8	23.9	34
	Mouse 3, L. limb	18.2	19.8	9
	Mouse 4, L. limb	17.3	20.4	18
	Mouse 5, L. limb	27.8	27.3	2
	Mouse 6, L. limb	29.3	24.4	17
	Mouse 7, L. limb	28.7	22.6	21
	Mouse 8, L. limb	22.5	24.0	6
Control limbs	Mouse 9, R limb	24.1	20.3	16
	Mouse 10, R limb	23.4	23.0	1
	Mouse 10, L limb	26.6	20.9	22
	Mouse 11, R limb	17.8	19.2	8
	Mouse 11, L limb	21.4	20.0	7
	Mouse 12, R limb	21.9	21.5	2
	Mouse 12, L limb	21.5	23.8	11
	Mouse 13, R limb	20.4	20.2	1
	Mouse 13, L limb	25.2	22.7	10
	Mouse 14, R limb	20.7	22.8	10
	Mouse 14, L limb	26.4	21.8	18
	Mouse 15, R limb	19.4	18.9	2
	Mouse 15, L limb	23.0	21.1	8
	Mouse 16, R limb	24.8	23.7	5
	Mouse 16, L limb	27.5	24.0	13

Pooled results for control and sham limbs are presented in Figure 43

Simulation and experimental tests showed good agreement (mean difference percentage of 11±8%). The fact that all results were close for control limbs (SD=6% for 16 control limbs against SD=10% for 8 sham limbs experimental ultimate load) led to a low R^2 (0.33) and a slope far from 1 (0.35). RMSE however stayed low (3.1).

To be sure that the two value were correlated despite low R^2, a Spearman test was performed on data and was highly significant ($\rho_{spearman}$=0.60; p=0.003), allowing the validation of FEA results.

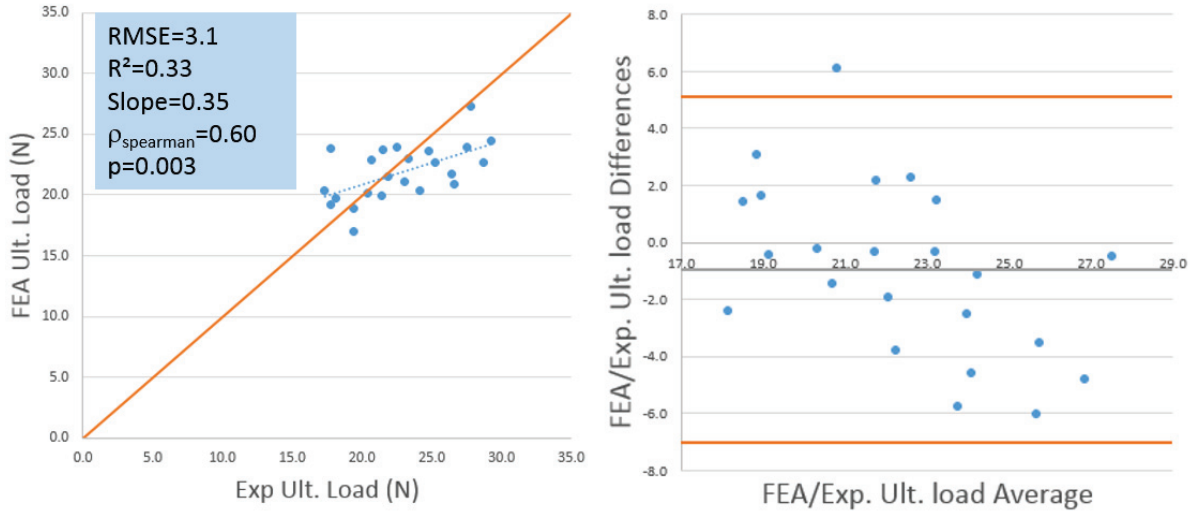

Figure 43: Comparison between Exp. and FEA failure load for heterogeneous models of sham and control limbs (n=23 limbs)

Search of potential differences between left and right limbs of control limbs experimental ultimate load values was led after sample batch differences check. It showed a significant difference between right and left limbs of control group batch.

However, it disagreed with the result found in the validation of the necessity to inject contralateral limb (Chapter IV part 5) and more importantly with literature results lying on a larger sample pool (no differences found between 14 Balb/c left and right tibia ultimate load (Holguin *et al.*, 2013))

Due to this disagreement, it was hypothesized that the difference found was accidental and results were kept pooled.

5. *Heterogeneous model results for tumoral bone*

Failure results for tumoral limbs for experimental tests and simulation are presented in Table 4.

Once again, heterogeneous model showed good agreement with experiments, with the exception of mouse 8 tumor limb. An explanation for this previously unseen difference will be detailed later (see part 9 of the present chapter).This particular result was taken off the comparison between FEA and experimental results to be fully exploited later. Disparity in results due to the difference of tumor development between individuals allowed to obtain good R^2 (0.85), along with an acceptable slope (1.32) and a comparable RMSE (3.0). A spearman's test was led for comparison mater with the previous section ($\rho_{spearman}$=0.75; p=0.05). Mean percentage difference between experimental and FEA ultimate load was of 12±7% (Table 4 Figure 44).

Table 4: Experimental and simulation (heterogeneous) results for each Lytic tumor limbs

	Mice	Experimental Ult. Load (N)	FEA Ult. Load (N)	Difference percentage between exp and FEA (%)
Tumor limbs	Mouse 1, R. limb	20.2	21.0	4
	Mouse 2, R. limb	20.6	22.4	10
	Mouse 3, R. limb	7.7	4.2	19
	Mouse 4, R. limb	13.3	10.6	15
	Mouse 5, R. limb	18.4	22.7	15
	Mouse 6, R. limb	12.5	12.2	1
	Mouse 7, R. limb	11.9	16.5	16
	Mouse 8, R. limb	7.7	18.3	47

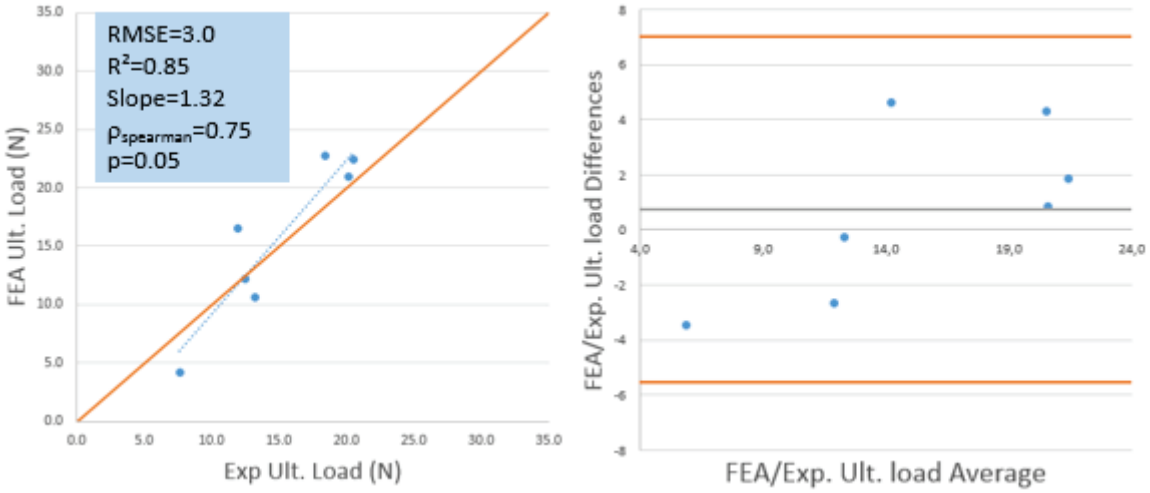

Figure 44: Comparison between Exp. and FEA failure load for heterogeneous models of tumor limbs (n=7 limbs)

6. *Specific model results for tumoral bone*

For the same reason as for heterogeneous model mouse 8 was taken off the comparisons between experimental and FEA failure, to be dealt with later (see part 9 of the present chapter).

Young's modulus used for tumor was of 0.0225 MPa.

Unlike their heterogeneous counterpart, specific model did not show good agreement with experimental results. In fact, difference percentage was of 23±22% and R^2 of 0.79 and Spearman's test was significant ($\rho_{spearman}$=0.77; p=0.04).
To assess differences with model implemented with Young's modulus derived from tissue harvested in real patient, same models were implemented with tumor Young's modulus obtained on myeloma resected from a patient (Table 6).

Table 5: Experimental and simulation (specific) results for each Lytic tumor limbs. Removed limb for FEA validation in light grey

	Mice	Experimental Ult. Load (N)	FEA Ult. Load (N)	Difference percentage between exp and FEA (%)
Tumor limbs	Mouse 1, R. limb	20.2	21.1	4.4
	Mouse 2, R. limb	20.6	21.1	2.4
	Mouse 3, R. limb	7.7	3.7	52.2
	Mouse 4, R. limb	13.3	13.1	1.6
	Mouse 5, R. limb	18.4	22.0	19.7
	Mouse 6, R. limb	12.5	7.4	40.5
	Mouse 7, R. limb	11.9	17.0	42.3
	Mouse 8, R. limb	7.7	17.9	133.9

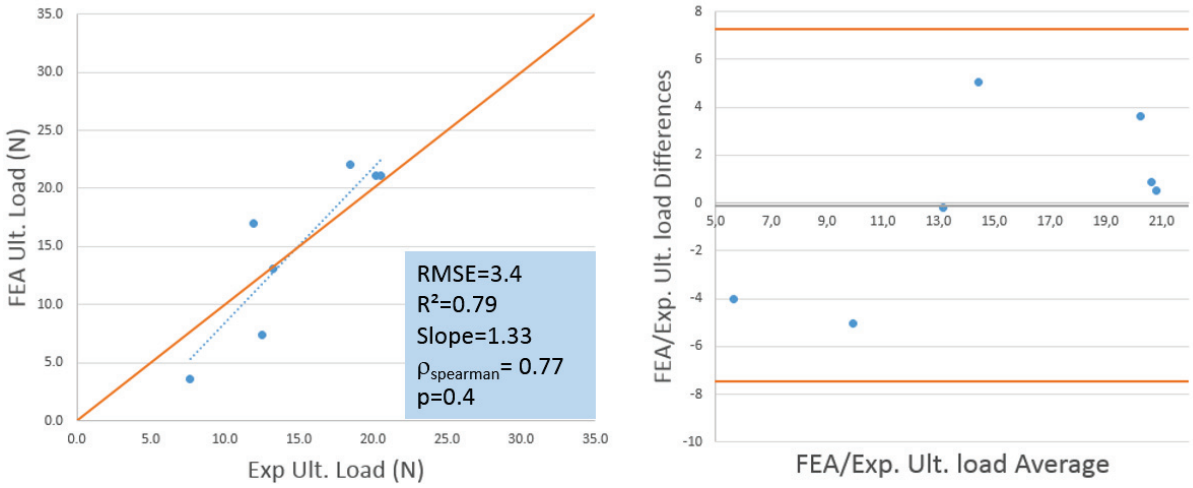

Figure 45: Comparison between Exp. and FEA failure load for specific models of tumor limbs (n=7 limbs)

7. *Specific model (myeloma moduli) results for tumoral bone*

For the same reason as for heterogeneous model mouse 8 was taken off the comparisons between experimental and FEA failure, to be dealt with later (see part 9 of the present chapter).

Young's moduli used for tumor (myeloma) was of 0.3 MPa.

Changing tumor modulus allowed the slightly improvement FEA result as mean difference percentage stayed stable at 24±20%, and R^2 raised to 0.81. The slope offset was slightly higher (1.4) but spearman test showed significance ($\rho_{spearman}$=0.86; p=0.02). Better correlation found with myeloma moduli than mice subcutaneous tumor tissue could be due to the fact that in the last case tumoral tissue developed *in situ*, thus with different material available for its development, that could lead to different material properties.

Table 6: Experimental and simulation (specific) results for each Lytic tumor limbs Removed limb for FEA validation in light grey

	Mice	Experimental Ult. Load (N)	FEA Ult. Load (N)	Difference percentage between exp and FEA (%)
Tumor limbs	Mouse 1, R. limb	20.2	21.1	4.4
	Mouse 2, R. limb	20.6	21.1	2.4
	Mouse 3, R. limb	7.7	3.7	52.2
	Mouse 4, R. limb	13.3	13.1	1.6
	Mouse 5, R. limb	18.4	22.0	19.7
	Mouse 6, R. limb	12.5	7.4	40.5
	Mouse 7, R. limb	11.9	17.0	42.3
	Mouse 8, R. limb	7.7	17.9	133.9

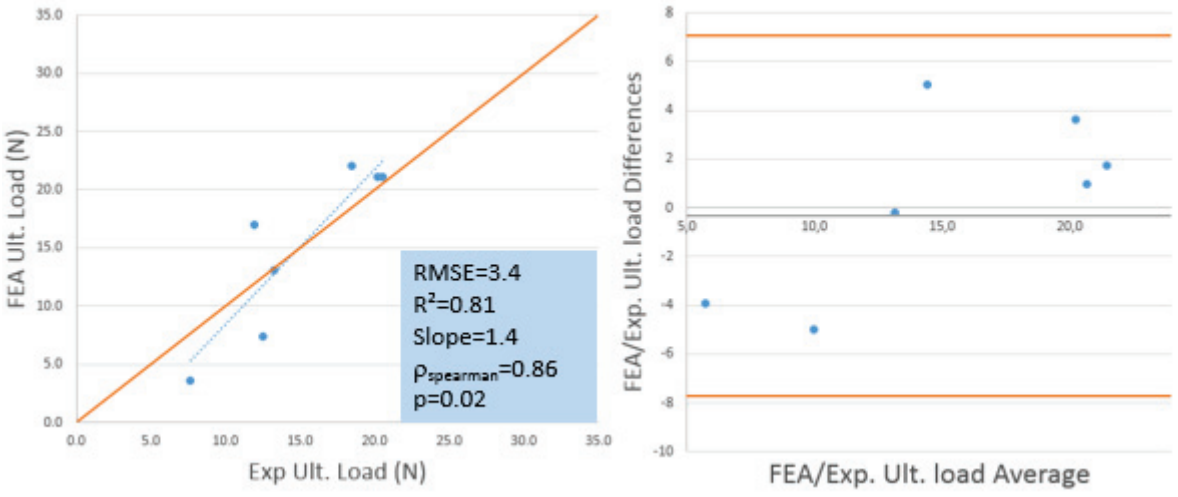

Figure 46: Comparison between Exp. and FEA failure load for specific models of tumor limbs (n=7 limbs)

8. *Comparison between specifics and heterogeneous models for tumoral bone*

As Table 7 shows, heterogeneous model prevailed on all the studied parameters but the Spearman's test was better for the specific model with myeloma module. In addition, manual segmenting of tumor is costly in time and automation is hard to reach. Thus, specific model does not seem to bring any advantage against its simpler version, heterogeneous model.

Table 7: Comparison between the results given by Specific and Heterogeneous model (n=7 limbs)

	Specific model (Myeloma module)	Heterogeneous model	Specific model (B02 module)
RMSE	3.4	3.0	3.4
R^2	0.81	0.85	0.79
Slope	1.40	1.32	1.33
$\rho_{spearman}$	0.86	0.75	0.75
p-value	0.02	0.05	0.05
Mean percentage difference	24±20	12±7	23±22

9. *Failure assessment improvement*

In order to understand why Mouse 8 tumor limb gave a result very different from other tumoral samples a special attention was given to it. Mouse 8 tumoral limb load-displacement curve was compared to the ones of other limbs that had same magnitude lyses (Figure 47).

From this simple comparison raised an idea: what if the failure experienced by Mouse 8 tumor limb was of the same kind of the disruptions experienced by Mouse 4 (around 6N) and Mouse 6 (around 3N) but unless those two samples, the failure provoked a changing in bone structure that prevented it to withstand any more stimulation. Thus, the "ultimate load" of mouse 8 should not be one, but a local failure load preceding whole bone failure as witnessed in mouse 4 and 6.
To test this assumption, a new analysis of tumoral bones simulation was done, but this time only considering the 3mm following the application of the load (Figure 48). Failure was then assessed the exact same way as for whole bone but on this limited element selection.

Mouse 8 local ultimate load got closer from the witnessed experimental ultimate load, while Mouse 4 and 6 local ultimate loads were close to the disruption witnessed in their respective curves (Table 8).

To push the investigation the same local analysis was performed on all bones tested and to compare local and global analyses percentage differences were calculated (negative when local failure < global failure).

Surprisingly, FEA local load of samples presenting reasonable size lyses went over FEA global load despite the bone defect (as for Mouse 1 tumoral limb for instance).

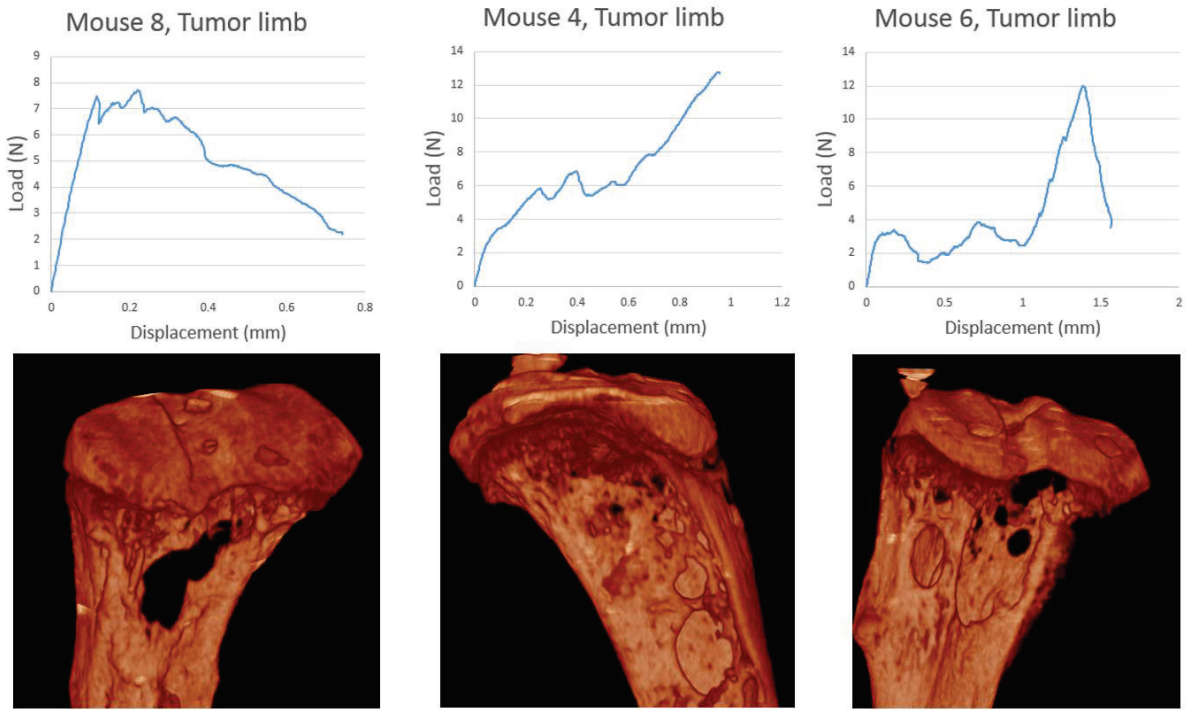

Figure 47: Load-Displacement curves of samples with same lyses magnitude as Mouse 8. Scale adjusted to each curve to clearly see disruption.

More interestingly, all limbs which percentage differences between local and global load went over -20% showed disruptions in their load-displacement curve, while others had a smoother profile (Figure 49).

The only sample that did not follow this trend (Mouse 7) experienced a relatively low failure, as it occurred around 12N while average tumor limb failure with difference percentage superior to -20% is 19.7±1.1 N and sham's average is 22.6±5.2 N, showing a difference with these groups.

These local/global analyses difference could be of great help to detect weakness in tumor bones and thus could help the clinicians in their diagnosis.

Figure 48: a) the load is applied on the element selected on the proximal end of the tibia, as in the previous simulations, b) represents the elements selected in order to obtain the "local failure load" in the bone part where lyses have been observed.

Table 8: Tumor, Sham and Control limbs experimental and FEA results for local and global failure (heterogeneous model)

	Mouse	Experimental Ult. Load (N)	FEA global Ult. Load (N)	FEA local Ult. Load (N)	Difference percentage between FEA global and local Ult. Load
Tumor limbs	Mouse 1, R. limb	20.2	21.0	21.4	2
	Mouse 2, R. limb	20.6	22.4	21.1	-6
	Mouse 3, R. limb	7.7	4.2	2.5	-41
	Mouse 4, R. limb	13.3	10.6	6.2	-42
	Mouse 5, R. limb	18.4	22.7	22.3	-2
	Mouse 6, R. limb	12.5	12.2	6.2	-49
	Mouse 7, R. limb	11.9	16.5	12.3	-26
	Mouse 8, R. limb	7.7	18.3	11.7	-36
Sham limbs	Mouse 1, L. limb	19.4	17.0	21.1	24
	Mouse 2, L. limb	17.8	23.9	25.2	6
	Mouse 3, L. limb	18.2	19.8	19.6	-1
	Mouse 4, L. limb	17.3	20.4	20.3	0
	Mouse 5, L. limb	27.8	27.3	27.4	0
	Mouse 6, L. limb	29.3	24.4	23.7	-3
	Mouse 7, L. limb	28.7	22.6	26.0	15
	Mouse 8, L. limb	22.5	24.0	26.5	11
Control limbs	Mouse 9, R limb	24.1	20.3	19.1	-6
	Mouse 10, R limb	23.4	23.0	22.7	-1
	Mouse 10, L limb	26.6	20.9	20.2	-3
	Mouse 11, R limb	17.8	19.2	17.1	-11
	Mouse 11, L limb	21.4	20.0	18.1	-9
	Mouse 12, R limb	21.9	21.5	18.9	-12
	Mouse 12, L limb	21.5	23.8	26.2	10
	Mouse 13, R limb	20.4	20.2	19.3	-4
	Mouse 13, L limb	25.2	22.7	20.4	-10
	Mouse 14, R limb	20.7	22.8	25.0	10
	Mouse 14, L limb	26.4	21.8	22.1	1
	Mouse 15, R limb	19.4	18.9	19.0	0
	Mouse 15, L limb	23.0	21.1	20.3	-4
	Mouse 16, R limb	24.8	23.7	22.8	-4
	Mouse 16, L limb	27.5	24.0	23.9	0

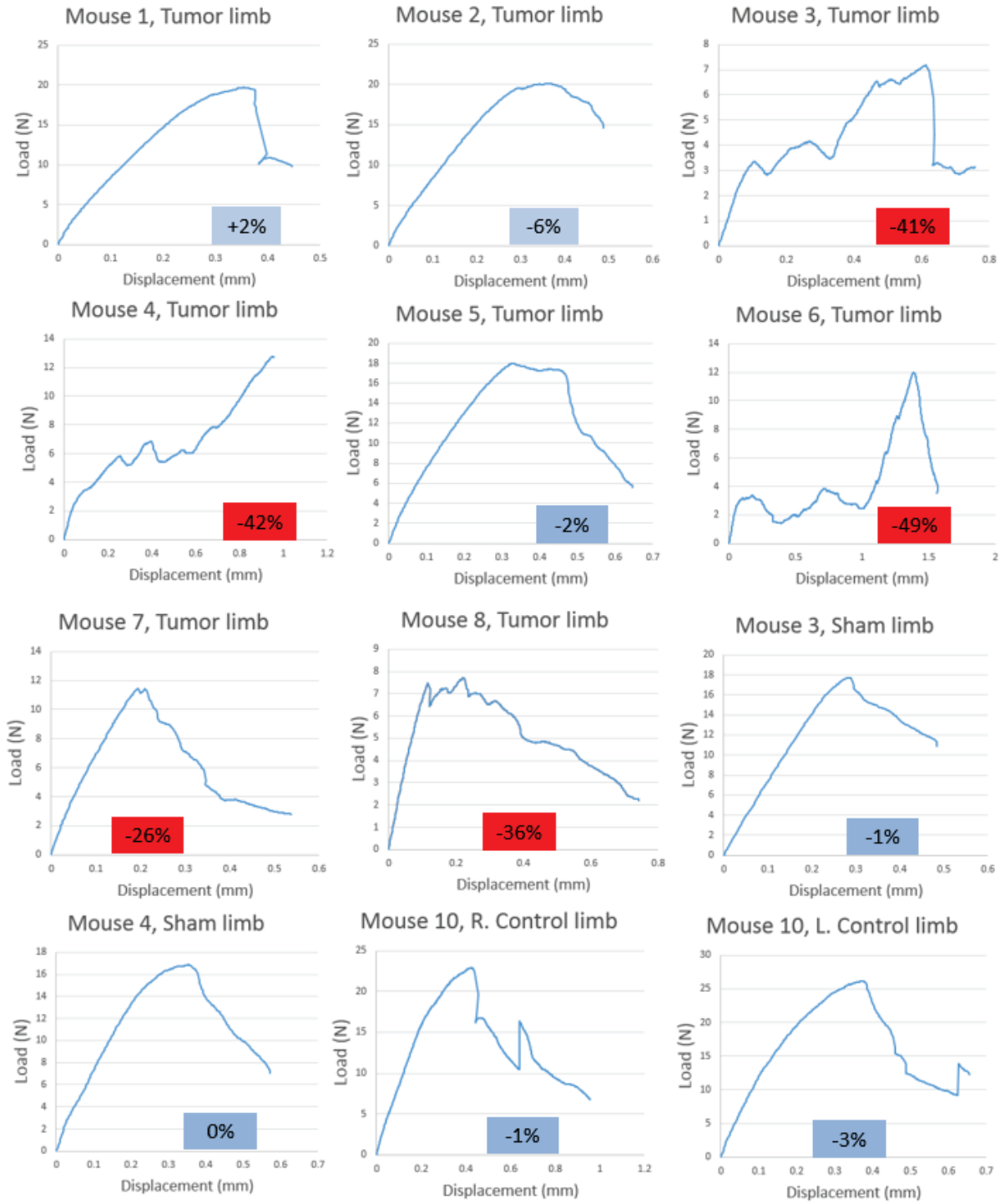

Figure 49: Experimental load-displacement curves for each lytic Tumor limb and examples of sham and control limbs, along with respectif percentage difference between local and global ult. load.

10. Intermediate conclusion

All FEA models ultimate loads showed good agreement with experimental failure loads apart from specific model implemented with Young's moduli obtained on subcutaneous tumors (Table 9, Figure 50). This should be due to the relatively low sample effective, even if the simulations with the moduli obtained on myeloma are improved.

Specific models being more costly in time to obtain, and not showing improvement against its simpler heterogeneous counterpart (see mean percentage differences presented in Table 9), does not seem suitable in our tumor bearing long bones case model (mice tibia).

Table 9: Correlation between experimental and FEA ultimate load for each limbs case presented in this part

	Tumoral limbs Specific model (B02 module)	Tumoral limbs Specific model (Myeloma module)	Tumoral limbs Heterogeneous model	Sham and Control limbs Heterogeneous model	All heterogeneous models
n (limbs)	7	7	7	23	30
RMSE	3.4	3.4	3.0	3.1	3.1
R^2	0.79	0.81	0.85	0.33	0.65
Slope	1.33	1.40	1.32	0.35	0.7
$\rho_{spearman}$	NS	0.86	0.75	0.60	0.71
p-value	0.06	0.02	0.05	0.003	0.00002
Mean percentage difference between exp. and FEA ult. Load	23±22	24±20	12±7	11±8	11±8

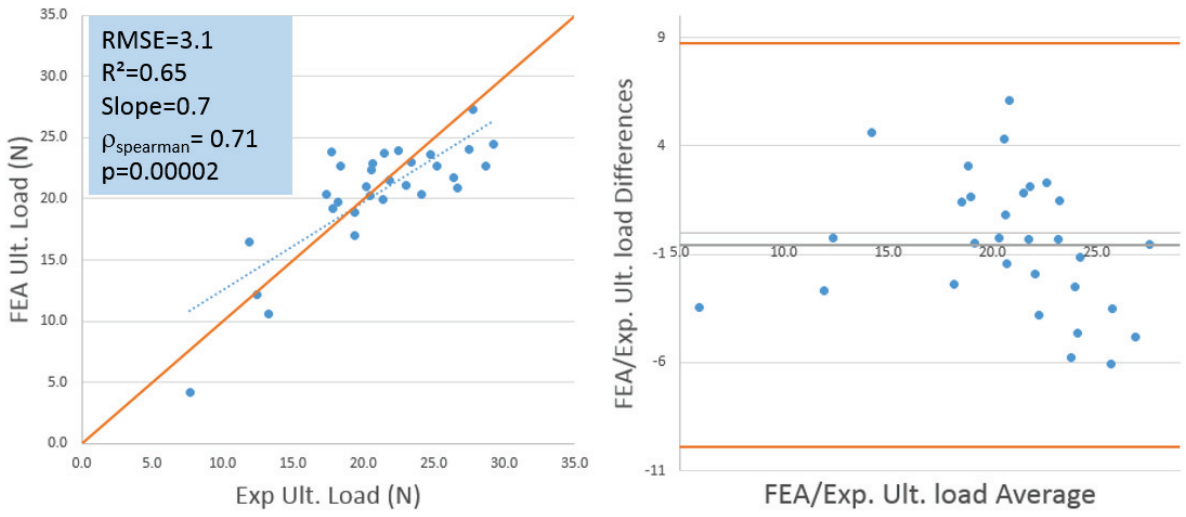

Figure 50: Comparison between Exp. and FEA failure load for heterogeneous models of tumoral, sham and control limbs(n=30 limbs)

Finally, local/global ultimate load comparison allowed the elucidation Mouse 8 FEA/experimental differences from other limbs along with better predicting which limbs could present a fracture lower than the globally detected one.

In fact, a 20% difference between local and global ultimate load in favor of global load allowed the detection of all samples that experience disruption in their load/displacement curves, or knew a low ultimate load.

This finding will have to be confirmed on mixed tumor lesion.

VI. Mixed tumor limbs

1. *Introduction*

To assess the effect of another type of cancer cells, same process as before was led but, this time, CMET (mixed bone defect type coming from human prostate cancer) cells were injected.

The aim of this part is to confirm that the local/global failure load comparison allow the detection of weak limbs as well in mixed lesion as previously presented in lytic lesion.

In the same logic as in precedent part, we wanted to quantify FEA accuracy in each injection case, giving the same analyses for FEA and experimental validation segmentation per injection case.

2. *Material and methods*

Eight BALB/c nude female mice were injected with tumor cells (CMET, human tumor cells) in their right limbs and PBS in their left to create sham limbs. Same nomenclature will be used in this part, only PBS injected mice limbs being referred to as “control” limbs, tumor injected limbs as “tumor” limbs and their contra lateral PBS injected limbs as “sham” limbs. The control group being the same as the one presented in “Lytic tumor limbs” part (Figure 51).

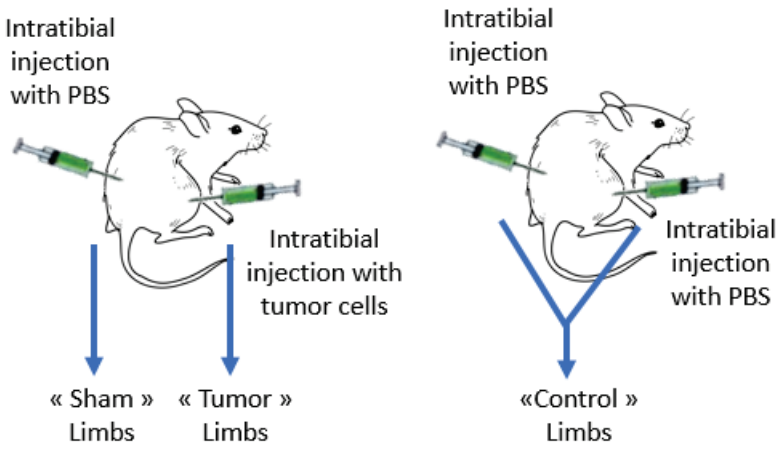

Figure 51: Mice batch denomination depending on injection type

Samples were obtained the exact same way as explained in the previous chapter. To summarize, animals were injected after one week stabling, and thoughtfully monitored for four weeks. After four weeks, they were sacrificed and rear limb were excised *en block* and frozen at -20°C in PBS soaked gaze. Limbs were only unfrozen on the day they were tested and scanned prior and after experimental tests (see methods development chapter for experimental details).

Once limbs tested, numerical models were created using µCT scans acquired before tests. Only one model (heterogeneous) was created for sham limbs, were bone Young’s modulus was linked to hydroxyapatite concentration (Easley *et al.*, 2010). The same model (heterogeneous) was created for

tumor bone not taking into account the tumoral tissue (Keyak *et al.*, 2005). A second model was created for tumoral bone, where tumor was segmented from bone manually, the bone received Young's modulus the same way heterogeneous model did, while tumor was implemented with tumor specific Young's modulus, obtained via rheology (specific model).

These two models (heterogeneous and specific) having a purely elastic behavior law, failure was assessed with a failure criterion modified from Pistoia *et al.* (Pistoia *et al.*, 2002) and supposed to occur when 2% of the meshed bone volume exceeds 0.01 in strain.

3. *Heterogeneous model results for CMET sham*

Failure results for CMET sham are presented in Table 10, along with previously presented control results for comparison.

Table 10: CMET sham limbs and control limbs exp. and FEA results on ultimate load.

	Mice	Experimental Ult. Load (N)	FEA Ult. Load (N)	Difference percentage between exp and FEA (%)
Sham limbs	Mouse 17, L. limb	21.0	21.5	3
	Mouse 18, L. limb	24.2	23.2	4
	Mouse 19, L. limb	14.1	15.7	12
	Mouse 20, L. limb	26.6	20.3	24
	Mouse 21, L. limb	30.1	23.4	22
	Mouse 22, L. limb	17.1	15.7	8
	Mouse 23, L. limb	23.1	21.9	5
	Mouse 24, L. limb	21.0	22.6	8
Control limbs	Mouse 9, R limb	24.1	20.3	16
	Mouse 10, R limb	23.4	23.0	1
	Mouse 10, L limb	26.6	20.9	22
	Mouse 11, R limb	17.8	19.2	8
	Mouse 11, L limb	21.4	20.0	7
	Mouse 12, R limb	21.9	21.5	2
	Mouse 12, L limb	21.5	23.8	11
	Mouse 13, R limb	20.4	20.2	1
	Mouse 13, L limb	25.2	22.7	10
	Mouse 14, R limb	20.7	22.8	10
	Mouse 14, L limb	26.4	21.8	18
	Mouse 15, R limb	19.4	18.9	2
	Mouse 15, L limb	23.0	21.1	8
	Mouse 16, R limb	24.8	23.7	5
	Mouse 16, L limb	27.5	24.0	13

4. *Comparison between CMET sham and control limbs*

The same problem as before logically appeared for the comparison between CMET sham and control limbs as for B02 sham and the control limbs. In fact, strength applied to each sample was not exactly the same due to an uncertainty on the strength on X and Y axes. This uncertainty was raised using FEA models (Figure 37, methods development chapter). The loads on X and Y axes, that were not measured in the test because a one axis (Z) load transducer was used, were identified using the experimental stiffness (see. Heterogeneous model from Methods development chapter).
Unfortunately, neither X and Y loads, neither the norm of the two loads were correlated with control limbs ultimate load (Mann-Whitney test non-significant). On the contrary, the norm of the load on X and Y and sham limbs ultimate load were correlated ($\rho_{spearman}$=0.72, p=0.045). However, the first test being non-significant, no correlated data was available to correct strength differences on ultimate load.

A Mann-Whitney's test was performed and was non-significant (Figure 52). Based on this test, no differences exist, but it relies on few samples, and early stage lyses were witnessed on CMET sham limbs (Figure 54).

Due to this fact, it was assumed that groups could be different and sham results from CMET batch were not pooled with B02 shams and control limbs (Figure 54).

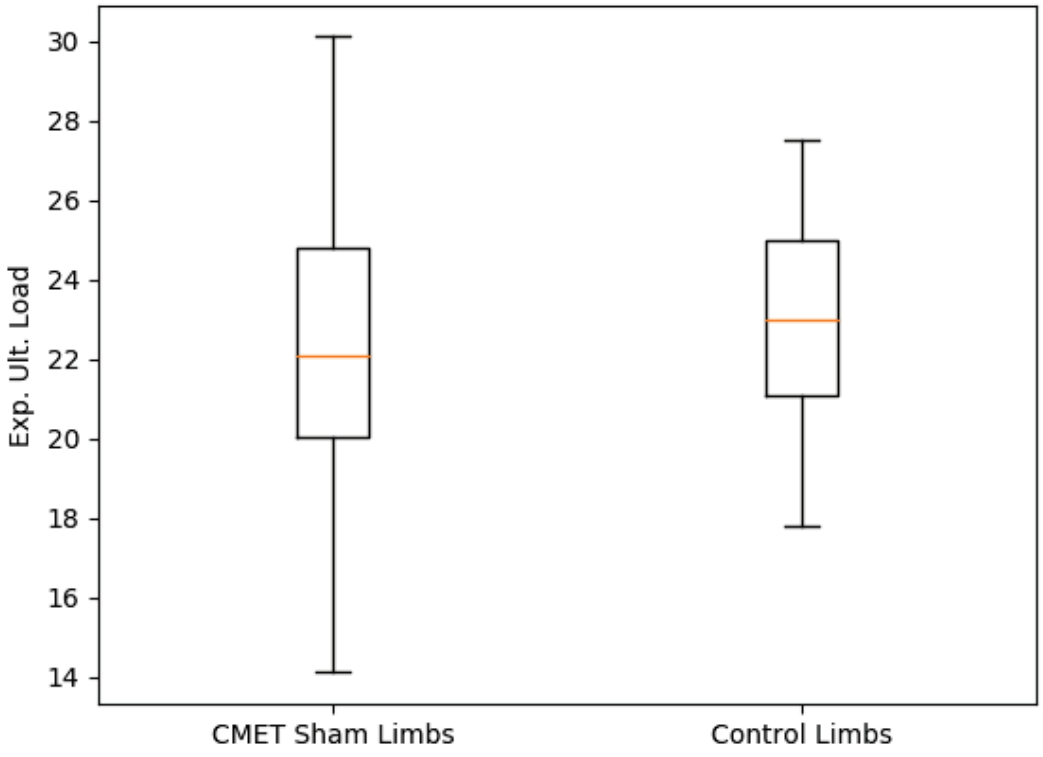

Figure 52: Box plot of sham and control ult. load and Mann-Whitney comparison test results

Therefore, correlation between FEA and experimental ultimate load was performed only on CMET shams (Figure 53).

The different results (R^2=0.62, RMSE=3.5, and $\rho_{spearman}$=0.71 p=0.05) allowed the evaluation of the batch simulation by itself, even if the slope indicated a shift in accuracy.

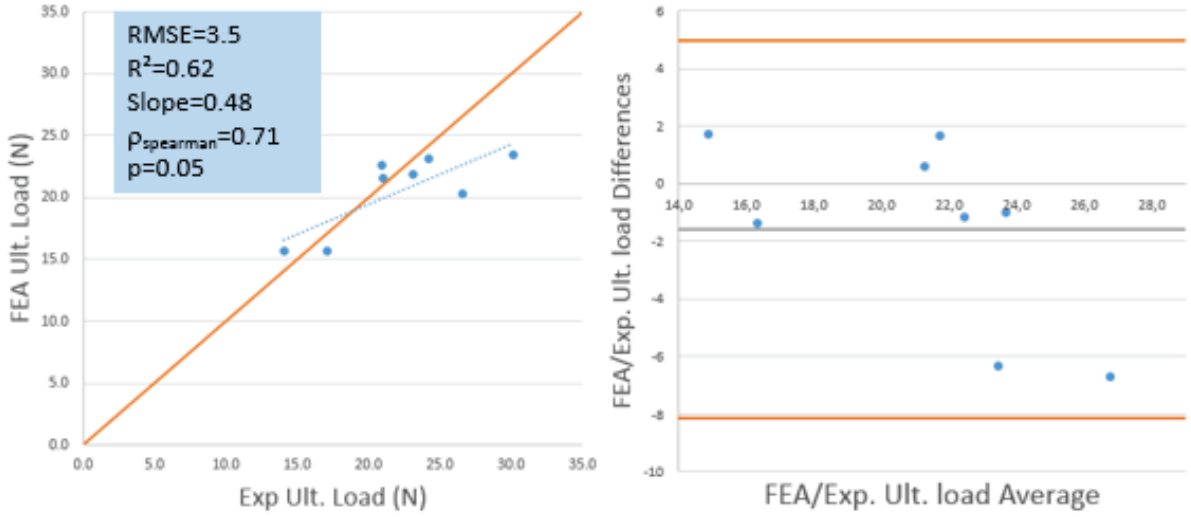

Figure 53: Comparison between Exp. and FEA failure load for heterogeneous models of sham limbs and Bland-Altman representation (n=8 limbs)

Figure 54: Mice 19, 20 and 21 sham limbs showing early stages of tumor lyses.

It has to be noted that the two points at a 6N underestimation on Bland-Altman representation (see Figure 53) belongs respectively to Mouse 20 and 21. These two limbs, despite early lyses stage had a high ultimate load.

We may assume that this may be due to the uncertainty on the loading (on X and Y), that might have provoke loading on the opposite side of where lyses developed, not stimulating the mechanically downgraded side of the bone, but the one that could have fortify to offset this downgrade.

5. *Heterogeneous model results for tumoral bone*

Tumoral limbs failure results for experimental tests and simulation are presented in Table 11.

Heterogeneous model showed good agreement with experiments, with the exception of mouse 19, 20 and 21 that experienced the same kind of early fracture as mouse 8 tumoral limb and was thus taken off the comparison between exp. and FEA comparison.

These cases will be reintegrated and analyzed in part 7 of the present chapter.

Lying on few results, determination coefficient R^2 value was low (0.51), while slope showed a tendency to overestimate low fracture and overestimate high ones. Moreover, Spearman's test was non significant between exp. Ult. Load and FEA's. However, this result being the only non-significant of all performed simulation so far, it was assumed that it was due to low effectives and comparison were still led.

Table 11: Experimental and simulation (heterogeneous) results for each Mixed tumor limbs. Removed limbs for FEA validation in light grey

	Mice	Experimental Ult. Load (N)	FEA Ult. Load (N)	Difference percentage between exp and FEA (%)
Tumor limbs	Mouse 17, R. limb	11.3	14.9	32
	Mouse 18, R. limb	14.7	15.2	3
	Mouse 19, R. limb	4.0	7.9	101
	Mouse 20, R. limb	4.6	7.8	70
	Mouse 21, R. limb	5.8	9.6	65
	Mouse 22, R. limb	14.6	12.1	17
	Mouse 23, R. limb	26.5	21.8	17
	Mouse 24, R. limb	16.8	10.3	39

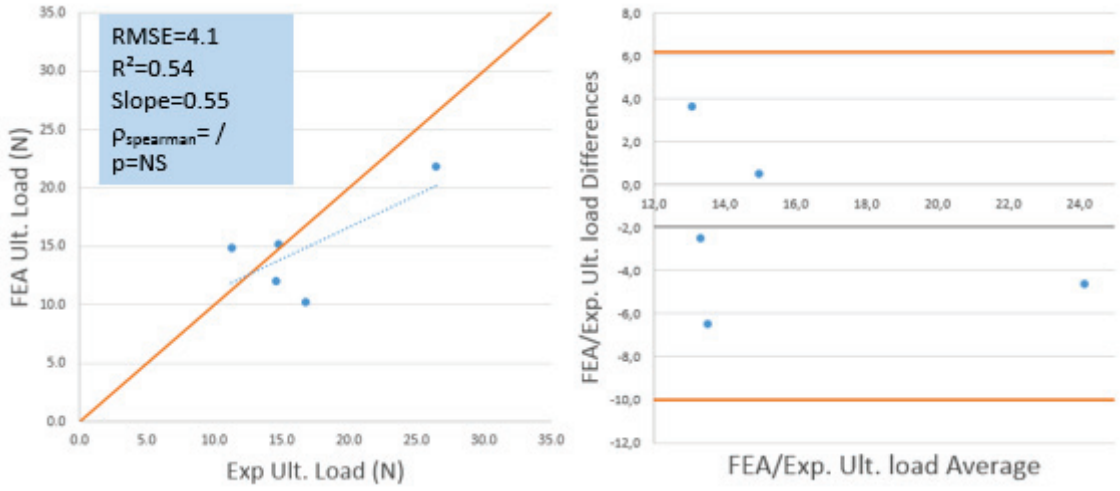

Figure 55: Comparison between Exp. and FEA failure load for heterogeneous models of tumor limbs and Bland-Altman representation (n=5 limbs)

6. *Specific model results for tumoral bone*

Young's modulus used for tumor was of 0.00225 MPa.

Results for CMET tumoral bone specific model are presented in Table 12. Unfortunately, due to extremely large lesion (Figure 56), mathematical solution was not reachable for some models. In fact, contact between tumor and bone prevented to end the simulation in half of the models (4/8).

This lesion size is due to two things. The first is that number of cells to be injected was evaluated on plain radiographs. The second is that mixed lesion type creates bone (see Figure 56 A). These two facts limited the assessment of lyses development as bone formation occurred and masked lyses that would have been visible on 3D scans. This led to an oversizing of the number of cell to be injected as lyses were noticeable only when reaching a high magnitude. When the first 3D scan was performed, reviling real lesion magnitude, it was unfortunately too late to produce new samples.

Moreover, one of the models that did not encountered numerical problem and reached solution happened to be mouse 19 tumor limb (having known an early fracture as mouse 8 tumoral) that was taken off FEA/Exp. comparison, drawing our number of points back to 3.

In these conditions, no statistical test was led and results presented in Table 12 and Figure 57 are only for an informative purpose.

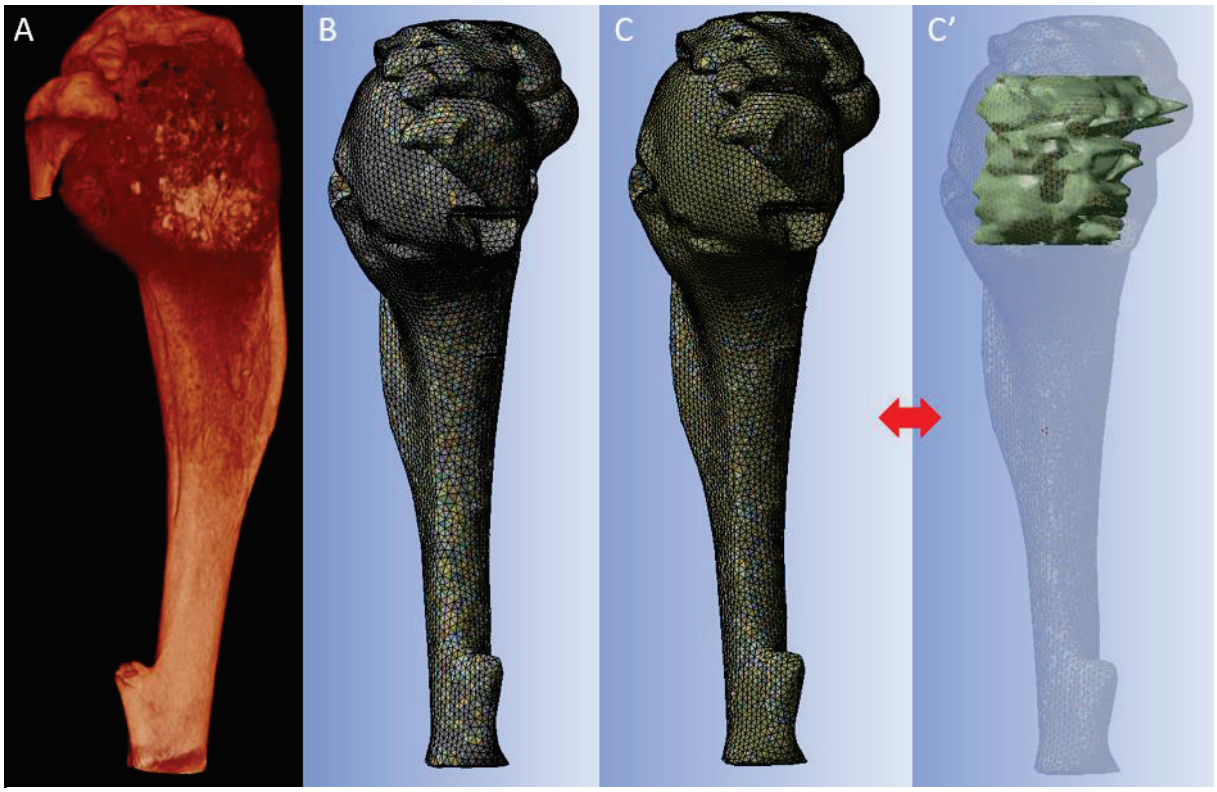

Figure 56: A Mouse 19 tumor limb reconstruction. B Mouse 19 tumor limb heterogeneous model. C Mouse 19 tumor limb specific model. C' Mouse 19 tumor limb specific model with transparent bone element for tumor visualization purpose.

Table 12: Experimental and simulation (specific) results for each Mixed tumoral limbs. Unreachable solution in red.

	Mice	Experimental Ult. Load (N)	FEA Ult. Load (N)	Difference percentage between exp and FEA (%)
Tumor limbs	Mouse 17, R. limb	11.3	4.1	63.7
	Mouse 18, R. limb	14.7	7.8	47.1
	Mouse 19, R. limb	4.0	2.6	34.3
	Mouse 20, R. limb	4.6		
	Mouse 21, R. limb	5.8		
	Mouse 22, R. limb	14.6		
	Mouse 23, R. limb	26.5	21.9	17.1
	Mouse 24, R. limb	16.8		

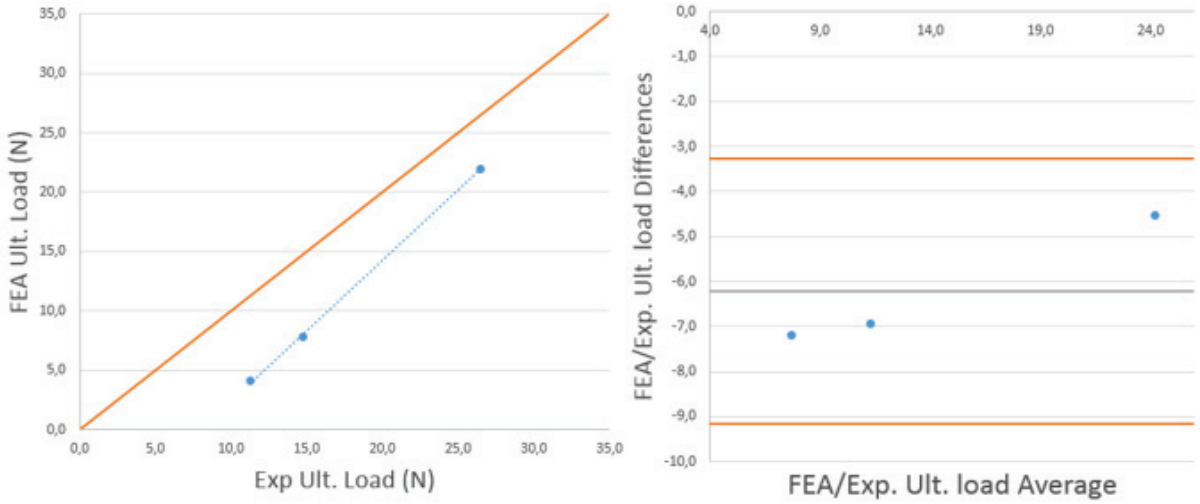

Figure 57: Comparison between Exp. and FEA failure load for specific models of tumor limbs and Bland-Altman representation (n=3 limbs)

7. *Failure assessment improvement*

Willing to see if the global/local analyses gave the same result on mixed lesion as on lytic lesions, the same analyses and comparisons were led on all the limbs from sham and tumoral limbs. Local analyses only recorded strain on the first 3mm following the load application (Figure 58) aiming to detect a local fracture on tumoral zone, while global analyses took the whole limb strain into account in order to detect a global failure load.

All results from those two analyses are presented in Table 13.

Local/global Ult. Load did not allow to segregate weaken limbs as efficiently as for lytic lesion but still allowed to detect most of them Figure 59.

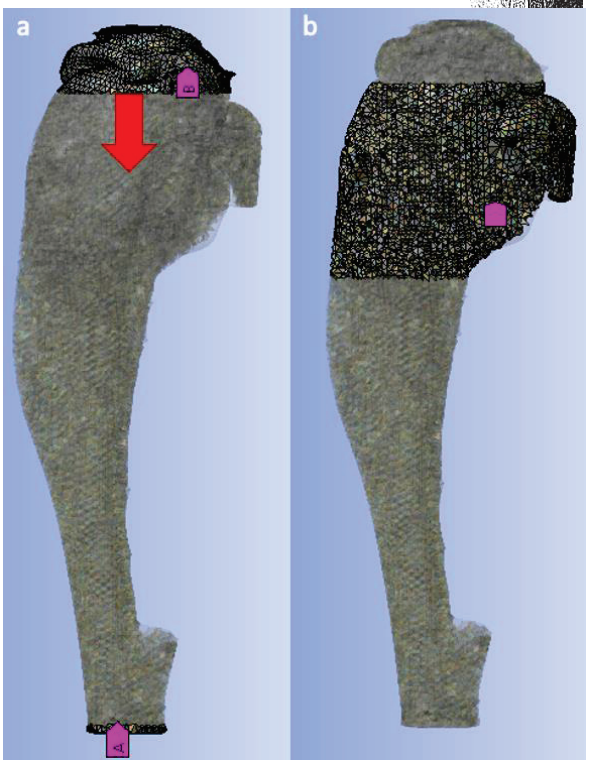

Figure 58: a; Boundary condition. b; elements selected in order to obtain the "local failure load" on bone section with lyses.

Table 13: CMET Tumor and Sham limbs experimental and FEA results for local and global failure

	Mice	Experimental Ult. Load (N)	FEA Ult. Load (N)	FEA local Ult. Load (N)	Difference percentage beetwen local and global FEA failure (%)
Tumor limbs	Mouse 17, R. limb	11.3	14.9	12.9	-13
	Mouse 18, R. limb	14.7	15.2	11.8	-22
	Mouse 19, R. limb	4.0	7.9	5.5	-31
	Mouse 20, R. limb	4.6	7.8	5.4	-30
	Mouse 21, R. limb	5.8	9.6	7.6	-21
	Mouse 22, R. limb	14.6	12.1	7.8	-35
	Mouse 23, R. limb	26.5	21.8	25.1	15
	Mouse 24, R. limb	16.8	10.3	10.2	-1
Sham limbs	Mouse 17, L. limb	21.0	21.5	23.0	7
	Mouse 18, L. limb	24.2	23.2	23.8	3
	Mouse 19, L. limb	14.1	15.7	12.0	-24
	Mouse 20, L. limb	26.6	20.3	19.1	-6
	Mouse 21, L. limb	30.1	23.4	25.0	7
	Mouse 22, L. limb	17.1	15.7	14.3	-9
	Mouse 23, L. limb	23.1	21.9	21.6	-1
	Mouse 24, L. limb	21.0	22.6	21.0	-7

In fact, as it is seeable on Figure 59, Mouse 17 and 21 tumoral limbs global/local Ultimate Load percentage did not reach the -20% threshold (established on B02 tumor limbs), as previously witnessed, even though mouse 17 tumoral limb experienced a low failure and mouse 24 experienced disruption in its load displacement curve.

However, mouse 18, 19,20,21,22 tumoral limbs and mouse 19 sham limb chaotic load/displacement curve or relatively low fracture, were successfully detected (Figure 59).

This emphasis that, even if the local global differences allow the discrimination of most of our weaken limbs, some are not (as mouse 17 and 24 for instance), which underline the need of a complementary criterion to successfully discriminate all weaken limbs.

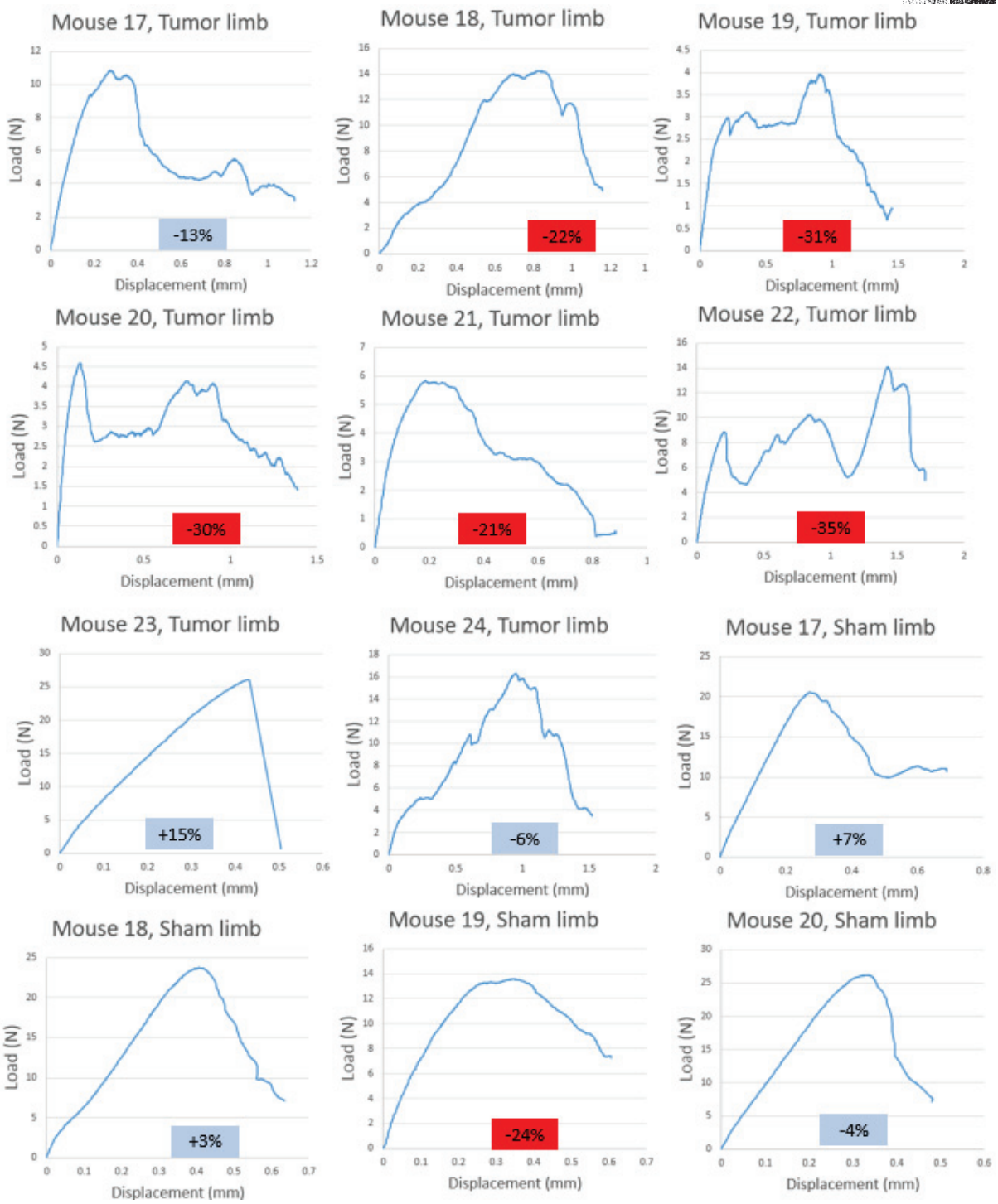

Figure 59: Displacement-Load curves for each mixed Tumoral limb and examples of sham limbs, along with respectif percentage difference between local and global ult. load. Scale was adapted to each curve to clearly see disruptions.

8. *Intermediate conclusion*

Heterogeneous model of sham limb proved to be correlated with experimental results on failure load (average percentage of difference of 22 ± 14% and $\rho_{spearman}$=0.71 p=0.05), which allowed us to validate this FEA results. But, due to large lyses, 3 out of 8 tumoral bones experienced a local failure that prevented to continue sample loading and reach global failure. This forced us to take them out of FEA validation, preventing to see clear correlation between FEA and experimental failure load, surely due to too low number of cases.

Still, as all heterogeneous models so far, lying on more results, showed good agreement between FEA and experimental ultimate load, comparisons were still led. However, pooled results for all heterogeneous models (CMET sham and tumoral limbs plus control limbs) showed good consistency with what was observed on chapter IV, part 10 (Table 14, Figure 60)

Large lyses had an incidence on tumoral bone specific model too, as over extended contacts prevented to reach mathematical solution in half models (4/8). As one of the models that reached solution was one that experienced a local failure preventing to reach the global one, we were left with only three results, too few to perform any comparison.

Table 14: Correlation between experimental and FEA ultimate load for each limbs case presented in this part. (No comparison led on Tumoral limbs specific model due to low effectives).

	Tumoral limbs Specific model (CMET module)	Tumoral limbs Heterogeneous model	Sham limbs Heterogeneous model	All Heterogeneous models
n (limbs)	3	5	8	28
RMSE		4.1	3.5	3.2
R^2		0.54	0.62	0.62
Slope		0.55	0.48	0.62
$\rho_{spearman}$		/	0.71	0.72
p-value		NS	0.05	0.00003
Mean percentage difference between exp. and FEA ult. Load	48±15	22±14	11±8	12±9

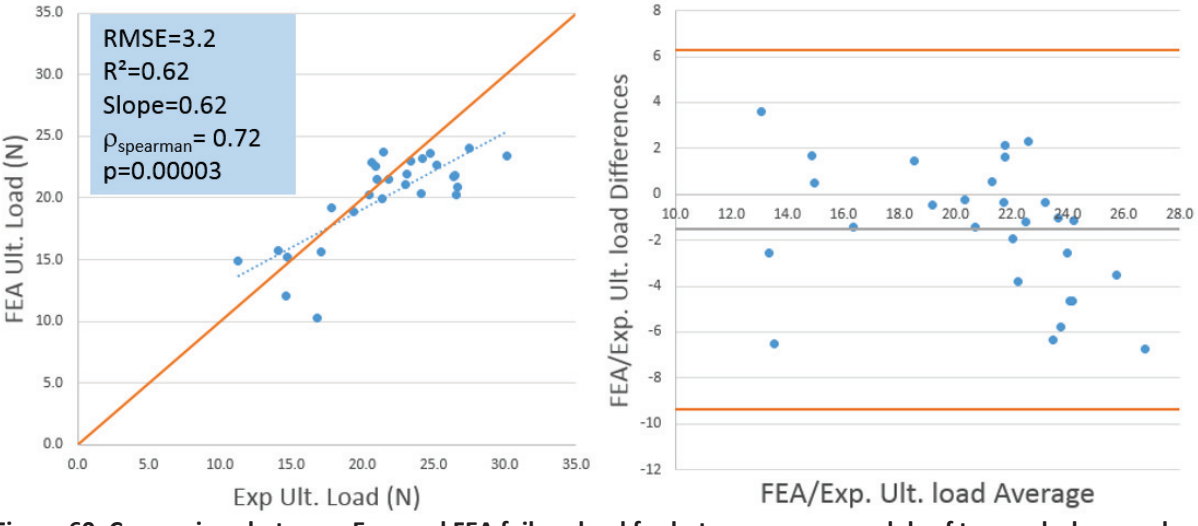

Figure 60: Comparison between Exp. and FEA failure load for heterogeneous models of tumoral, sham and control limbs(n=28 limbs)

The three limbs that were taken out of FEA/Exp. validation were reintegrated in Local/Global analyses in order to see if the differences between the two analyses allowed us to detect them, along with other apparently weaken bones.

Even if the results were not as good as on lytic lesions (2 limbs managed to go through the grid), the percentage difference threshold set at 20% in favor of global failure allowed to detect six out of eight bones that seemed to have altered mechanical strength (either disruption in load/displacement curve or low ultimate load).

Aiming to detect all bone that would present that kind of behavior, analyze was pushed implementing all data available on mice and all limbs tested so far.

VII. Complementary criterion for failure assessment

All results discussed in this part are presented in Table 15.

So far, we tried to detect bone weakness taking into account only local/global failure difference and not failure absolute values. In order to be able to discriminate all bones that would experience either a low fracture or a disruption in their load/displacement curve (physically meaning an early fracture) it was decided to consider mouse weight, which should be linked with global failure load.

To do so, all bones (n=47 limbs) from the present study were considered (lytic tumor bone, mixed tumor bone, both of their shams and control bones). All bones that experienced either a disruption in their load/displacement curve or a failure under the lowest sham/control ultimate load (17.1 N, mouse 22 sham limb) were assessed as weakened, excluding sham limbs that developed visually detectable lyses (*i.e.* Mouse 19, 20 and 21 sham limbs).

Based only on global/local ultimate load differences with a threshold set at -20%, sensibility (defined as real positive divided by the sum of real positives and false negatives) was of 85% and specificity (defined as real negatives divided by the sum of real negatives and false positives) was of 100% (Table 15).

Then, mice weights, which were recorded at the day of the sacrifice, was divided by the FEA global ultimate load in order to take individual morphology differences into account along with bone ultimate load. The threshold to determine which bone is at risk was set at the higher weaken bone ratio between mice weight and global ultimate load (here 0.82 g/N, Table 15).

Unfortunately, even if sensibility increased at 100%, specificity felt to 94%, not really bettering global prediction.

The same operation was performed for weight and FEA local ultimate load and once again, weakness detection threshold was set at the higher weight/local ultimate load ratio of weaken bone (here 0.63 g/N, Table 15).

This allowed to perfectly discriminating weakened bone from safe bone as both sensibility and specificity reached 100%.

Table 15: Bone weakness detection for all studied samples. Bone status were assumed at risk when limbs experienced either a disruption in their load/displacement curve or a failure under the lowest sham/control ultimate load, excluding sham limbs that developed visually detectable lyses (*i.e.* Mouse 19, 20 and 21 sham limbs), giving a threshold at 17.1N

	Mice	Results					Weakness prediction (green: true negative, yellow: false negative, red true positive, orange false positive)		
		Experimental Ult. Load (N)	Bone status (red at risk, green safe)	FEA global Ult. Load (N)	FEA local Ult. Load (N)	Mice Weight (g)	Difference percentage beetwen local and global FEA failure (%)	Weight/FEA global Ultimate Load ratio	Weight/FEA local Ultimate Load ratio
B02 Tumor limbs	Mouse 1, R. limb	20.2		21.0	21.4	21.8	2	0.96	0.98
	Mouse 2, R. limb	20.6		22.4	21.1	21.9	-6	1.02	0.96
	Mouse 3, R. limb	7.7		4.2	2.5	19.1	-41	0.22	0.13
	Mouse 4, R. limb	13.3		10.6	6.2	19.4	-42	0.55	0.32
	Mouse 5, R. limb	18.4		22.7	22.3	25.1	-2	0.90	0.89
	Mouse 6, R. limb	12.5		12.2	6.2	23.2	-49	0.53	0.27
	Mouse 7, R. limb	11.9		16.5	12.3	21.7	-26	0.76	0.56
	Mouse 8, R. limb	7.7		18.3	11.7	23.5	-36	0.78	0.50
Sham limbs	Mouse 1, L. limb	19.4		17.0	21.1	21.8	24	0.78	0.97
	Mouse 2, L. limb	17.8		23.9	25.2	21.9	6	1.09	1.15
	Mouse 3, L. limb	18.2		19.8	19.6	19.1	-1	1.04	1.03
	Mouse 4, L. limb	17.3		20.4	20.3	19.4	0	1.05	1.05
	Mouse 5, L. limb	27.8		27.3	27.4	25.1	0	1.09	1.09
	Mouse 6, L. limb	29.3		24.4	23.7	23.2	-3	1.05	1.02
	Mouse 7, L. limb	28.7		22.6	26.0	21.7	15	1.04	1.20
	Mouse 8, L. limb	22.5		24.0	26.5	23.5	11	1.02	1.13
Control limbs	Mouse 9, R limb	24.1		20.3	19.1	23.0	-6	0.88	0.83
	Mouse 10, R limb	23.4		23.0	22.7	21.7	-1	1.06	1.05
	Mouse 10, L limb	26.6		20.9	20.2	21.7	-3	0.96	0.93
	Mouse 11, R limb	17.8		19.2	17.1	20.3	-11	0.95	0.84
	Mouse 11, L limb	21.4		20.0	18.1	20.3	-9	0.98	0.89
	Mouse 12, R limb	21.9		21.5	18.9	24.0	-12	0.90	0.79
	Mouse 12, L limb	21.5		23.8	26.2	24.0	10	0.99	1.09
	Mouse 13, R limb	20.4		20.2	19.3	25.3	-4	0.80	0.76
	Mouse 13, L limb	25.2		22.7	20.4	25.3	-10	0.90	0.81
	Mouse 14, R limb	20.7		22.8	25.0	22.5	10	1.02	1.11
	Mouse 14, L limb	26.4		21.8	22.1	22.5	1	0.97	0.98
	Mouse 15, R limb	19.4		18.9	19.0	21.3	0	0.89	0.89
	Mouse 15, L limb	23.0		21.1	20.3	21.3	-4	0.99	0.95
	Mouse 16, R limb	24.8		23.7	22.8	24.8	-4	0.95	0.92
	Mouse 16, L limb	27.5		24.0	23.9	24.8	0	0.97	0.96
CMET Tumor limbs	Mouse 17, R. limb	11.3		14.9	12.9	20.8	-13	0.72	0.62
	Mouse 18, R. limb	14.7		15.2	11.8	21.5	-22	0.71	0.55
	Mouse 19, R. limb	4.0		7.9	5.5	19.1	-31	0.42	0.29
	Mouse 20, R. limb	4.6		7.8	5.4	19.3	-30	0.40	0.28
	Mouse 21, R. limb	5.8		9.6	7.6	21.3	-21	0.45	0.36
	Mouse 22, R. limb	14.6		12.1	7.8	17.4	-35	0.69	0.45
	Mouse 23, R. limb	26.5		21.8	25.1	22.9	15	0.95	1.10
	Mouse 24, R. limb	16.8		10.3	10.2	23.3	-1	0.44	0.44
Sham limbs	Mouse 17, L. limb	21.0		21.5	23.0	20.8	7	1.04	1.11
	Mouse 18, L. limb	24.2		23.2	23.8	21.5	3	1.08	1.11
	Mouse 19, L. limb	14.1		15.7	12.0	19.1	-24	0.82	0.63
	Mouse 20, L. limb	26.6		20.3	19.1	19.3	-6	1.05	0.99
	Mouse 21, L. limb	30.1		23.4	25.0	21.3	7	1.10	1.17
	Mouse 22, L. limb	17.1		15.7	14.3	17.4	-9	0.90	0.82
	Mouse 23, L. limb	23.1		21.9	21.6	22.9	-1	0.96	0.94
	Mouse 24, L. limb	21.0		22.6	21.0	23.3	-7	0.97	0.90

VIII. Global conclusion, perspectives and discussion

Our failure prediction results proved to be in the same range as published work (Figure 61). Moreover, same parameters as Nyman *et al.* (Nyman *et al.*, 2015) were identified when optimizing Pistoia's criterion (fractural volume of 2% exceeding a failure strain of 0.01). Thus the current results are consistent with this previous study developed in the same condition (an animal model study using a failure criterion developed on human bones on mice bones).

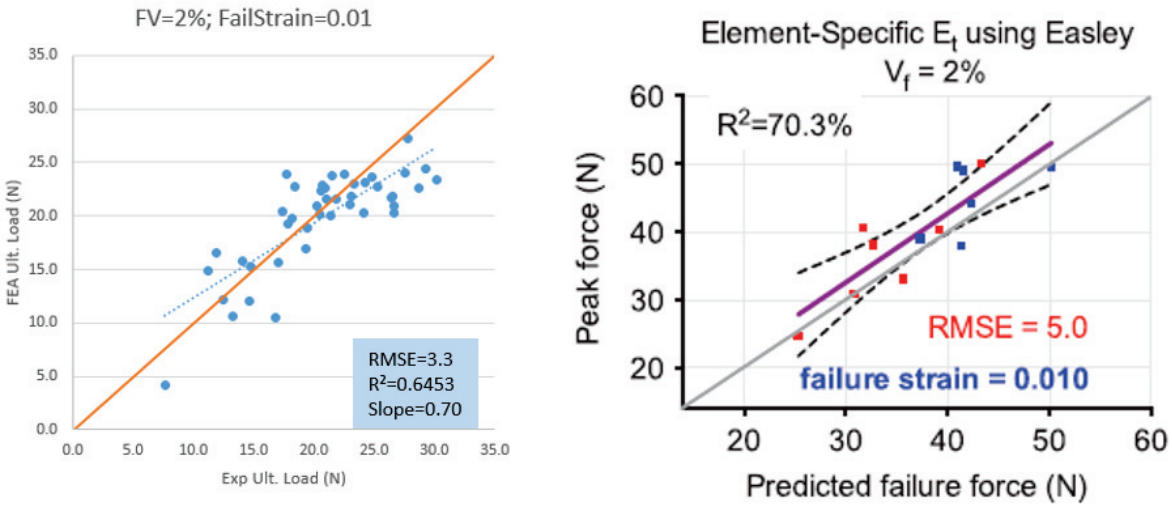

Figure 61: Comparison between results obtained in this study (n=43 limbs, on the top left) and Nyman *et al.* 2015 published results on mice vertebrae (on the top right)

Results obtained on specific model (with a specific property for the tumor) did not allow to better predict failure. In fact, heterogeneous model were more consistent with experimental value (average difference of 12±9% for heterogeneous models (n=43 limbs) against 30±21% for specific model (n=11 limbs, myeloma module for B02 tumoral limbs and CMET module for CMET tumor limbs).

This original result shows that specific model does not bring improvement while being harder to build. Indeed specific model needs tumor segmentation which is currently manual. Automation would need machine-learning algorithms. On the other hand, automatically obtaining heterogeneous model would be easier, some parts as sane bone segmentation being already automated. The comparison between both modelling approaches should be applied to larger tumors to confirm the current results.

Of course, there is room for improvement for our specific model. In fact, our results suggest that to be exploitable, tumor properties should be quantified on tumor developed in bone only. Moreover, the model could be more realistic, creating a transition zone between tumor and bone instead of making non realistic brutal frontier between the two materials. However, our heterogeneous results as well as published studies using equivalent models (Eggermont et al., 2018; Goodheart et al., 2015) show that for metastases bone failure prediction, specific tumor properties do not seem to be needed.

Our results are in agreement with literature results using heterogeneous models that accurately detect bone failure on animal models (*ex vivo* study) and retrospective patient cases (Derikx *et al.*, 2012; Eggermont *et al.*, 2018; Goodheart *et al.*, 2015; Mann *et al.*, 2008).
Based on the current and previous results, heterogeneous model is efficient enough and specific model is not needed, even if our specific model suffered several limitations.
The main limitations are due to the fact that mixed tumor (CMET) Young's modulus was quantified only on subcutaneous tumor. B02 Young's modulus proved to give less accurate results than patient myeloma tested. Moreover tumor segmentation was manual with the assumption that tumor developed where cortical was pierced. Models were purely linear elastic, not taking into account tumor viscosity and plasticity.

Finally, we were able to improve failure assessment of tumoral bone, comparing a global bone analysis with a local one (performed on the 3 mm of bone were tumors developed, due to our intratibial injection animal model).
A threshold of 20% difference between local and global ultimate loads allowed to successfully differentiating all B02 tumoral samples which would have a different behavior than control and sham groups.
This behavior was considered different first when a disruption in their load-displacement curve occurred, physically meaning a partial bone failure. Second, when an ultimate load was inferior to the lowest witnessed in sham and control groups, excluding Mouse 19, 20 and 21 that developed lyses due to large tumoral development in their contra-lateral limbs. This behavior will be furtherly referred to as "weaken bones".
This segregation was not as efficient when considering CMET tumoral bones as two weaken bones were not identified.
Considering mouse weight in the criterion (dividing mice weight by FEA global ultimate load and setting higher ratio obtained for weaken bone as a threshold) allowed to successfully detect all weaken bones but unfortunately detected control bones as weaken (false positives).
Finally, using mice weight and local failure load (dividing mice weight by local ultimate load and setting highest weaken bone ratio as threshold) allowed to successfully detect all weaken bones and did not induce false positives.

This improved prediction may be useful in human bones to help clinician in their decision.

Of course before that, a long way remains. One of the first step would be to confirm this result in a retrospective study on patients with metastatic bone follow up, as it was done in recently published work (Eggermont *et al.*, 2018).
Another step would be to automate the FEA process (from the image up to the results of the simulation) to make it usable in daily clinical practice.

In the near future, the present study could be improved pushing µCT images analyses in parallel with histology staining. In fact, more precise analyses could help understanding parameters that could explain weaken bone behavior based on data as lyses volume, cortical lyses involvement, or possible transition zone (if identifiable).

Additionally, to be closer to Pistoia's idea when developing his criterion, results could be reworked in order to consider the correlation between first inflections in load-displacement curve with load predicted with the criterion.

Ultimately, this study presents several limitations as being based on an animal model when clinical need is on patients. Moreover, the FE models are isotropic, purely linear elastic when bone is in fact a highly anisotropic, elastoplastic material. Lastly, the performed tests and the simulation were in quasi-static loading, roughly mimicking a single leg stance when in real life loadings could be dynamic and failures can occur during stairs climbing or chair standing and not only walking.

Nevertheless, published studies presented the same limitations ((Mann *et al.*, 2008) working on a mice cancer model, and (Derikx *et al.*, 2012) in a cadaveric model with mechanically induced metastases bone (compared to biologically induced tumors in the current work), both in quasi static bone loading mimicking single leg stance for experimental tests and static for simulation). Yet, the retrospectives studies performed on patients showed promising results (Eggermont *et al.*, 2018; Goodheart *et al.*, 2015).
The results obtained so far allow concluding this work with an optimistic note on the possible application in clinical practice. A multicentric study in France has just started (principal investigator Professor Cyrille Confavreux, rheumatologist).

IX. Personal publications

- Publications in a peer-review journals

Failure prediction of metastatic bone with osteolytic lesion in mice.
B. Delpuech, S. Nicolle, C. Confavreux, L. Bouazza, P. Clezardin, H. Follet, and D. Mitton,
Consecutive to an ICoNSoM 2019 talk, under preparation.

- Oral communication in international conferences with proceedings publications

Effect of intra-tibial injection on mechanical properties of mousebone,
B. Delpuech, C. Confavreux, L. Bouazza, S. Geraci, P. Clezardin, D.Mitton & H. Follet (2017), Computer Methods in Biomechanics and Biomedical Engineering, 20:sup1, 57-58, DOI:10.1080/10255842.2017.1382859« Oral presentation in international conferences ».

- Oral presentation in international conferences

Determination of tumor tissue mechanical properties, toward quantification of implication of tumor in whole bone resistance: a preliminary study,
B. Delpuech, S. Nicolle, C. Confavreux, L. Bouazza, S. Geraci, P. Clezardin, D. Mitton, and H. Follet,
ESBiomech Conference 2019, Vienna, Austria.

- Poster presentation in international conferences

Failure prediction of metastatic bone with osteolytic lesion in mice,
B. Delpuech, S. Nicolle, C. Confavreux, L. Bouazza, P. Clezardin, D. Mitton, and H. Follet,
8Th World Congress of Biomechanics 2018, Dublin, Ireland,

-Price:

ESB travel award winner.

X. Bibliography

Anatomy and Physiology | Simple Book Production [WWW Document], n.d. URL https://courses.lumenlearning.com/nemcc-ap/ (accessed 7.19.18).

Arguello, F., Baggs, R.B., Frantz, C.N., 1988. A Murine Model of Experimental Metastasis to Bone and Bone Marrow. Cancer Res. 48, 6876–6881.

Ascenzi, M.-G., Lutz, A., Du, X., Klimecky, L., Kawas, N., Hourany, T., Jahng, J., Chin, J., Tintut, Y., Nackenhors, U., Keyak, J., 2014. Hyperlipidemia affects multiscale structure and strength of murine femur. J. Biomech. 47, 2436–2443. https://doi.org/10.1016/j.jbiomech.2014.04.006

Attar, S., Steffner, R.J., Avedian, R., Hussain, W.M., 2012. Surgical intervention of nonvertebral osseous metastasis. Cancer Control J. Moffitt Cancer Cent. 19, 113–121. https://doi.org/10.1177/107327481201900205

Benca, E., Reisinger, A., Patsch, J.M., Hirtler, L., Synek, A., Stenicka, S., Windhager, R., Mayr, W., Pahr, D.H., 2017. Effect of simulated metastatic lesions on the biomechanical behavior of the proximal femur. J. Orthop. Res. 35, 2407–2414. https://doi.org/10.1002/jor.23550

Benca, E., Synek, A., Amini, M., Kainberger, F., Hirtler, L., Windhager, R., Mayr, W., Pahr, D.H., 2019. QCT-based finite element prediction of pathologic fractures in proximal femora with metastatic lesions. Sci. Rep. 9. https://doi.org/10.1038/s41598-019-46739-y

Bessho, M., Ohnishi, I., Matsumoto, T., Ohashi, S., Matsuyama, J., Tobita, K., Kaneko, M., Nakamura, K., 2009. Prediction of proximal femur strength using a CT-based nonlinear finite element method: Differences in predicted fracture load and site with changing load and boundary conditions. Bone 45, 226–231. https://doi.org/10.1016/j.bone.2009.04.241

Bone Remodeling [WWW Document], n.d. URL https://courses.washington.edu/conj/bess/bone/bone2.html (accessed 7.24.18).

Boundless Anatomy and Physiology | Simple Book Publishing [WWW Document], n.d. URL https://courses.lumenlearning.com/boundless-ap/ (accessed 6.5.19).

Boyd, S.K., Szabo, E., Ammann, P., 2011. Increased bone strength is associated with improved bone microarchitecture in intact female rats treated with strontium ranelate: A finite element analysis study. Bone 48, 1109–1116. https://doi.org/10.1016/j.bone.2011.01.004

Burkhart, T.A., Andrews, D.M., Dunning, C.E., 2013. Finite element modeling mesh quality, energy balance and validation methods: A review with recommendations associated with the modeling of bone tissue. J. Biomech. 46, 1477–1488. https://doi.org/10.1016/j.jbiomech.2013.03.022

Cazzato, R.L., Garnon, J., Koch, G., Shaygi, B., Tsoumakidou, G., Caudrelier, J., Boatta, E., Buy, X., Palussiere, J., Gangi, A., 2018. Current role of interventional radiology in the management of visceral and bone metastases from thyroid cancer. Gland Surg. 7, 80–88. https://doi.org/10.21037/gs.2017.12.08

Cheal, E.J., Hipp, J.A., Hayes, W.C., 1993. Evaluation of finite element analysis for prediction of the strength reduction due to metastatic lesions in the femoral neck. J. Biomech. 26, 251–264. https://doi.org/10.1016/0021-9290(93)90363-J

Chevalier, Y., Pahr, D., Allmer, H., Charlebois, M., Zysset, P., 2007. Validation of a voxel-based FE method for prediction of the uniaxial apparent modulus of human trabecular bone using macroscopic mechanical tests and nanoindentation. J. Biomech. 40, 3333–3340. https://doi.org/10.1016/j.jbiomech.2007.05.004

Coleman, R.E., 1997. Skeletal complications of malignancy. Cancer 80, 1588–1594.

De Souza, R.L., Matsuura, M., Eckstein, F., Rawlinson, S.C.F., Lanyon, L.E., Pitsillides, A.A., 2005. Non-invasive axial loading of mouse tibiae increases cortical bone formation and modifies trabecular organization: A new model to study cortical and cancellous compartments in a single loaded element. Bone 37, 810–818. https://doi.org/10.1016/j.bone.2005.07.022

Delpuech, B., Confavreux, C., Bouazza, L., Geraci, S., Clezardin, P., Mitton, D., Follet, H., 2017. Effect of intra-tibial injection on mechanical properties of mouse bone. Comput. Methods Biomech. Biomed. Engin. 20, 57–58. https://doi.org/10.1080/10255842.2017.1382859

Derikx, L.C., van Aken, J.B., Janssen, D., Snyers, A., van der Linden, Y.M., Verdonschot, N., Tanck, E., 2012. The assessment of the risk of fracture in femora with metastatic lesions. J. Bone Joint Surg. Br. 94-B, 1135–1142. https://doi.org/10.1302/0301-620X.94B8.28449

Derikx, L.C., Verdonschot, N., Tanck, E., 2015. Towards clinical application of biomechanical tools for the prediction of fracture risk in metastatic bone disease. J. Biomech. 48, 761–766. https://doi.org/10.1016/j.jbiomech.2014.12.017

Du, Z., Zang, J., Tang, X., Guo, W., 2010. Experts' agreement on therapy for bone metastases. Orthop. Surg. 2, 241–253. https://doi.org/10.1111/j.1757-7861.2010.00095.x

Duchemin, L., Mitton, D., Jolivet, E., Bousson, V., Laredo, J.D., Skalli, W., 2008. An anatomical subject-specific FE-model for hip fracture load prediction. Comput. Methods Biomech. Biomed. Engin. 11, 105–111. https://doi.org/10.1080/10255840802297143

Easley, S.K., Jekir, M.G., Burghardt, A.J., Li, M., Keaveny, T.M., 2010. Contribution of the intra-specimen variations in tissue mineralization to PTH- and raloxifene-induced changes in stiffness of rat vertebrae. Bone 46, 1162–1169. https://doi.org/10.1016/j.bone.2009.12.009

Edwards, J.R., Nyman, J.S., Lwin, S.T., Moore, M.M., Esparza, J., O'Quinn, E.C., Hart, A.J., Biswas, S., Patil, C.A., Lonning, S., Mahadevan-Jansen, A., Mundy, G.R., 2010. Inhibition of TGF-β signaling by 1D11 antibody treatment increases bone mass and quality in vivo. J. Bone Miner. Res. 25, 2419–2426. https://doi.org/10.1002/jbmr.139

Eggermont, F., Derikx, L.C., Verdonschot, N., van der Geest, I.C.M., de Jong, M. a. A., Snyers, A., van der Linden, Y.M., Tanck, E., 2018. Can patient-specific finite element models better predict fractures in metastatic bone disease than experienced clinicians? Bone Jt. Res. 7, 430–439. https://doi.org/10.1302/2046-3758.76.BJR-2017-0325.R2

El-Hamalawi, A., 2000. A simple and effective element distortion factor. https://doi.org/10.1016/S0045-7949(99)00105-4

Erdemir, A., Guess, T.M., Halloran, J., Tadepalli, S.C., Morrison, T.M., 2012. Considerations for Reporting Finite Element Analysis Studies in Biomechanics. J. Biomech. 45, 625–633. https://doi.org/10.1016/j.jbiomech.2011.11.038

Fathers, K.E., Bell, E.S., Rajadurai, C.V., Cory, S., Zhao, H., Mourskaia, A., Zuo, D., Madore, J., Monast, A., Mes-Masson, A.-M., Grosset, A.-A., Gaboury, L., Hallet, M., Siegel, P., Park, M., 2012. Crk adaptor proteins act as key signaling integrators for breast tumorigenesis. Breast Cancer Res. BCR 14, R74. https://doi.org/10.1186/bcr3183

Fellipa, C., 2012. FEM modeling : Mesh, Loads and BCs, Chapter7. [WWW Document]. URL http://kis.tu.kielce.pl//mo/COLORADO_FEM/colorado/IFEM.Ch07.index.html (accessed 4.15.19).

Fidler, M., 1973. Prophylactic Internal Fixation of Secondary Neoplastic Deposits in Long Bones. Br. Med. J. 1, 341–343.

Fritton, J.C., Myers, E.R., Wright, T.M., van der Meulen, M.C.H., 2005a. Loading induces site-specific increases in mineral content assessed by microcomputed tomography of the mouse tibia. Bone 36, 1030–1038. https://doi.org/10.1016/j.bone.2005.02.013

Fritton, J.C., Myers, E.R., Wright, T.M., van der Meulen, M.C.H., 2005b. Loading induces site-specific increases in mineral content assessed by microcomputed tomography of the mouse tibia. Bone 36, 1030–1038. https://doi.org/10.1016/j.bone.2005.02.013

Fung, Y.C., 1993. Biomechanics: Mechanical Properties of Living Tissues, 2nd ed. Springer-Verlag, New York.

Gardner, M.J., Meulen, M.C.H. van der, Demetrakopoulos, D., Wright, T.M., Myers, E.R., Bostrom, M.P., 2006. In Vivo Cyclic Axial Compression Affects Bone Healing in the Mouse Tibia. J. Orthop. Res. Off. Publ. Orthop. Res. Soc. 24, 1679–1686. https://doi.org/10.1002/jor.20230

Geis, C., Graulich, M., Wissmann, A., Hagenacker, T., Thomale, J., Sommer, C., Schäfers, M., 2010. Evoked pain behavior and spinal glia activation is dependent on tumor necrosis factor receptor 1 and 2 in a mouse model of bone cancer pain. Neuroscience 169, 463–474. https://doi.org/10.1016/j.neuroscience.2010.04.022

Goodheart, J.R., Cleary, R.J., Damron, T.A., Mann, K.A., 2015. Simulating activities of daily living with finite element analysis improves fracture prediction for patients with metastatic femoral lesions. J. Orthop. Res. 33, 1226–1234. https://doi.org/10.1002/jor.22887

Harrington, K.D., 1982. New trends in the management of lower extremity metastases. Clin. Orthop. 53–61.

Higinbotham, N.L., Marcove, R.C., 1965. THE MANAGEMENT OF PATHOLOGICAL FRACTURES. J. Trauma Acute Care Surg. 5, 792.

Holguin, N., Brodt, M.D., Sanchez, M.E., Kotiya, A.A., Silva, M.J., 2013. Adaptation of Tibial Structure and Strength to Axial Compression Depends on Loading-History in Both C57BL/6 and BALB/C Mice. Calcif. Tissue Int. 93, 211–221. https://doi.org/10.1007/s00223-013-9744-4

Hong, J., Cabe, G.D., Tedrow, J.R., Hipp, J.A., Snyder, B.D., 2004. Failure of trabecular bone with simulated lytic defects can be predicted non-invasively by structural analysis. J. Orthop. Res. 22, 479–486. https://doi.org/10.1016/j.orthres.2003.09.006

Hoskin, P.J., 2003. Bisphosphonates and radiation therapy for palliation of metastatic bone disease. Cancer Treat. Rev. 29, 321–327. https://doi.org/10.1016/S0305-7372(03)00013-6

Iannaccone, P.M., Jacob, H.J., 2009. Rats! Dis. Model. Mech. 2, 206–210. https://doi.org/10.1242/dmm.002733

Jepsen, K.J., Silva, M.J., Vashishth, D., Guo, X.E., van der Meulen, M.C., 2015. Establishing Biomechanical Mechanisms in Mouse Models: Practical Guidelines for Systematically Evaluating Phenotypic Changes in the Diaphyses of Long Bones. J. Bone Miner. Res. Off. J. Am. Soc. Bone Miner. Res. 30, 951–966. https://doi.org/10.1002/jbmr.2539

Katagiri, H., Takahashi, M., Wakai, K., Sugiura, H., Kataoka, T., Nakanishi, K., 2005. Prognostic factors and a scoring system for patients with skeletal metastasis. J. Bone Joint Surg. Br. 87-B, 698–703. https://doi.org/10.1302/0301-620X.87B5.15185

Keyak, J.H., Kaneko, T.S., Rossi, S.A., Pejcic, M.R., Tehranzadeh, J., Skinner, H.B., 2005. Predicting the strength of femoral shafts with and without metastatic lesions. Clin. Orthop. 439, 161–170.

Keyak, J.H., Kaneko, T.S., Skinner, H.B., Hoang, B.H., 2007. The effect of simulated metastatic lytic lesions on proximal femoral strength. Clin. Orthop. 459, 139–145. https://doi.org/10.1097/BLO.0b013e3180514caa

Keyak, J.H., Lee, I.Y., Nath, D.S., Skinner, H.B., 1996. Postfailure compressive behavior of tibial trabecular bone in three anatomic directions. J. Biomed. Mater. Res. 31, 373–378. https://doi.org/10.1002/(SICI)1097-4636(199607)31:3<373::AID-JBM11>3.0.CO;2-K

Keyak, J.H., Rossi, S.A., Jones, K.A., Les, C.M., Skinner, H.B., 2001. Prediction of fracture location in the proximal femur using finite element models. Med. Eng. Phys. 23, 657–664.

Keyak, J.H., Sigurdsson, S., Karlsdottir, G.S., Oskarsdottir, D., Sigmarsdottir, A., Kornak, J., Harris, T.B., Sigurdsson, G., Jonsson, B.Y., Siggeirsdottir, K., Eiriksdottir, G., Gudnason, V., Lang, T.F., 2013. Effect of finite element model loading condition on fracture risk assessment in men and women: The AGES-Reykjavik study. Bone 57, 18–29. https://doi.org/10.1016/j.bone.2013.07.028

Klingner, B.M., Shewchuk, J.R., 2008. Aggressive Tetrahedral Mesh Improvement, in: Brewer, M.L., Marcum, D. (Eds.), Proceedings of the 16th International Meshing Roundtable. Springer Berlin Heidelberg, pp. 3–23.

Knupp, P., 2001. Algebraic Mesh Quality Metrics. SIAM J. Sci. Comput. 23, 193–218. https://doi.org/10.1137/S1064827500371499

Kopperdahl, D.L., Aspelund, T., Hoffmann, P.F., Sigurdsson, S., Siggeirsdottir, K., Harris, T.B., Gudnason, V., Keaveny, T.M., 2014. Assessment of incident spine and hip fractures in women and men using finite element analysis of CT scans. J. Bone Miner. Res. 29, 570–580. https://doi.org/10.1002/jbmr.2069

Leong, N.L., Anderson, M.E., Gebhardt, M.C., Snyder, B.D., 2010. Computed Tomography-Based Structural Analysis for Predicting Fracture Risk in Children with Benign Skeletal Neoplasms. J. Bone Joint Surg. Am. 92, 1827–1833. https://doi.org/10.2106/JBJS.I.00871

Logan, D.L., 2012. A first course in the finite element method, 5th ed. ed. Cengage Learning, Stamford, CT.

Lund, M.E., de Zee, M., Andersen, M.S., Rasmussen, J., 2012. On validation of multibody musculoskeletal models. Proc. Inst. Mech. Eng. [H] 226, 82–94. https://doi.org/10.1177/0954411911431516

Lynch, M.E., Brooks, D., Mohanan, S., Lee, M.J., Polamraju, P., Dent, K., Bonassar, L.J., van der Meulen, M.C.H., Fischbach, C., 2013. In Vivo Tibial Compression Decreases Osteolysis and Tumor Formation in a Human Metastatic Breast Cancer Model. J. Bone Miner. Res. Off. J. Am. Soc. Bone Miner. Res. 28, 2357–2367. https://doi.org/10.1002/jbmr.1966

Lynch, M.E., Main, R.P., Xu, Q., Walsh, D.J., Schaffler, M.B., Wright, T.M., van der Meulen, M.C.H., 2010. Cancellous bone adaptation to tibial compression is not sex dependent in growing mice. J. Appl. Physiol. 109, 685–691. https://doi.org/10.1152/japplphysiol.00210.2010

Mann, K.A., Lee, J., Arrington, S.A., Damron, T.A., Allen, M.J., 2008. Predicting Distal Femur Bone Strength in a Murine Model of Tumor Osteolysis. Clin. Orthop. 466, 1271–1278. https://doi.org/10.1007/s11999-008-0241-4

Mantyh, P., 2013. Bone cancer pain: causes, consequences, and therapeutic opportunities. Pain 154 Suppl 1, S54-62. https://doi.org/10.1016/j.pain.2013.07.044

Mirels, H., 2003. The Classic: Metastatic Disease in Long Bones A Proposed Scoring System for Diagnosing Impending Pathologic Fractures. Clin. Orthop. 415. https://doi.org/10.1097/01.blo.0000093045.56370.dd

Mundy, G.R., 2002. Metastasis: Metastasis to bone: causes, consequences and therapeutic opportunities. Nat. Rev. Cancer 2, 584–593. https://doi.org/10.1038/nrc867

National Academies of Sciences, E., 2011. Procedures for Verification and Validation of Computer Simulations Used for Roadside Safety Applications. https://doi.org/10.17226/17647

Niebur, G.L., Feldstein, M.J., Yuen, J.C., Chen, T.J., Keaveny, T.M., 2000. High-resolution finite element models with tissue strength asymmetry accurately predict failure of trabecular bone. J. Biomech. 33, 1575–1583. https://doi.org/10.1016/S0021-9290(00)00149-4

Nyman, J.S., Uppuganti, S., Makowski, A.J., Rowland, B.J., Merkel, A.R., Sterling, J.A., Bredbenner, T.L., Perrien, D.S., 2015. Predicting mouse vertebra strength with micro-computed tomography-derived finite element analysis. BoneKEy Rep. 4. https://doi.org/10.1038/bonekey.2015.31

Ottewell, P.D., Wang, N., Brown, H.K., Fowles, C.A., Croucher, P.I., Eaton, C.L., Holen, I., 2015. OPG-Fc inhibits ovariectomy-induced growth of disseminated breast cancer cells in bone. Int. J. Cancer 137, 968–977. https://doi.org/10.1002/ijc.29439

Ottewell, P.D., Wang, N., Brown, H.K., Reeves, K.J., Fowles, C.A., Croucher, P.I., Eaton, C.L., Holen, I., 2014. Zoledronic Acid Has Differential Antitumor Activity in the Pre- and Postmenopausal Bone Microenvironment In Vivo. Clin. Cancer Res. 20, 2922–2932. https://doi.org/10.1158/1078-0432.CCR-13-1246

Ottewell, P.D., Woodward, J.K., Lefley, D.V., Evans, C.A., Coleman, R.E., Holen, I., 2009. Anticancer mechanisms of doxorubicin and zoledronic acid in breast cancer tumor growth in bone. Mol. Cancer Ther. 8, 2821–2832. https://doi.org/10.1158/1535-7163.MCT-09-0462

Patel, T.K., Brodt, M.D., Silva, M.J., 2014. Experimental and finite element analysis of strains induced by axial tibial compression in young-adult and old female C57Bl/6 mice. J. Biomech. 47, 451–457. https://doi.org/10.1016/j.jbiomech.2013.10.052

Pereira, A.F., Javaheri, B., Pitsillides, A.A., Shefelbine, S.J., 2015. Predicting cortical bone adaptation to axial loading in the mouse tibia. J. R. Soc. Interface 12. https://doi.org/10.1098/rsif.2015.0590

Pistoia, W., van Rietbergen, B., Lochmüller, E.-M., Lill, C.A., Eckstein, F., Rüegsegger, P., 2002. Estimation of distal radius failure load with micro-finite element analysis models based on three-dimensional peripheral quantitative computed tomography images. Bone 30, 842–848. https://doi.org/10.1016/S8756-3282(02)00736-6

Prasad, J., Wiater, B.P., Nork, S.E., Bain, S.D., Gross, T.S., 2010. Characterizing gait induced normal strains in a murine tibia cortical bone defect model. J. Biomech. 43, 2765–2770. https://doi.org/10.1016/j.jbiomech.2010.06.030

Quenneville, C.E., Dunning, C.E., 2011. Development of a finite element model of the tibia for short-duration high-force axial impact loading. Comput. Methods Biomech. Biomed. Engin. 14, 205–212. https://doi.org/10.1080/10255842.2010.548324

Razi, H., Birkhold, A.I., Zaslansky, P., Weinkamer, R., Duda, G.N., Willie, B.M., Checa, S., 2015. Skeletal maturity leads to a reduction in the strain magnitudes induced within the bone: A murine tibia study. Acta Biomater. 13, 301–310. https://doi.org/10.1016/j.actbio.2014.11.021

Renders, G.A.P., Mulder, L., Langenbach, G.E.J., van Ruijven, L.J., van Eijden, T.M.G.J., 2008. Biomechanical effect of mineral heterogeneity in trabecular bone. J. Biomech. 41, 2793–2798. https://doi.org/10.1016/j.jbiomech.2008.07.009

Robling, A.G., Burr, D.B., Turner, C.H., 2001. Skeletal loading in animals. J. Musculoskelet. Neuronal Interact. 1, 249–262.

Rogge, R.D., Adams, B.D., Goel, V.K., 2002. An analysis of bone stresses and fixation stability using a finite element model of simulated distal radius fractures. J. Hand Surg. 27, 86–92. https://doi.org/10.1053/jhsu.2002.29485

Scheid, V., Buzdar, A.U., Smith, T.L., Hortobagyi, G.N., 1986. Clinical course of breast cancer patients with osseous metastasis treated with combination chemotherapy. Cancer 58, 2589–2593. https://doi.org/10.1002/1097-0142(19861215)58:12<2589::AID-CNCR2820581206>3.0.CO;2-O

Slosky, L.M., Largent-Milnes, T.M., Vanderah, T.W., 2015a. Use of Animal Models in Understanding Cancer-induced Bone Pain. Cancer Growth Metastasis 8, 47–62. https://doi.org/10.4137/CGM.S21215

Slosky, L.M., Largent-Milnes, T.M., Vanderah, T.W., 2015b. Use of Animal Models in Understanding Cancer-induced Bone Pain. Cancer Growth Metastasis 8, 47–62. https://doi.org/10.4137/CGM.S21215

Spatz, J.M., Ellman, R., Cloutier, A.M., Louis, L., van Vliet, M., Suva, L.J., Dwyer, D., Stolina, M., Ke, H.Z., Bouxsein, M.L., 2013. Sclerostin Antibody Inhibits Skeletal Deterioration Due to Reduced Mechanical Loading. J. Bone Miner. Res. Off. J. Am. Soc. Bone Miner. Res. 28, 865–874. https://doi.org/10.1002/jbmr.1807

Tanck, E., van Aken, J.B., van der Linden, Y.M., Schreuder, H.W.B., Binkowski, M., Huizenga, H., Verdonschot, N., 2009. Pathological fracture prediction in patients with metastatic lesions can be improved with quantitative computed tomography based computer models. Bone 45, 777–783. https://doi.org/10.1016/j.bone.2009.06.009

Turner, C.H., Burr, D.B., 1993. Basic biomechanical measurements of bone: A tutorial. Bone 14, 595–608. https://doi.org/10.1016/8756-3282(93)90081-K

Urwin, G.H., Percival, R.C., Harris, S., Beneton, M.N., Williams, J.L., Kanis, J.A., 1985. Generalised increase in bone resorption in carcinoma of the prostate. Br. J. Urol. 57, 721–723.

Van der Linden, Y.M., Dijkstra, P.D.S., Kroon, H.M., Lok, J.J., Noordijk, E.M., Leer, J.W.H., Marijnen, C. a. M., 2004. Comparative analysis of risk factors for pathological fracture with femoral metastases. J. Bone Joint Surg. Br. 86, 566–573.

van Rietbergen, B., Ito, K., 2015. A survey of micro-finite element analysis for clinical assessment of bone strength: The first decade. J. Biomech., In Memory of Rik Huiskes 48, 832–841. https://doi.org/10.1016/j.jbiomech.2014.12.024

Verhulp, E., van Rietbergen, B., Huiskes, R., 2006. Comparison of micro-level and continuum-level voxel models of the proximal femur. J. Biomech. 39, 2951–2957. https://doi.org/10.1016/j.jbiomech.2005.10.027

Viceconti, M., Taddei, F., Van Sint Jan, S., Leardini, A., Cristofolini, L., Stea, S., Baruffaldi, F., Baleani, M., 2008. Multiscale modelling of the skeleton for the prediction of the risk of fracture. Clin. Biomech. Bristol Avon 23, 845–852. https://doi.org/10.1016/j.clinbiomech.2008.01.009

Wagner, D.W., Lindsey, D.P., Beaupre, G.S., 2011. Deriving tissue density and elastic modulus from microCT bone scans. Bone 49, 931–938. https://doi.org/10.1016/j.bone.2011.07.021

Wedin, R., Bauer, H.C.F., 2005. Surgical treatment of skeletal metastatic lesions of the proximal femur. J. Bone Joint Surg. Br. 87-B, 1653–1657. https://doi.org/10.1302/0301-620X.87B12.16629

Werbeck, J.L., Thudi, N.K., Martin, C.K., Premanandan, C., Yu, L., Ostrowksi, M.C., Rosol, T.J., 2014. Tumor Microenvironment Regulates Metastasis and Metastasis Genes of Mouse MMTV-PymT Mammary Cancer Cells In Vivo. Vet. Pathol. 51, 868–881. https://doi.org/10.1177/0300985813505116

Wernle, J.D., Damron, T.A., Allen, M.J., Mann, K.A., 2010. Local irradiation alters bone morphology and increases bone fragility in a mouse model. J. Biomech. 43, 2738–2746. https://doi.org/10.1016/j.jbiomech.2010.06.017

Wong, M., Pavlakis, N., 2011. Optimal management of bone metastases in breast cancer patients. Breast Cancer Targets Ther. 3, 35–60. https://doi.org/10.2147/BCTT.S6655

Wright, L.E., Ottewell, P.D., Rucci, N., Peyruchaud, O., Pagnotti, G.M., Chiechi, A., Buijs, J.T., Sterling, J.A., 2016. Murine models of breast cancer bone metastasis. Bonekey Rep. 5, UNSP 804. https://doi.org/10.1038/bonekey.2016.31

Yang, H., Butz, K.D., Duffy, D., Niebur, G.L., Nauman, E.A., Main, R.P., 2014. Characterization of cancellous and cortical bone strain in the in vivo mouse tibial loading model using microCT-based finite element analysis. Bone 66, 131–139. https://doi.org/10.1016/j.bone.2014.05.019

Yang, X., Matsuda, K., Bialek, P., Jacquot, S., Masuoka, H.C., Schinke, T., Li, L., Brancorsini, S., Sassone-Corsi, P., Townes, T.M., Hanauer, A., Karsenty, G., 2004. ATF4 Is a Substrate of RSK2 and an Essential Regulator of Osteoblast Biology: Implication for Coffin-Lowry Syndrome. Cell 117, 387–398. https://doi.org/10.1016/S0092-8674(04)00344-7

Yoneda, T., Sasaki, A., Mundy, G.R., 1994. Osteolytic bone metastasis in breast cancer. Breast Cancer Res. Treat. 32, 73–84.

Zapata, E., Rongieras, F., Pialat, J.-B., Follet, H., Mitton, D., 2017. An ex vivo experiment to reproduce a forward fall leading to fractured and non-fractured radii. J. Biomech. 63, 174–178. https://doi.org/10.1016/j.jbiomech.2017.08.013

Zysset, P., Qin, L., Lang, T., Khosla, S., Leslie, W.D., Shepherd, J.A., Schousboe, J.T., Engelke, K., 2015. Clinical Use of Quantitative Computed Tomography-Based Finite Element Analysis of the Hip and Spine in the Management of Osteoporosis in Adults: the 2015 ISCD Official Positions-Part

II. J. Clin. Densitom. Off. J. Int. Soc. Clin. Densitom. 18, 359–392. https://doi.org/10.1016/j.jocd.2015.06.011

Zysset, P.K., Dall'Ara, E., Varga, P., Pahr, D.H., 2013. Finite element analysis for prediction of bone strength. BoneKEy Rep. 2. https://doi.org/10.1038/bonekey.2013.120

XI. French Summarize

1. *Table des matières*

2. *Introduction*

Le corps humain (adulte) est composé de 206 os (“Anatomy and Physiology | Simple Book Production,” n.d.) qui sont des tissus denses et composent la majeure partie du squelette humain.

Le rôle de l’os est multiple. Tout d’abord, au niveau cellulaire, il produit les cellules du sang (de par la moelle osseuse) et permet le stockage ainsi que l’utilisation de minéraux et de gras. Ensuite, au niveau de l’organisme, il permet de supporter le reste du corps, tout en lui apportant une protection. Enfin, il facilite le mouvement en procurant des points d’insertions aux muscles (via les tendons).

L’os n’est pas un matériau figé, mais un matériau vivant, qui se réadapte tout au long de la vie en fonction des sollicitations extérieures qu’il reçoit(“Bone Remodeling,” n.d.).

Le cancer pour sa part, décrit un ensemble de maladies qui ont en commun le dérèglement de la croissance cellulaire causée par des mutations génétiques.
En tant que tel, ses origines sont avant tout génétiques, bien que le risque de développer un cancer soit aggravé par des facteurs environnementaux (le fait de fumer, l’obésité, la pollution environnante…).
Il inclut un sous-ensemble malin de néoplasmes : un groupe de cellules qui croit de façon non régulée et forme une masse de tissus : les tumeurs.
Une de ses principales caractéristiques est sa possibilité de migrer à d’autres parties du corps que son site de développement primaire et de s’y implanter via les métastases (tumeurs migrantes).

Le squelette, étant hautement vascularisé, est l’endroit le plus communément affecté par le cancer métastatique (Coleman, 1997).
Le développement des métastases osseuses n’est pas un évènement chaotique, mais une succession d’étapes organisées depuis la survie des métastases dans le sang jusqu’à l’implantation et le développement dans les tissus osseux en passant par le transfert du sang à l’os (Wong and Pavlakis, 2011).
Le plus souvent, les métastases osseuses se développent dans la moelle osseuse. Elles sont par ailleurs dénommées en fonction de leur apparence radiographique, telle que lytique (aspect d’un trou à la radio), condensantes (densification osseuse) ou mixte (mélange des deux précédentes,(Wong and Pavlakis, 2011).

L’apparition de ces métastases osseuses fragilise l’os et peut provoquer des fractures pathologiques. Toutefois la prédiction de telles fractures est difficile et loin d’être automatique.

En effet, dans une étude incluant 1800 patients, une faible occurrence de fracture a été rapportée (8%) et 53% de ces dernières avaient eu lieu chez des patients atteints du cancer du sein (Higinbotham and Marcove, 1965).
Une autre étude, ne considérant que des patients atteint de cancer du sein, a rapporté une incidence de fracture pathologiques de 57% (Scheid et al., 1986).

Enfin, dans une étude comprenant 37 cas de cancer de la prostate avec lésions condensantes, tous les patients ont présenté une fracture pathologique (Wedin and Bauer, 2005).
Ceci montre que, quel que soit le type de métastase et le site primaire de développement du cancer, tous les types de lésions métastatiques sont problématiques.

Les indications pour pratiquer une chirurgie permettant d'éviter ce type de fracture varie en fonction des patients et des chirurgiens (Attar et al., 2012). Quoiqu'il en soit, le fait que la décision de mener une chirurgie préventive dépende de plusieurs aspects tels que la localisation de la tumeur, l'espérance de vie du patient, les attentes de ce dernier ainsi que les risques pour l'intégrité de l'os a fait un large consensus (Attar et al., 2012).

Toutefois les risques pour la stabilité de l'os avec métastases est difficile à quantifier, même par des chirurgiens experts (Attar et al., 2012).
En 1982, Mirels a proposé une méthode de score pour prédire le risque de fracture des os longs (os de forme cylindrique, plus long que large, tel que le fémur le tibia ou l'humérus) atteints de métastases (Mirels, 2003). Ce score a été développé sur 78 os longs atteints de métastases osseuses et repose sur la notation de quatre critères: la taille de la lésion, son site d'implantation dans l'os, le degré de sclérose/ lyse osseuse constaté et la douleur ressentie par le patient (Mirels, 2003). Avec le temps, le score de Mirels est devenu largement utilisé (Van der Linden et al., 2004).

De manière à tester ce score sur une plus large gamme de patients que celle sur laquelle il avait été développé, Van der Linden a mené une étude rétrospective sur 102 patients. Ces derniers présentaient tous des métastases osseuses et quatorze d'entre eux avaient connu une fracture pathologique pendant le suivi.
Tous les cas répertoriés ont été évalués à l'aide du score de Mirels. Il en ressort que si la décision avait été prise sur la base de ce simple score, 84 cas (82% du total des cas considérés) auraient été sur-traités chirurgicalement, et 13% auraient été déclarés n'étant pas à risque et auraient fracturé (Van der Linden et al., 2004). En ajoutant un seuil sur l'implication corticale de la métastase, il a été possible de réduire le sur-traitement chirurgical supposé à 42% (Van der Linden et al., 2004).

Etant donné que le sur-traitement chirurgical a un large impact sur la qualité de vie de patients disposant d'une espérance de vie faible, un outil de diagnostic plus discriminant serait souhaitable.

Une possibilité pour créer un tel outil serait les simulations numériques par éléments finis (FEA en anglais pour « Finite Elements Analysis ») spécifiques aux patients. Le potentiel de cette méthode a largement été étudié et a montré de très bons résultats dans le cas de l'ostéoporose (parmi d'autres : Bessho et al. 2009; Duchemin et al. 2008; Keyak et al. 2013).
Etant donné que cette méthode a montré un potentiel inégalé par les autres modalités, elle a été plus récemment étudiée comme outil pouvant potentiellement améliorer la prédiction des fractures (ou des risques de fractures) d'os métastatiques (Derikx et al., 2012; Eggermont et al., 2018; Goodheart et al., 2015; Keyak et al., 2005).
Ces études ont finalement montré que la FEA spécifique au patient était capable de surpasser l'expertise des cliniciens dans le cas d'étude *ex vivo* avec défauts osseux induits mécaniquement

(Derikx et al., 2012), la FEA atteignant un taux de Kendall de 0.78 contre 0.5 ±0.03 en moyenne pour six cliniciens experts.
Toutefois cette étude ayant été menée *ex vivo*, sur des défauts osseux induits mécaniquement (donc sans tissus métastatiques), il était alors impossible de statuer sur la reproductibilité de tels résultats dans le cas clinique.
Cette impossibilité a été levée au cours des dernières années, lorsqu'une étude a été menée par la même équipe sur une cohorte de patients atteints de métastases osseuses .trente-neuf patients ont été inclus à l'étude et suivis, soit pendant six mois si possible, soit jusqu'à ce que l'os atteint de métastases fracture, soit jusqu'à leur décès (en fonction du premier des trois événements à survenir, Eggermont et al. 2018a).
Les résultats obtenus ont été en accord avec ceux de la précédente étude, la prédiction de la FEA atteignant 89% de sensitivité (prédiction correcte des cas de fractures) contre 0 à 33% pour les cliniciens.
Bien que sans commune mesure, les résultats se sont montrés moins probants sur la spécificité (prédiction correcte des cas de non fracture). Ainsi les cliniciens ont pu atteindre un pourcentage de spécificité allant de 84 à 95%, la FEA n'atteignant pour sa part que 79%.

Les recherches portant sur le cancer osseux sont toutefois difficiles à mettre en place, les échantillons osseux étant rares.
De manière à contourner la difficulté de trouver des échantillons humains rarement disponibles, ou d'étudier des paramètres non étudiables de façon non-invasive chez l'homme, la souris a été utilisée comme modèle squelettique dans plusieurs cas. Ainsi, ce modèle animal a pu être utilisé dans le cadre de recherche sur le remodelage osseux (Fritton et al., 2005b), les études précliniques (Slosky et al., 2015b) ou encore la tenue mécanique d'os atteint de métastases *exvivo* (Mann et al., 2008).

Ainsi, de manière à pouvoir étudier l'implication du tissu métastatique dans la résistance globale de l'os sur échantillons réels, nous avons utilisé ce modèle animal pour créer des échantillons tumoraux.

Notre but était double : premièrement, quantifier l'apport de la prise en compte des propriétés mécaniques de la métastase dans la résistance globale de l'os. Deuxièmement, statuer sur le fait qu'un modèle plus simple que celui proposé dans la littérature (reposant sur des propriétés purement élastiques plutôt qu'élasto-plastiques (Eggermont et al., 2018)) pouvait permettre d'améliorer la prédiction de fractures pathologiques.

3. *Développement des méthodes*

Le but de cette partie est de présenter toutes les méthodes développées au cours de ce projet de thèse. L'ensemble du processus est présenté en Figure 62.

Uniquement des souris femelles immuno-déficientes (BalB/c nude, Janvier Laboratories®) ont été utilisées tout au cours de cette étude. Toutes ont été injectées à l'âge de 4 semaines (après une semaine de stabulation). L'ensemble des protocoles d'injection et de développement tumoral présenté ci-dessous a été validé par le comité d'éthique pour l'expérimentation animale de l'Université Claude Bernard Lyon 1.

Tout d'abord, les souris ont été injectées en sous cutané (10^6 cellules dans une solution de 100µL de Solution tampon (Phosphate Buffered Sollution, PBS) à l'aide d'une seringue de 1mL, Myjector (070151, Terumo Japon) après anesthésie. Etant l'objet d'un suivi minutieux, ces dernières ont été sacrifiées lorsque la tumeur atteignait 1cm de diamètre.
Deux types d'échantillons tumoraux ont alors été créés à partir de cellules de lignées tumorales humaines. L'une provenant d'une souche de cancer du sein et provoquant des lésions lytiques (B02). La seconde provenant d'une souche de cancer de la prostate et créant des lésions mixtes (CMET). Il a enfin été possible, au cours du projet, de récupérer un échantillon de myélome (lésion lytique) d'un patient, qui a été ajouté à l'étude pour comparaison.

Les tumeurs résultantes ont ensuite été testées par rhéologie de manière à implémenter le résultat obtenu dans la simulation numérique (FEA). Ce test a été mené sur une machine fabriquée sur mesure de manière à solliciter des tranches d'échantillons de 800µm par un cisaillement harmonique à faible déplacement de 0.1 à 10 000Hz.
Ces tests ont permis de déterminer le module de cisaillement de chacun des échantillons (4 tumeurs coupées en 13 tranches de tumeurs B02, deux tumeurs coupées en 3 tranches de CMET et une tumeur coupée en 13 tranches de myélome).

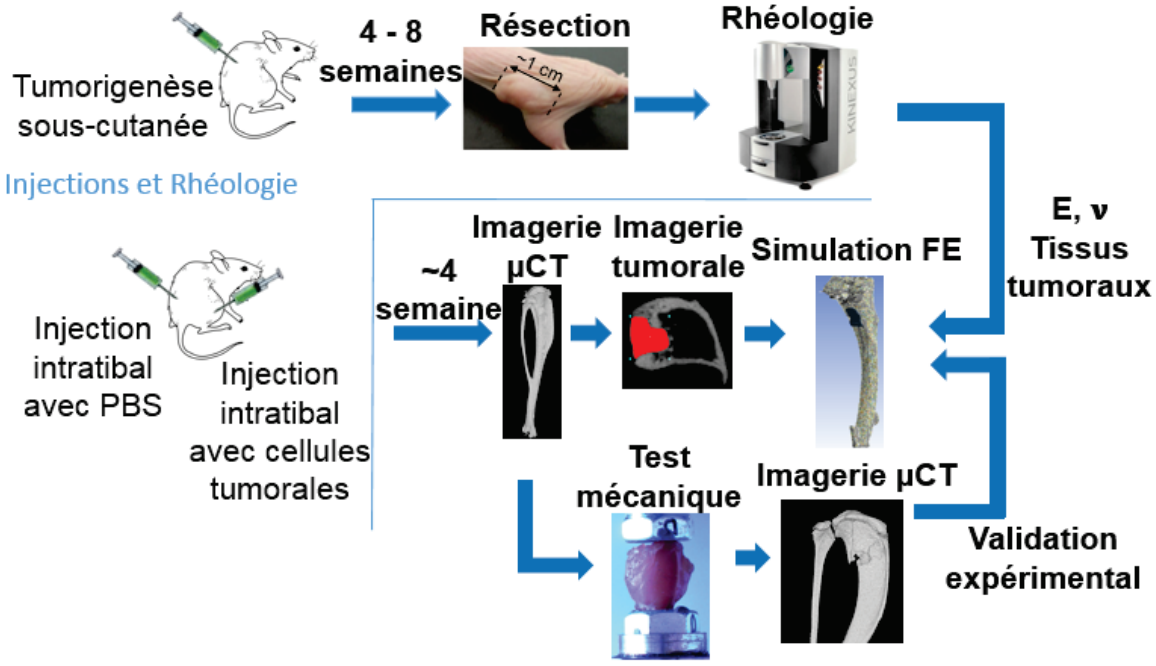

Figure 62: processus de l'étude

Ce module complexe a ensuite été converti en module de Young (module élastique) en se basant sur l'hypothèse d'incompressibilité.

Ainsi, un module de Young de 0.0225 MPa a été obtenu pour les échantillons de B02 contre 0.00225 MPa pour ceux des CMET et 0.3 MPa pour ceux du myélome.

Parallèlement, 16 autres souris (8 par groupes) ont été injectées en intra-tibial par les mêmes souches cellulaires (B02 et CMET) après anesthésie en patte droite (pattes tumorales, Figure 63) et en patte gauche avec du PBS (pattes shams, Figure 63). Huit autres souris ont à leur tour été injectées uniquement en patte droite et gauche par du PBS de manière à fournir des échantillons dans lesquels le cancer ne pourrait pas migrer (pattes contrôles, Figure 63).
A la suite d'un mois de gestation, les animaux ont été sacrifiés via cervico-dislocation, les pattes ont été disséquées et stockées à -20°C jusqu'au jour du test mécanique.

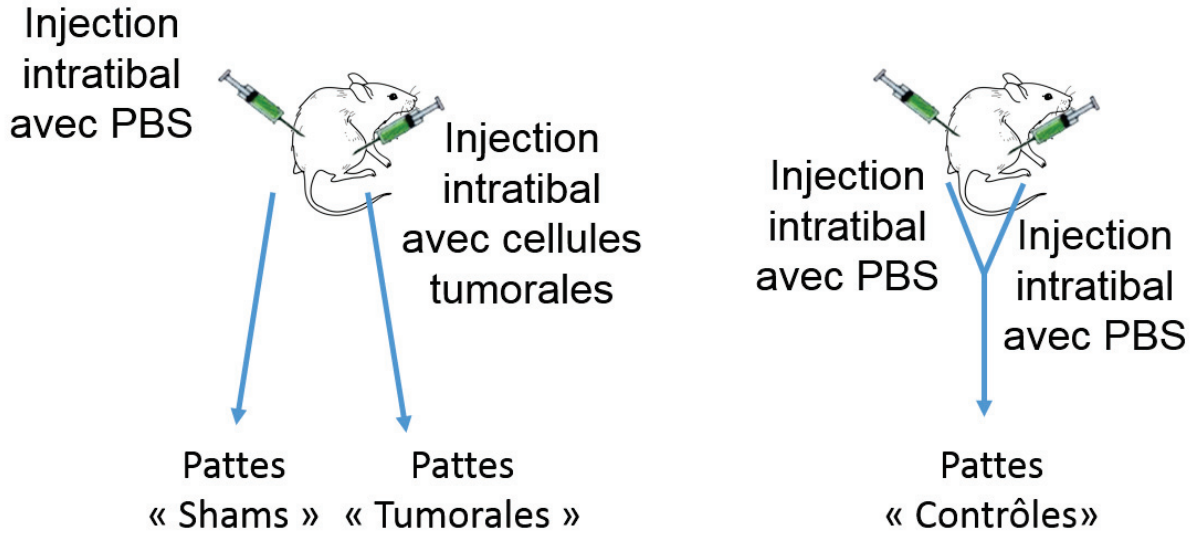

Figure 63: Nomenclature des échantillons en fonction des injections

Il est à noter que la nécessité d'injecter les pattes controlatérales avec du PBS lors d'une étude comparative a fait l'objet d'une recherche spécifique lors de ce projet, et a été publiée (Delpuech et al., 2017).

Une imagerie scanner a été effectuée avant et après les essais mécaniques (Bruker Skyscan 1176 (Kontiche, Belgium), 10 µm de résolution isotropique, (50 kV, 500 µA, filtre aluminium de 0.5mm, pas de rotation 0.6° jusqu'à 180°).
Le scanner avant les essais mécaniques avait pour but de créer le modèle éléments finis (FEA) et celui après, de confirmer et localiser la fracture de l'échantillon.

Les échantillons ont tous suivis la même préparation (Figure 64), implémentant une double rotule, l'encastrement bas étant réalisé à l'aide d'une résine méthacrylate de méthyl à prise rapide (VariDur ref 10-1027, Buehler, USA) et le haut d'une résine époxy (Pattex, Ref 1875423). Le tibia ayant été

séparé des autres os, les ligaments coupés, mais les tissus mous gardés en place de manière à ne pas risquer d'endommager la tumeur pouvant s'y être développée.

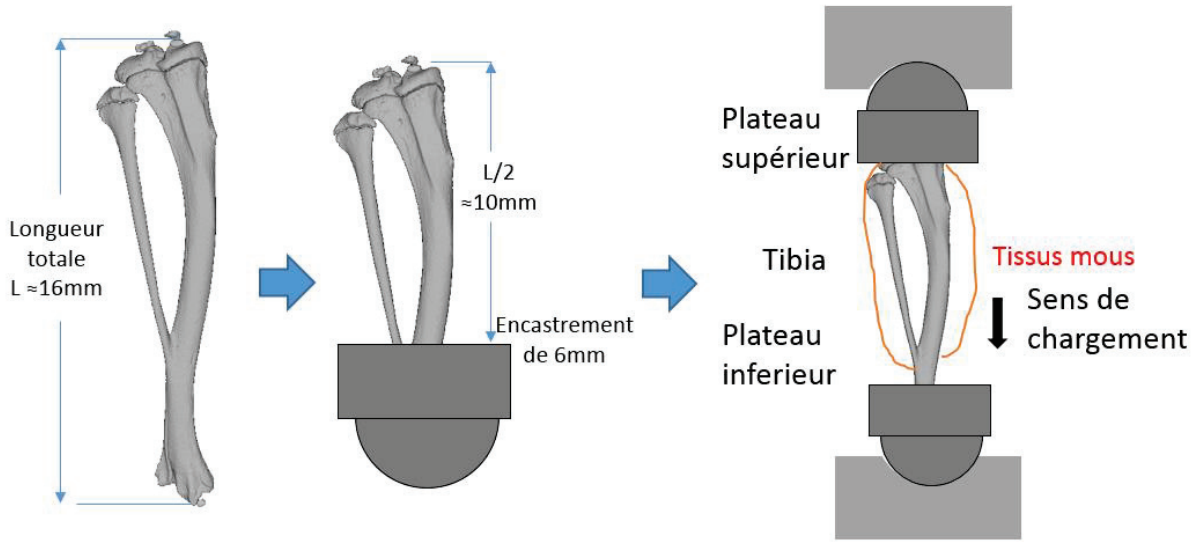

Figure 64: Préparation et position d'essai des échantillons

Les essais mécaniques ont été menés suite à un précyclage de -0.5N à -2N sur 30 cycles à 0.5Hz. L'essai destructif en lui-même a été effectué en compression avec un déplacement imposé de 0.03 mm/s jusqu'à la rupture (Bose Corporation, Eden Prairie, MN: 5500).
Les efforts et déplacements de ces tests ont été enregistrés à 60Hz (WinTest® Digital Control System) à l'aide des capteurs machine (précision de 10 µm en déplacement, 0.04 N en effort).
La raideur et l'effort ultime de chaque échantillon ont été déterminés à partir de ces données.

Les modèles éléments finis ont été créés à partir de l'imagerie scanner avant essais.
Pour ce faire, l'os a d'abord été segmenté de manière à créer un fichier surfacique de l'enveloppe osseuse (fichier STL, CTan 1.16.4.1+, Skyscan Bruker, Kontiche, Belgium, 3DSlicer 4.8.1, National Alliance for Medical Image Computing (NA-MIC)).
Ce fichier surfacique a ensuite été importé et converti en maillage volumique formé de tétraèdres (Ansys 19.0, Ansys inc., Canonsburg, Pennsylvania, USA).
Puis le module de Young de chacun de ces éléments a été corrélé au niveau de minéralisation de l'os qu'occupe chacun des élément à l'aide d'une loi puissance présentée dans la littérature (Easley et al., 2010) avec un seuillage à 0.31 g Ha/mm^3 à l'aide d'un logiciel académique (Bonemat, Istituto Ortopedico Rizzoli, Bologna, Italy).
Enfin, les tests mécaniques ont été simulés (Ansys 19.0, Ansys inc., Canonsburg, Pennsylvania, USA) en imposant la force à rupture sur le premier millimètre d'os (plateaux tibiaux) et un déplacement nul à sa base (Figure 65 C).

La stabilité de la réponse du modèle numérique a été évaluée à l'aide d'une étude de sensibilité (mesure d'évolution de la réponse en fonction du nombre d'éléments) et a permis de déterminer le nombre d'éléments permettant d'allier vitesse de résolution et stabilité de la réponse, ici 200 000 éléments.

Enfin, deux types de modèles ont été créés, l'un uniquement pour les os tumoraux (modèle spécifique Figure 65 A). Ce dernier consistait à segmenter la tumeur de l'os (avec l'hypothèse que la tumeur se trouvait là où une lyse était présente). Ensuite les propriétés mécaniques de l'os ont été définies selon la méthode précédemment décrite, alors que les propriétés de la tumeur ont été implémentées en fonction des résultats rhéologiques.

Le second modèle, développé pour tous les os, a consisté uniquement à suivre la méthode précédemment détaillée (modèle hétérogène Figure 65 B).

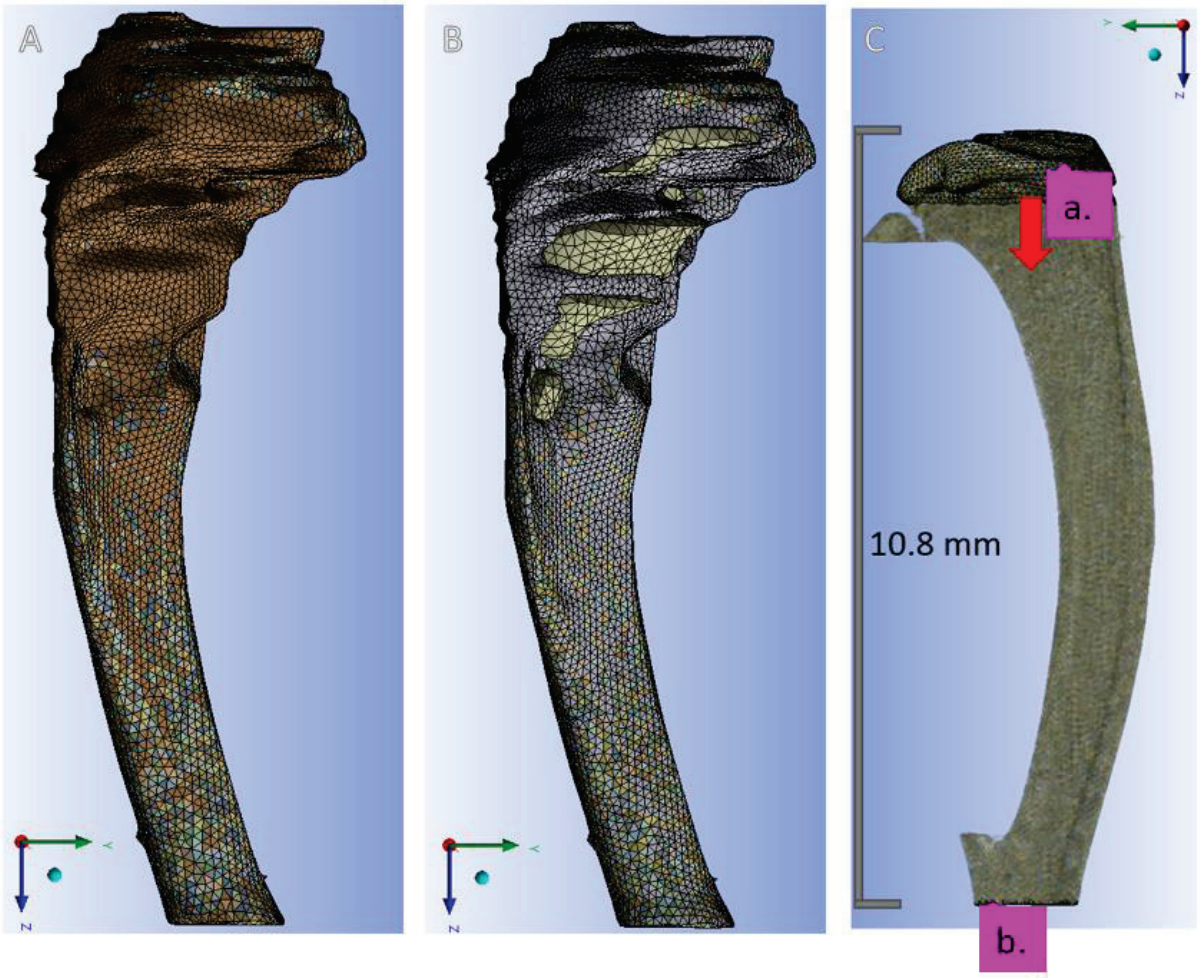

Figure 65: A, modèle hétérogène, B modèle spécifique, C: applications des conditions limites aux modèles (valables pour A et B) avec en a. l'application de la force à rupture et en b. un déplacement nul.

Il est à noter que la FEA a également permis de lever une incertitude. Les forces résultantes sur X et Y (Figure 65) n'ayant pas été enregistrées pendant l'essai (du fait du capteur axial en Z), elles ont été identifiées par la FEA grâce aux raideurs expérimentales et simulées.

Pour finir, les modèles éléments finis étant purement linéaires élastiques (pas d'endommagement) un critère de fracture était nécessaire. Ce dernier a été, à l'instar de la loi de corrélation minéralisation/module de Young, publiée dans la littérature (Pistoia et al., 2002). Basé sur la déformation des éléments et développé sur échantillons humains, il a fait l'objet d'une identification des paramètres les plus pertinents de manière à déterminer la fracture dans le cas du tibia de souris comme dans une autre étude publiée (Nyman et al., 2015).
En conséquence, la fracture a été déterminée sur les modèles numériques, lorsque 2% du volume total des éléments avait subi une déformation de 0.01, retrouvant ainsi le même résultat que l'étude suscitée sur vertèbres de souris (Nyman et al., 2015).

4. *Echantillon tumoraux lytiques*

Cette partie vise à comparer les résultats expérimentaux et de FEA obtenus par le biais des méthodes précédemment détaillées et de les discuter pour ce qui est des échantillons présentant des tumeurs lytiques.

De manière à quantifier le niveau de précision de chacun des modèles en fonction des échantillons étudiés (tumoraux lytiques ou contrôles) leur résultat a été analyser indépendamment les uns des autres.

Dans un premier temps, les résultats des pattes « shams » ont été comparés aux pattes « contrôles » (Tableau 1). Ne montrant pas de différences les unes par rapport aux autres (test de Mann-Whitney non significatif entre les deux groupes), elles ont été analysées ensemble.

Tableau 1:Valeurs de forces ultimes obtenus pour les pattes shams et contrôles, expérimentalement et par FEA (modèle hétérogène)

	Souris	Force Ult. Exp. (N)	Force Ult. FEA (N)	Pourcentage de difference entre Exp. et FEA (%)
Pattes Sham	Souris 1, p. Gauche	19,4	17,0	12
	Souris 2, p. Gauche	17,8	23,9	34
	Souris 3, p. Gauche	18,2	19,8	9
	Souris 4, p. Gauche	17,3	20,4	18
	Souris 5, p. Gauche	27,8	27,3	2
	Souris 6, p. Gauche	29,3	24,4	17
	Souris 7, p. Gauche	28,7	22,6	21
	Souris 8, p. Gauche	22,5	24,0	6
Pattes Contrôles	Souris 9, p. Droite	24,1	20,3	16
	Souris 10, p. Droite	23,4	23,0	1
	Souris 10, p. Gauche	26,6	20,9	22
	Souris 11, p. Droite	17,8	19,2	8
	Souris 11, p. Gauche	21,4	20,0	7
	Souris 12, p. Droite	21,9	21,5	2
	Souris 12, p. Gauche	21,5	23,8	11
	Souris 13, p. Droite	20,4	20,2	1
	Souris 13, p. Gauche	25,2	22,7	10
	Souris 14, p. Droite	20,7	22,8	10
	Souris 14, p. Gauche	26,4	21,8	18
	Souris 15, p. Droite	19,4	18,9	2
	Souris 15, p. Gauche	23,0	21,1	8
	Souris 16, p. Droite	24,8	23,7	5
	Souris 16, p. Gauche	27,5	24,0	13

En moyenne, la différence entre prédiction via FEA et force ultime expérimentale s'est avérée être de 11±8%. Les deux paramètres sont significativement corrélés ($\rho_{spearman}$=0.60, p=0.003).

Ensuite, les valeurs obtenues pour le modèle hétérogène des pattes tumorales ont donné des résultats similaires, la moyennes des pourcentages différences entre FEA et expérimental étant de 12±7% et les deux paramètres étant bien corrélés ($\rho_{spearman}$=0.75, p=0.05, Tableau 2).

Le résultat de la Souris 8 étant une fracture locale (fracture intermédiaire ayant changé les conditions limites et rendant l'échantillon incapable de répondre à la sollicitation) ayant empêché d'atteindre la rupture globale, ce résultat a été retiré de cette comparaison pour être réintégré lors d'une analyse ultérieure.

Tableau 2: Valeurs de forces ultimes obtenues pour les pattes tumorales, expérimentalement et par FEA, modèle hétérogène. Patte non prise en compte lors de cette analyse en gris.

	Souris	Force Ult. Exp. (N)	Force Ult. FEA (N)	Pourcentage de difference entre Exp. et FEA (%)
Pattes Tumorales	Souris 1, p. Droite	20,2	21,0	4
	Souris 2, p. Droite	20,6	22,4	10
	Souris 3, p. Droite	7,7	4,2	19
	Souris 4, p. Droite	13,3	10,6	15
	Souris 5, p. Droite	18,4	22,7	15
	Souris 6, p. Droite	12,5	12,2	1
	Souris 7, p. Droite	11,9	16,5	16
	Souris 8, p. Droite	7,7	18,3	47

Le résultat des modèles spécifiques de ces mêmes pattes, implémenté avec le module des tumeurs (0.0225 MPa) s'est révélé être moins bon, présentant un pourcentage de différence en moyenne de 23±22%, les valeurs expérimentales et de FEA n'étant pas alors plus significativement corrélées ($\rho_{spearman}$=0.77; p=0.04 , Tableau 3).

Tableau 3:Valeurs de forces ultimes obtenus pour les pattes tumorales, expérimentalement et par FEA, modèle spécifique, module B02 (0.0225MPa). Patte non prise en compte lors de cette analyse en gris.

	Souris	Force Ult. Exp. (N)	Force Ult. FEA (N)	Pourcentage de difference entre Exp. et FEA (%)
Pattes Tumorales	Souris 1, p. Droite	20,2	21,1	4,4
	Souris 2, p. Droite	20,6	21,1	2,4
	Souris 3, p. Droite	7,7	3,7	52,2
	Souris 4, p. Droite	13,3	13,1	1,6
	Souris 5, p. Droite	18,4	22,0	19,7
	Souris 6, p. Droite	12,5	7,4	40,5
	Souris 7, p. Droite	11,9	17,0	42,3
	Souris 8, p. Droite	7,7	17,9	133,9

Le module ayant été obtenu sur des tumeurs sous cutanées, et le myélome étant de nature lytique, les mêmes modèles ont été implémentés avec le module obtenu sur le myélome de patient (0.3MPa), montrant à nouveau des résultats corrélés mais avec le même degré d'accord avec l'expérimental (différence moyenne de 24±20%, $\rho_{spearman}$=0.86, p=0.02, Tableau 4).

Tableau 4:Valeurs de forces ultimes obtenus pour les pattes tumorales, expérimentalement et par FEA, modèle spécifique, module myélome (0.3MPa). Patte non prise en compte lors de cette analyse en gris.

	Souris	Force Ult. Exp. (N)	Force Ult. FEA (N)	pourcentage de difference entre Exp. et FEA (%)
Pattes Tumorales	Souris 1, p. Droite	20,2	21,2	4,8
	Souris 2, p. Droite	20,6	22,3	8,5
	Souris 3, p. Droite	7,7	3,7	51,1
	Souris 4, p. Droite	13,3	13,1	1,6
	Souris 5, p. Droite	18,4	22,0	19,7
	Souris 6, p. Droite	12,5	7,5	40,1
	Souris 7, p. Droite	11,9	17,0	42,3
	Souris 8, p. Droite	7,7	17,9	133,9

Ainsi, le fait d'utiliser le module obtenu pour des tumeurs s'étant développées dans l'os (le myélome) a permis d'obtenir des résultats de meilleures qualités pour le modèle spécifique.
Toutefois ces derniers se sont montrés moins proches de l'expérimental que les résultats du modèle hétérogène, qui par ailleurs est plus simple à obtenir, ne demandant pas de segmentation entre tumeur et os.
La prise en compte des propriétés de la tumeur ne semble donc pas permettre une meilleure prédiction de la force ultime dans le cas de tumeurs lytiques, mais ce résultat sera à confirmer dans le cas de tumeurs mixtes (chapitre suivant).

De manière à confirmer le fait que la fracture de la souris 8 était bien une fracture locale, une nouvelle analyse de la FEA a été menée sur les 3mm d'os consécutif à l'application de la force sur le modèle numérique. Cette analyse sera appelée « analyse locale » par la suite. Cette dernière a bien permis de se rapprocher de la valeur de fracture constatée pour la patte tumorale de la souris 8, semblant confirmer notre intuition (Tableau 5).

De manière surprenante, certaines des valeurs locales de pattes tumorales se sont avérées être supérieures à celle de l'analyse globale, malgré la présence de lyse osseuse, en pourcentage de volume plus important.

Plus intéressant, toutes les analyses présentant un pourcentage de différence entre analyse locale et globale en faveur de l'analyse globale (pourcentages négatifs, Tableau 5) de -20% ou plus se sont avérées être les pattes ayant connues des pics de forces multiples sur les courbes expérimentales

lors de leur chargement (traduisant physiquement une rupture locale n'ayant pas empêché la poursuite du chargement) soit une force ultime inferieure à la plus basses des pattes « shams » et « contrôles ».

De manière à confirmer la possible utilisation de cette double analyse, ceci a également été menée sur les pattes shams et contrôles. Aucune n'a montré pareille pourcentage de différence.

Cette différence, permettant apparemment de différencier les os dont la stabilité mécanique pose problème de ceux pour lesquels elle n'en pose pas pourrait être à même d'aider les cliniciens dans leur diagnostic.

Là encore ce résultat sera à confirmer dans le cas des lésions mixtes (Chapitre suivant).

Tableau 5: Résultats FEA des analyses globales et locales, pour les modèles hétérogènes des pattes tumorales, shams et contrôles

	Souris	Force Ult. Exp. (N)	Force Ult. Globale FEA (N)	Force Ult. Locale FEA (N)	Pourcentage de difference entre Force locale et globale FEA (%)
Pattes Tumorales	Souris 1, p. Droite	20,2	21,0	21,4	2
	Souris 2, p. Droite	20,6	22,4	21,1	-6
	Souris 3, p. Droite	7,7	4,2	2,5	-41
	Souris 4, p. Droite	13,3	10,6	6,2	-42
	Souris 5, p. Droite	18,4	22,7	22,3	-2
	Souris 6, p. Droite	12,5	12,2	6,2	-49
	Souris 7, p. Droite	11,9	16,5	12,3	-26
	Souris 8, p. Droite	7,7	18,3	11,7	-36
Pattes Sham	Souris 1, p. Gauche	19,4	17,0	21,1	24
	Souris 2, p. Gauche	17,8	23,9	25,2	6
	Souris 3, p. Gauche	18,2	19,8	19,6	-1
	Souris 4, p. Gauche	17,3	20,4	20,3	0
	Souris 5, p. Gauche	27,8	27,3	27,4	0
	Souris 6, p. Gauche	29,3	24,4	23,7	-3
	Souris 7, p. Gauche	28,7	22,6	26,0	15
	Souris 8, p. Gauche	22,5	24,0	26,5	11
Pattes Contrôles	Souris 9, p. Droite	24,1	20,3	19,1	-6
	Souris 10, p. Droite	23,4	23,0	22,7	-1
	Souris 10, p. Gauche	26,6	20,9	20,2	-3
	Souris 11, p. Droite	17,8	19,2	17,1	-11
	Souris 11, p. Gauche	21,4	20,0	18,1	-9
	Souris 12, p. Droite	21,9	21,5	18,9	-12
	Souris 12, p. Gauche	21,5	23,8	26,2	10
	Souris 13, p. Droite	20,4	20,2	19,3	-4
	Souris 13, p. Gauche	25,2	22,7	20,4	-10
	Souris 14, p. Droite	20,7	22,8	25,0	10
	Souris 14, p. Gauche	26,4	21,8	22,1	1
	Souris 15, p. Droite	19,4	18,9	19,0	0
	Souris 15, p. Gauche	23,0	21,1	20,3	-4
	Souris 16, p. Droite	24,8	23,7	22,8	-4
	Souris 16, p. Gauche	27,5	24,0	23,9	0

5. *Echantillons tumoraux mixtes*

Cette partie vise à comparer les résultats expérimentaux et de FEA obtenus par le biais des méthodes précédemment détaillées et de les discuter pour ce qui est des échantillons présentant des tumeurs mixtes.

De la même manière que pour les échantillons lytiques, les résultats ont, dans un premier temps, été analysés par type d'échantillons (shams et tumoraux) et par type de modèle (spécifique et hétérogène).

Les résultats des pattes shams (contra-latérales des pattes lytiques) ont été analysés séparément des pattes contrôles précédemment présentés, certaines pattes présentant un développement faible de lyses osseuses (pattes gauches des souris 19, 20 et 21).
Quoi qu'il en soit, les résultats des modèles hétérogènes ont été dans les mêmes ordres de grandeurs de ceux précédemment obtenus, le pourcentage de différence entre force ultime expérimentale et prédite par la FEA s'élevant à 11±8%, et les deux résultats étant significativement statistiquement liés ($\rho_{spearman}$=0.71, p=0.05, Tableau 6).

Tableau 6: Valeurs de forces ultimes obtenues pour les pattes shams, expérimentalement et par FEA, modèle hétérogène.

	Souris	Force Ult. Exp. (N)	Force Ult. FEA (N)	Pourcentage de difference entre Exp. et FEA (%)
Pattes Sham	Souris 17, p. Gauche	21,0	21,5	3
	Souris 18, p. Gauche	24,2	23,2	4
	Souris 19, p. Gauche	14,1	15,7	12
	Souris 20, p. Gauche	26,6	20,3	24
	Souris 21, p. Gauche	30,1	23,4	22
	Souris 22, p. Gauche	17,1	15,7	8
	Souris 23, p. Gauche	23,1	21,9	5
	Souris 24, p. Gauche	21,0	22,6	8

Les lyses osseuses étant plus développées pour les échantillons tumoraux mixtes que lytiques, trois pattes ont connu une rupture locale empêchant de continuer le chargement de l'échantillon à la manière de la patte tumorale de la souris 8 du chapitre précédent. De la même manière, ces trois pattes (pattes droite des souris 19, 20 et 21) ont été retirées de la comparaison entre forces ultimes obtenues expérimentalement et par FEA.

Ces résultats ne reposant plus que sur 5 échantillons, la corrélation entre force ultime expérimentale et simulée (FEA) n'as pas pu être prouvée ($\rho_{spearman}$ non significatif) et le pourcentage de différence s'est avéré plus élevé que les précédemment rapportés pour les modèles hétérogènes (22±14%, Tableau 7).

Toutefois, ce résultat étant le premier non significatif observé sur les modèles hétérogènes, cette non significativité a été mise sur le compte d'un effectif trop faible, et les comparaisons ont tout de même été poursuivies.

Tableau 7:Valeurs de forces ultimes obtenues pour les pattes tumorales, expérimentalement et par FEA, modèle hétérogène. Pattes non prises en compte pour la comparaison en gris.

	Souris	Force Ult. Exp. (N)	Force Ult. FEA (N)	Pourcentage de difference entre Exp. et FEA (%)
Pattes Tumorales	Souris 17, p. Droite	11,3	14,9	32
	Souris 18, p. Droite	14,7	15,2	3
	Souris 19, p. Droite	4,0	7,9	101
	Souris 20, p. Droite	4,6	7,8	70
	Souris 21, p. Droite	5,8	9,6	65
	Souris 22, p. Droite	14,6	12,1	17
	Souris 23, p. Droite	26,5	21,8	17
	Souris 24, p. Droite	16,8	10,3	39

Ce problème de faible effectif a empiré sur les modèles spécifiques. En effet, les tumeurs étant bien plus étendues que les précédentes, des problèmes de gestions de contact sont apparus, empêchant la moitié des simulations d'aboutir (4/8). Malheureusement, l'une des simulations ayant aboutie était celle d'une patte retirée de la comparaison expérimentale/FEA. Cet état de fait nous laissant avec seulement trois résultats de modèle spécifique tumoraux mixtes, aucune analyse statistique n'a été menée et les résultats présents en Tableau 8 le sont uniquement à titre illustratif.

Tableau 8: Valeurs de forces ultimes obtenues pour les pattes tumorales, expérimentalement et par FEA, modèle hétérogène. Pattes non prises en compte pour la comparaison en gris et simulation n'ayant pas abouties du fait de problèmes de gestion de contact de la simulation en rouge.

	Souris	Force Ult. Exp. (N)	Force Ult. FEA (N)	Pourcentage de difference entre Exp. et FEA (%)
Pattes Tumorales	Souris 17, p. Droite	11,3	4,1	63,7
	Souris 18, p. Droite	14,7	7,8	47,1
	Souris 19, p. Droite	4,0	2,6	34,3
	Souris 20, p. Droite	4,6		
	Souris 21, p. Droite	5,8		
	Souris 22, p. Droite	14,6		
	Souris 23, p. Droite	26,5	21,9	17,1
	Souris 24, p. Droite	16,8		

Les faibles effectifs des simulations des modèles hétérogènes (n=5) et des modèles spécifiques (n=3) permet difficilement de conclure quant à la différence entre les deux modèles.

Toutefois, le pourcentage de différence moyen entre force ultime prédite par FEA du modèle hétérogène (22±14%) reste bien inférieur à celui des modèles spécifiques (48±15%), ne semblant pas présager une amélioration quant à ce qui a été observé pour les tumeurs lytiques. A cela s'ajoute le problème de gestion de contact du logiciel éléments finis, inhérent à la nature même du modèle spécifique et semblant en dépeindre une nouvelle limite.
Ainsi, le modèle spécifique ne semble pas apporter d'amélioration pour la prédiction de fracture des os tumoraux dans le cas de lésions mixtes non plus.

Enfin, l'analyse locale a également été menée sur les modèles hétérogènes des pattes shams et tumorales des échantillons à lésions mixtes (Tableau 9). Le but de cette comparaison était de confirmer le résultat obtenu sur les pattes présentant des tumeurs lytiques du chapitre précédant, à savoir que les pattes présentant une instabilité mécanique présenteraient une différence entre force ultime locale et globale de -20% (en faveur de la globale). L'instabilité mécanique a ici été définie comme étant soit la présence d'une discontinuité forte dans la courbe de chargement des échantillons (traduisant une rupture locale n'ayant pas empêché la suite du test), soit présentant un effort ultime inférieur à la plus basse valeur constatée pour les pattes contrôles et shams, en excluant les shams présentant des signes de tumeurs (pattes shams des souris 19, 20 et 21).

Bien qu'ayant permis de détecter la majorité des cas décrits précédemment, deux pattes présentant une instabilité mécanique n'ont pas été détectées (Pattes droites des souris 17 et 24). Il est à noter que la différence de -20% à toutefois permis de détecter l'instabilité mécanique d'une patte sham ayant présentée de très faibles lyses (patte gauche de la souris 19).

Visant à pouvoir détecter l'ensemble des instabilités mécaniques, l'analyse a été poussée en incluant notamment le poids des souris (chapitre suivant).

Tableau 9:Résultats FEA des analyses globales et locales, pour les modèles hétérogènes des pattes tumorales

	Mice	Experimental Ult. Load (N)	FEA Ult. Load (N)	FEA local Ult. Load (N)	Difference percentage beetwen local and global FEA failure (%)
Pattes Tumorales	Souris 17, p. Droite	11,3	14,9	12,9	-13
	Souris 18, p. Droite	14,7	15,2	11,8	-22
	Souris 19, p. Droite	4,0	7,9	5,5	-31
	Souris 20, p. Droite	4,6	7,8	5,4	-30
	Souris 21, p. Droite	5,8	9,6	7,6	-21
	Souris 22, p. Droite	14,6	12,1	7,8	-35
	Souris 23, p. Droite	26,5	21,8	25,1	15
	Souris 24, p. Droite	16,8	10,3	10,2	-1
Pattes Sham	Souris 17, p. Gauche	21,0	21,5	23,0	7
	Souris 18, p. Gauche	24,2	23,2	23,8	3
	Souris 19, p. Gauche	14,1	15,7	12,0	-24
	Souris 20, p. Gauche	26,6	20,3	19,1	-6
	Souris 21, p. Gauche	30,1	23,4	25,0	7
	Souris 22, p. Gauche	17,1	15,7	14,3	-9
	Souris 23, p. Gauche	23,1	21,9	21,6	-1
	Souris 24, p. Gauche	21,0	22,6	21,0	-7

6. *Amélioration de la prédiction du risque d'instabilité mécanique*

De manière à prédire l'instabilité mécanique, le poids des souris a été ajouté et l'analyse poussée, de manière à pouvoir discriminer efficacement les pattes présentant une instabilité de celles n'en présentant pas. L'instabilité mécanique a ici été définie comme étant soit la présence d'une discontinuité forte dans la courbe de chargement des échantillons (traduisant une rupture locale n'ayant pas empêché la suite du test) soit un effort ultime inférieur plus bas que ceux constatés pour les pattes contrôles et sham, en excluant les shams présentant des signes de tumeurs (pattes shams des souris 19, 20 et 21). L'ensemble de ces données est présenté en Tableau 10.

Dans chacun des cas, la sensibilité (permettant de quantifier la capacité du critère à déterminer les os présentant une instabilité mécanique, et calculée comme étant le rapport des vrais positifs et de la somme des vrais positifs et faux positifs) et la spécificité (permettant de quantifier la capacité du critère à déterminer les os ne présentant pas d'instabilité mécanique, et calculée comme étant le rapport des vrais négatifs et de la somme des vrais négatifs et faux négatifs) ont été calculées pour chacun des critères de détection avancés.

Ainsi, la différence de 20% entre force ultime locale et globale en faveur de la globale présentait une sensibilité de 85% et une spécificité de 100%.

Cherchant à augmenter la sensibilité du critère de diagnostic, le poids des souris a été divisé par la force ultime globale prédite. Le seuil de détection étant fixé au ratio maximum des pattes présentant une instabilité mécanique (ici 0.82 g/N, souris 19 pattes shams).
Ce nouveau critère atteignit une sensibilité de 100%, mais une spécificité de 94%, ne permettant pas encore un diagnostic juste dans tous les cas (Tableau 10).

La même procédure fut alors entreprise avec la force ultime locale prédite par FEA (ratio du poids et de cette dernière). Encore une fois, le seuil de détection de l'instabilité mécanique a été fixée au ratio maximum des pattes définies comme instables (ici 0.63 g/N, souris 19).

Ce nouveau critère a permis de bien détecter l'ensemble des pattes, à la fois instables et stables, atteignant une sensibilité et une spécificité de 100% (Tableau 10).

Tableau 10:Détection de l'instabilité mécanique pour tous les os inclus dans l'étude (n=47 pattes). L'instabilité mécanique à ici été définie comme étant : 1° soit la présence d'une discontinuité forte dans la courbe de chargement des échantillons (traduisant une rupture locale n'ayant pas empêchée la suite du test), 2° soit présentant un effort ultime inférieur à la plus basse de celle constatée chez les pattes contrôles et shams, en excluant les shams présentant des signes de tumeurs (pattes shams des souris 19, 20 et 21).

	Souris	Resultats					Prediction d'instabilité mécanique (vert: vrai negatif, jaune:faux négatif, rouge: vrai positif, orange: faux positif)		
		Force Ult. Exp. (N)	Stabilité mécanique (rouge: instable, vert: stable)	Force Ult. Globale FEA (N)	Force Ult. Locale FEA (N)	Poids des Souris (g)	Pourcentage de difference entre Exp. et FEA (%)	Poids/Force Ult. Globale FEA	Poids/Force Ult. Locale FEA
Pattes Tumorales B02	Souris 1, p. Droite	20.2		21.0	21.4	21.8	2	0.96	0.98
	Souris 2, p. Droite	20.6		22.4	21.1	21.9	-6	1.02	0.96
	Souris 3, p. Droite	7.7		4.2	2.5	19.1	-41	0.22	0.13
	Souris 4, p. Droite	13.3		10.6	6.2	19.4	-42	0.55	0.32
	Souris 5, p. Droite	18.4		22.7	22.3	25.1	-2	0.90	0.89
	Souris 6, p. Droite	12.5		12.2	6.2	23.2	-49	0.53	0.27
	Souris 7, p. Droite	11.9		16.5	12.3	21.7	-26	0.76	0.56
	Souris 8, p. Droite	7.7		18.3	11.7	23.5	-36	0.78	0.50
Pattes Sham	Souris 1, p. Gauche	19.4		17.0	21.1	21.8	24	0.78	0.97
	Souris 2, p. Gauche	17.8		23.9	25.2	21.9	6	1.09	1.15
	Souris 3, p. Gauche	18.2		19.8	19.6	19.1	-1	1.04	1.03
	Souris 4, p. Gauche	17.3		20.4	20.3	19.4	0	1.05	1.05
	Souris 5, p. Gauche	27.8		27.3	27.4	25.1	0	1.09	1.09
	Souris 6, p. Gauche	29.3		24.4	23.7	23.2	-3	1.05	1.02
	Souris 7, p. Gauche	28.7		22.6	26.0	21.7	15	1.04	1.20
	Souris 8, p. Gauche	22.5		24.0	26.5	23.5	11	1.02	1.13
Pattes Contrôles	Souris 9, p. Droite	24.1		20.3	19.1	23.0	-6	0.88	0.83
	Souris 10, p. Droite	23.4		23.0	22.7	21.7	-1	1.06	1.05
	Souris 10, p. Gauche	26.6		20.9	20.2	21.7	-3	0.96	0.93
	Souris 11, p. Droite	17.8		19.2	17.1	20.3	-11	0.95	0.84
	Souris 11, p. Gauche	21.4		20.0	18.1	20.3	-9	0.98	0.89
	Souris 12, p. Droite	21.9		21.5	18.9	24.0	-12	0.90	0.79
	Souris 12, p. Gauche	21.5		23.8	26.2	24.0	10	0.99	1.09
	Souris 13, p. Droite	20.4		20.2	19.3	25.3	-4	0.80	0.76
	Souris 13, p. Gauche	25.2		22.7	20.4	25.3	-10	0.90	0.81
	Souris 14, p. Droite	20.7		22.8	25.0	22.5	10	1.02	1.11
	Souris 14, p. Gauche	26.4		21.8	22.1	22.5	1	0.97	0.98
	Souris 15, p. Droite	19.4		18.9	19.0	21.3	0	0.89	0.89
	Souris 15, p. Gauche	23.0		21.1	20.3	21.3	-4	0.99	0.95
	Souris 16, p. Droite	24.8		23.7	22.8	24.8	-4	0.95	0.92
	Souris 16, p. Gauche	27.5		24.0	23.9	24.8	0	0.97	0.96
Pattes Tumorales CMET	Souris 17, p. Droite	11.3		14.9	12.9	20.8	-13	0.72	0.62
	Souris 18, p. Droite	14.7		15.2	11.8	21.5	-22	0.71	0.55
	Souris 19, p. Droite	4.0		7.9	5.5	19.1	-31	0.42	0.29
	Souris 20, p. Droite	4.6		7.8	5.4	19.3	-30	0.40	0.28
	Souris 21, p. Droite	5.8		9.6	7.6	21.3	-21	0.45	0.36
	Souris 22, p. Droite	14.6		12.1	7.8	17.4	-35	0.69	0.45
	Souris 23, p. Droite	26.5		21.8	25.1	22.9	15	0.95	1.10
	Souris 24, p. Droite	16.8		10.3	10.2	23.3	-1	0.44	0.44
Pattes Sham	Souris 17, p. Gauche	21.0		21.5	23.0	20.8	7	1.04	1.11
	Souris 18, p. Gauche	24.2		23.2	23.8	21.5	3	1.08	1.11
	Souris 19, p. Gauche	14.1		15.7	12.0	19.1	-24	0.82	0.63
	Souris 20, p. Gauche	26.6		20.3	19.1	19.3	-6	1.05	0.99
	Souris 21, p. Gauche	30.1		23.4	25.0	21.3	7	1.10	1.17
	Souris 22, p. Gauche	17.1		15.7	14.3	17.4	-9	0.90	0.82
	Souris 23, p. Gauche	23.1		21.9	21.6	22.9	-1	0.96	0.94
	Souris 24, p. Gauche	21.0		22.6	21.0	23.3	-7	0.97	0.90

7. *Conclusion et perspectives*

Tout d'abord, les résultats obtenus avec nos modèles hétérogènes ont montré une bonne consistance avec la littérature, la corrélation entre tous les modèles hétérogènes (fractures locales exclues, n=43 pattes) quant à la fracture simulée et expérimentale étant du même ordre de grandeur que celles d'une étude analogue menée sur vertèbres de souris (RMSE de l'ensemble de nos résultats de 3.3 contre 5 et R^2 de 0.65 contre 0.70 respectivement, (Nyman et al., 2015)).

Ensuite, le modèle prenant en compte les propriétés des tumeurs n'as pas permis d'améliorer la prédiction de fracture, au contraire, la moyenne des différences de ces modèles étant de 30±21% (n=11 pattes, modules du myélome pour les pattes lytiques et module des CMET pour les mixtes) contre 12±9% (n=43 pattes, incluant pattes contrôles, shams et tumorales de tous les groupes).
De plus, le modèle spécifique (prenant en compte le module des tumeurs) étant plus difficile à obtenir que le modèle hétérogène (ne nécessitant pas de segmentation entre os et tumeur), le premier ne semble pas être judicieux dans la prédiction de fracture d'os long présentant des lyses osseuses.

Enfin, un critère de détection reposant sur la différence entre valeurs de forces ultimes globale et locale a permis de détecter la majorité des instabilités mécaniques constatées dans cette étude (sensibilité de 85% et spécificité de 100%). Un autre critère, basé sur le ratio entre poids des individus et la force ultime locale prédite via FEA a permis de correctement diagnostiquer l'ensemble des cas (100% de sensibilité et de spécificité).
Ce résultat pourrait s'avérer être d'une grande aide quant à la prise de décision d'intervention chirurgicale dans le cas d'os long atteints de métastases osseuses.
Bien sûr, avant cela, la route à parcourir reste longue, ce résultat devant d'abord être confirmé cliniquement (possiblement en ayant recours à l'étude d'une cohorte rétrospective, comme cela a déjà pu être fait dans d'autres études(Eggermont et al., 2018)).
L'obtention des modèles FEA, ainsi que leur résolution, devront également être automatisées, pour pouvoir aider les cliniciens dans leur pratique clinique courante.

Cette étude a plusieurs limites. Tout d'abord elle est basée sur un modèle animal alors qu'elle vise à identifier les mécanismes de fracture d'os tumoraux intervenant chez des patients. Ensuite l'étude a été menée en *ex vivo*. Enfin le cas de chargement étudié (chargement axial jusqu'à rupture en quasi statique) n'est pas nécessairement représentatif de la sollicitation que connait sur l'os d'un patient au cours de la vie quotidienne (orientations complexes, chargements mécaniques dynamiques).

Cependant, certaines études connaissant le même type de limitations (par exemple(Mann et al., 2008) travaillant sur modèle animal *ex vivo* d'os tumoraux en quasi statique et (Derikx et al., 2012) travaillant sur échantillon *ex vivo* en quasi statique également) ont montré une grande consistance de leurs résultats une fois ramenés dans le cas clinique (Eggermont et al., 2018; Goodheart et al., 2015)

Cet état de fait nous permet de conclure cette étude sur une note optimiste quant à l'application de ces résultats en clinique. Cette étude vient d'être initiée dans le cas du projet MEKANOS (étude multicentrique en France) porté par le Professeur Cyrille Confavreux (rhumatologue).

8. *Références bibliographiques*

Anatomy and Physiology | Simple Book Production [WWW Document], n.d. URL https://courses.lumenlearning.com/nemcc-ap/ (accessed 7.19.18).

Arguello, F., Baggs, R.B., Frantz, C.N., 1988. A Murine Model of Experimental Metastasis to Bone and Bone Marrow. Cancer Res. 48, 6876–6881.

Ascenzi, M.-G., Lutz, A., Du, X., Klimecky, L., Kawas, N., Hourany, T., Jahng, J., Chin, J., Tintut, Y., Nackenhors, U., Keyak, J., 2014. Hyperlipidemia affects multiscale structure and strength of murine femur. J. Biomech. 47, 2436–2443. https://doi.org/10.1016/j.jbiomech.2014.04.006

Attar, S., Steffner, R.J., Avedian, R., Hussain, W.M., 2012. Surgical intervention of nonvertebral osseous metastasis. Cancer Control J. Moffitt Cancer Cent. 19, 113–121. https://doi.org/10.1177/107327481201900205

Benca, E., Reisinger, A., Patsch, J.M., Hirtler, L., Synek, A., Stenicka, S., Windhager, R., Mayr, W., Pahr, D.H., 2017. Effect of simulated metastatic lesions on the biomechanical behavior of the proximal femur. J. Orthop. Res. 35, 2407–2414. https://doi.org/10.1002/jor.23550

Benca, E., Synek, A., Amini, M., Kainberger, F., Hirtler, L., Windhager, R., Mayr, W., Pahr, D.H., 2019. QCT-based finite element prediction of pathologic fractures in proximal femora with metastatic lesions. Sci. Rep. 9. https://doi.org/10.1038/s41598-019-46739-y

Bessho, M., Ohnishi, I., Matsumoto, T., Ohashi, S., Matsuyama, J., Tobita, K., Kaneko, M., Nakamura, K., 2009. Prediction of proximal femur strength using a CT-based nonlinear finite element method: Differences in predicted fracture load and site with changing load and boundary conditions. Bone 45, 226–231. https://doi.org/10.1016/j.bone.2009.04.241

Bone Remodeling [WWW Document], n.d. URL https://courses.washington.edu/conj/bess/bone/bone2.html (accessed 7.24.18).

Boundless Anatomy and Physiology | Simple Book Publishing [WWW Document], n.d. URL https://courses.lumenlearning.com/boundless-ap/ (accessed 6.5.19).

Boyd, S.K., Szabo, E., Ammann, P., 2011. Increased bone strength is associated with improved bone microarchitecture in intact female rats treated with strontium ranelate: A finite element analysis study. Bone 48, 1109–1116. https://doi.org/10.1016/j.bone.2011.01.004

Burkhart, T.A., Andrews, D.M., Dunning, C.E., 2013. Finite element modeling mesh quality, energy balance and validation methods: A review with recommendations associated with the modeling of bone tissue. J. Biomech. 46, 1477–1488. https://doi.org/10.1016/j.jbiomech.2013.03.022

Cazzato, R.L., Garnon, J., Koch, G., Shaygi, B., Tsoumakidou, G., Caudrelier, J., Boatta, E., Buy, X., Palussiere, J., Gangi, A., 2018. Current role of interventional radiology in the management of visceral and bone metastases from thyroid cancer. Gland Surg. 7, 80–88. https://doi.org/10.21037/gs.2017.12.08

Cheal, E.J., Hipp, J.A., Hayes, W.C., 1993. Evaluation of finite element analysis for prediction of the strength reduction due to metastatic lesions in the femoral neck. J. Biomech. 26, 251–264. https://doi.org/10.1016/0021-9290(93)90363-J

Chevalier, Y., Pahr, D., Allmer, H., Charlebois, M., Zysset, P., 2007. Validation of a voxel-based FE method for prediction of the uniaxial apparent modulus of human trabecular bone using macroscopic mechanical tests and nanoindentation. J. Biomech. 40, 3333–3340. https://doi.org/10.1016/j.jbiomech.2007.05.004

Coleman, R.E., 1997. Skeletal complications of malignancy. Cancer 80, 1588–1594.

De Souza, R.L., Matsuura, M., Eckstein, F., Rawlinson, S.C.F., Lanyon, L.E., Pitsillides, A.A., 2005. Non-invasive axial loading of mouse tibiae increases cortical bone formation and modifies

trabecular organization: A new model to study cortical and cancellous compartments in a single loaded element. Bone 37, 810–818. https://doi.org/10.1016/j.bone.2005.07.022

Delpuech, B., Confavreux, C., Bouazza, L., Geraci, S., Clezardin, P., Mitton, D., Follet, H., 2017. Effect of intra-tibial injection on mechanical properties of mouse bone. Comput. Methods Biomech. Biomed. Engin. 20, 57–58. https://doi.org/10.1080/10255842.2017.1382859

Derikx, L.C., van Aken, J.B., Janssen, D., Snyers, A., van der Linden, Y.M., Verdonschot, N., Tanck, E., 2012. The assessment of the risk of fracture in femora with metastatic lesions. J. Bone Joint Surg. Br. 94-B, 1135–1142. https://doi.org/10.1302/0301-620X.94B8.28449

Derikx, L.C., Verdonschot, N., Tanck, E., 2015. Towards clinical application of biomechanical tools for the prediction of fracture risk in metastatic bone disease. J. Biomech. 48, 761–766. https://doi.org/10.1016/j.jbiomech.2014.12.017

Du, Z., Zang, J., Tang, X., Guo, W., 2010. Experts' agreement on therapy for bone metastases. Orthop. Surg. 2, 241–253. https://doi.org/10.1111/j.1757-7861.2010.00095.x

Duchemin, L., Mitton, D., Jolivet, E., Bousson, V., Laredo, J.D., Skalli, W., 2008. An anatomical subject-specific FE-model for hip fracture load prediction. Comput. Methods Biomech. Biomed. Engin. 11, 105–111. https://doi.org/10.1080/10255840802297143

Easley, S.K., Jekir, M.G., Burghardt, A.J., Li, M., Keaveny, T.M., 2010. Contribution of the intra-specimen variations in tissue mineralization to PTH- and raloxifene-induced changes in stiffness of rat vertebrae. Bone 46, 1162–1169. https://doi.org/10.1016/j.bone.2009.12.009

Edwards, J.R., Nyman, J.S., Lwin, S.T., Moore, M.M., Esparza, J., O'Quinn, E.C., Hart, A.J., Biswas, S., Patil, C.A., Lonning, S., Mahadevan-Jansen, A., Mundy, G.R., 2010. Inhibition of TGF-β signaling by 1D11 antibody treatment increases bone mass and quality in vivo. J. Bone Miner. Res. 25, 2419–2426. https://doi.org/10.1002/jbmr.139

Eggermont, F., Derikx, L.C., Verdonschot, N., van der Geest, I.C.M., de Jong, M. a. A., Snyers, A., van der Linden, Y.M., Tanck, E., 2018. Can patient-specific finite element models better predict fractures in metastatic bone disease than experienced clinicians? Bone Jt. Res. 7, 430–439. https://doi.org/10.1302/2046-3758.76.BJR-2017-0325.R2

El-Hamalawi, A., 2000. A simple and effective element distortion factor. https://doi.org/10.1016/S0045-7949(99)00105-4

Erdemir, A., Guess, T.M., Halloran, J., Tadepalli, S.C., Morrison, T.M., 2012. Considerations for Reporting Finite Element Analysis Studies in Biomechanics. J. Biomech. 45, 625–633. https://doi.org/10.1016/j.jbiomech.2011.11.038

Fathers, K.E., Bell, E.S., Rajadurai, C.V., Cory, S., Zhao, H., Mourskaia, A., Zuo, D., Madore, J., Monast, A., Mes-Masson, A.-M., Grosset, A.-A., Gaboury, L., Hallet, M., Siegel, P., Park, M., 2012. Crk adaptor proteins act as key signaling integrators for breast tumorigenesis. Breast Cancer Res. BCR 14, R74. https://doi.org/10.1186/bcr3183

Fellipa, C., 2012. FEM modeling : Mesh, Loads and BCs, Chapter7. [WWW Document]. URL http://kis.tu.kielce.pl//mo/COLORADO_FEM/colorado/IFEM.Ch07.index.html (accessed 4.15.19).

Fidler, M., 1973. Prophylactic Internal Fixation of Secondary Neoplastic Deposits in Long Bones. Br. Med. J. 1, 341–343.

Fritton, J.C., Myers, E.R., Wright, T.M., van der Meulen, M.C.H., 2005a. Loading induces site-specific increases in mineral content assessed by microcomputed tomography of the mouse tibia. Bone 36, 1030–1038. https://doi.org/10.1016/j.bone.2005.02.013

Fritton, J.C., Myers, E.R., Wright, T.M., van der Meulen, M.C.H., 2005b. Loading induces site-specific increases in mineral content assessed by microcomputed tomography of the mouse tibia. Bone 36, 1030–1038. https://doi.org/10.1016/j.bone.2005.02.013

Fung, Y.C., 1993. Biomechanics: Mechanical Properties of Living Tissues, 2nd ed. Springer-Verlag, New York.

Gardner, M.J., Meulen, M.C.H. van der, Demetrakopoulos, D., Wright, T.M., Myers, E.R., Bostrom, M.P., 2006. In Vivo Cyclic Axial Compression Affects Bone Healing in the Mouse Tibia. J. Orthop. Res. Off. Publ. Orthop. Res. Soc. 24, 1679–1686. https://doi.org/10.1002/jor.20230

Geis, C., Graulich, M., Wissmann, A., Hagenacker, T., Thomale, J., Sommer, C., Schäfers, M., 2010. Evoked pain behavior and spinal glia activation is dependent on tumor necrosis factor receptor 1 and 2 in a mouse model of bone cancer pain. Neuroscience 169, 463–474. https://doi.org/10.1016/j.neuroscience.2010.04.022

Goodheart, J.R., Cleary, R.J., Damron, T.A., Mann, K.A., 2015. Simulating activities of daily living with finite element analysis improves fracture prediction for patients with metastatic femoral lesions. J. Orthop. Res. 33, 1226–1234. https://doi.org/10.1002/jor.22887

Harrington, K.D., 1982. New trends in the management of lower extremity metastases. Clin. Orthop. 53–61.

Higinbotham, N.L., Marcove, R.C., 1965. THE MANAGEMENT OF PATHOLOGICAL FRACTURES. J. Trauma Acute Care Surg. 5, 792.

Holguin, N., Brodt, M.D., Sanchez, M.E., Kotiya, A.A., Silva, M.J., 2013. Adaptation of Tibial Structure and Strength to Axial Compression Depends on Loading-History in Both C57BL/6 and BALB/C Mice. Calcif. Tissue Int. 93, 211–221. https://doi.org/10.1007/s00223-013-9744-4

Hong, J., Cabe, G.D., Tedrow, J.R., Hipp, J.A., Snyder, B.D., 2004. Failure of trabecular bone with simulated lytic defects can be predicted non-invasively by structural analysis. J. Orthop. Res. 22, 479–486. https://doi.org/10.1016/j.orthres.2003.09.006

Hoskin, P.J., 2003. Bisphosphonates and radiation therapy for palliation of metastatic bone disease. Cancer Treat. Rev. 29, 321–327. https://doi.org/10.1016/S0305-7372(03)00013-6

Iannaccone, P.M., Jacob, H.J., 2009. Rats! Dis. Model. Mech. 2, 206–210. https://doi.org/10.1242/dmm.002733

Jepsen, K.J., Silva, M.J., Vashishth, D., Guo, X.E., van der Meulen, M.C., 2015. Establishing Biomechanical Mechanisms in Mouse Models: Practical Guidelines for Systematically Evaluating Phenotypic Changes in the Diaphyses of Long Bones. J. Bone Miner. Res. Off. J. Am. Soc. Bone Miner. Res. 30, 951–966. https://doi.org/10.1002/jbmr.2539

Katagiri, H., Takahashi, M., Wakai, K., Sugiura, H., Kataoka, T., Nakanishi, K., 2005. Prognostic factors and a scoring system for patients with skeletal metastasis. J. Bone Joint Surg. Br. 87-B, 698–703. https://doi.org/10.1302/0301-620X.87B5.15185

Keyak, J.H., Kaneko, T.S., Rossi, S.A., Pejcic, M.R., Tehranzadeh, J., Skinner, H.B., 2005. Predicting the strength of femoral shafts with and without metastatic lesions. Clin. Orthop. 439, 161–170.

Keyak, J.H., Kaneko, T.S., Skinner, H.B., Hoang, B.H., 2007. The effect of simulated metastatic lytic lesions on proximal femoral strength. Clin. Orthop. 459, 139–145. https://doi.org/10.1097/BLO.0b013e3180514caa

Keyak, J.H., Lee, I.Y., Nath, D.S., Skinner, H.B., 1996. Postfailure compressive behavior of tibial trabecular bone in three anatomic directions. J. Biomed. Mater. Res. 31, 373–378. https://doi.org/10.1002/(SICI)1097-4636(199607)31:3<373::AID-JBM11>3.0.CO;2-K

Keyak, J.H., Rossi, S.A., Jones, K.A., Les, C.M., Skinner, H.B., 2001. Prediction of fracture location in the proximal femur using finite element models. Med. Eng. Phys. 23, 657–664.

Keyak, J.H., Sigurdsson, S., Karlsdottir, G.S., Oskarsdottir, D., Sigmarsdottir, A., Kornak, J., Harris, T.B., Sigurdsson, G., Jonsson, B.Y., Siggeirsdottir, K., Eiriksdottir, G., Gudnason, V., Lang, T.F., 2013. Effect of finite element model loading condition on fracture risk assessment in men and women: The AGES-Reykjavik study. Bone 57, 18–29. https://doi.org/10.1016/j.bone.2013.07.028

Klingner, B.M., Shewchuk, J.R., 2008. Aggressive Tetrahedral Mesh Improvement, in: Brewer, M.L., Marcum, D. (Eds.), Proceedings of the 16th International Meshing Roundtable. Springer Berlin Heidelberg, pp. 3–23.

Knupp, P., 2001. Algebraic Mesh Quality Metrics. SIAM J. Sci. Comput. 23, 193–218. https://doi.org/10.1137/S1064827500371499

Kopperdahl, D.L., Aspelund, T., Hoffmann, P.F., Sigurdsson, S., Siggeirsdottir, K., Harris, T.B., Gudnason, V., Keaveny, T.M., 2014. Assessment of incident spine and hip fractures in women and men using finite element analysis of CT scans. J. Bone Miner. Res. 29, 570–580. https://doi.org/10.1002/jbmr.2069

Leong, N.L., Anderson, M.E., Gebhardt, M.C., Snyder, B.D., 2010. Computed Tomography-Based Structural Analysis for Predicting Fracture Risk in Children with Benign Skeletal Neoplasms. J. Bone Joint Surg. Am. 92, 1827–1833. https://doi.org/10.2106/JBJS.I.00871

Logan, D.L., 2012. A first course in the finite element method, 5th ed. ed. Cengage Learning, Stamford, CT.

Lund, M.E., de Zee, M., Andersen, M.S., Rasmussen, J., 2012. On validation of multibody musculoskeletal models. Proc. Inst. Mech. Eng. [H] 226, 82–94. https://doi.org/10.1177/0954411911431516

Lynch, M.E., Brooks, D., Mohanan, S., Lee, M.J., Polamraju, P., Dent, K., Bonassar, L.J., van der Meulen, M.C.H., Fischbach, C., 2013. In Vivo Tibial Compression Decreases Osteolysis and Tumor Formation in a Human Metastatic Breast Cancer Model. J. Bone Miner. Res. Off. J. Am. Soc. Bone Miner. Res. 28, 2357–2367. https://doi.org/10.1002/jbmr.1966

Lynch, M.E., Main, R.P., Xu, Q., Walsh, D.J., Schaffler, M.B., Wright, T.M., van der Meulen, M.C.H., 2010. Cancellous bone adaptation to tibial compression is not sex dependent in growing mice. J. Appl. Physiol. 109, 685–691. https://doi.org/10.1152/japplphysiol.00210.2010

Mann, K.A., Lee, J., Arrington, S.A., Damron, T.A., Allen, M.J., 2008. Predicting Distal Femur Bone Strength in a Murine Model of Tumor Osteolysis. Clin. Orthop. 466, 1271–1278. https://doi.org/10.1007/s11999-008-0241-4

Mantyh, P., 2013. Bone cancer pain: causes, consequences, and therapeutic opportunities. Pain 154 Suppl 1, S54-62. https://doi.org/10.1016/j.pain.2013.07.044

Mirels, H., 2003. The Classic: Metastatic Disease in Long Bones A Proposed Scoring System for Diagnosing Impending Pathologic Fractures. Clin. Orthop. 415. https://doi.org/10.1097/01.blo.0000093045.56370.dd

Mundy, G.R., 2002. Metastasis: Metastasis to bone: causes, consequences and therapeutic opportunities. Nat. Rev. Cancer 2, 584–593. https://doi.org/10.1038/nrc867

National Academies of Sciences, E., 2011. Procedures for Verification and Validation of Computer Simulations Used for Roadside Safety Applications. https://doi.org/10.17226/17647

Niebur, G.L., Feldstein, M.J., Yuen, J.C., Chen, T.J., Keaveny, T.M., 2000. High-resolution finite element models with tissue strength asymmetry accurately predict failure of trabecular bone. J. Biomech. 33, 1575–1583. https://doi.org/10.1016/S0021-9290(00)00149-4

Nyman, J.S., Uppuganti, S., Makowski, A.J., Rowland, B.J., Merkel, A.R., Sterling, J.A., Bredbenner, T.L., Perrien, D.S., 2015. Predicting mouse vertebra strength with micro-computed tomography-derived finite element analysis. BoneKEy Rep. 4. https://doi.org/10.1038/bonekey.2015.31

Ottewell, P.D., Wang, N., Brown, H.K., Fowles, C.A., Croucher, P.I., Eaton, C.L., Holen, I., 2015. OPG-Fc inhibits ovariectomy-induced growth of disseminated breast cancer cells in bone. Int. J. Cancer 137, 968–977. https://doi.org/10.1002/ijc.29439

Ottewell, P.D., Wang, N., Brown, H.K., Reeves, K.J., Fowles, C.A., Croucher, P.I., Eaton, C.L., Holen, I., 2014. Zoledronic Acid Has Differential Antitumor Activity in the Pre- and Postmenopausal Bone Microenvironment In Vivo. Clin. Cancer Res. 20, 2922–2932. https://doi.org/10.1158/1078-0432.CCR-13-1246

Ottewell, P.D., Woodward, J.K., Lefley, D.V., Evans, C.A., Coleman, R.E., Holen, I., 2009. Anticancer mechanisms of doxorubicin and zoledronic acid in breast cancer tumor growth in bone. Mol. Cancer Ther. 8, 2821–2832. https://doi.org/10.1158/1535-7163.MCT-09-0462

Patel, T.K., Brodt, M.D., Silva, M.J., 2014. Experimental and finite element analysis of strains induced by axial tibial compression in young-adult and old female C57Bl/6 mice. J. Biomech. 47, 451–457. https://doi.org/10.1016/j.jbiomech.2013.10.052

Pereira, A.F., Javaheri, B., Pitsillides, A.A., Shefelbine, S.J., 2015. Predicting cortical bone adaptation to axial loading in the mouse tibia. J. R. Soc. Interface 12. https://doi.org/10.1098/rsif.2015.0590

Pistoia, W., van Rietbergen, B., Lochmüller, E.-M., Lill, C.A., Eckstein, F., Rüegsegger, P., 2002. Estimation of distal radius failure load with micro-finite element analysis models based on three-dimensional peripheral quantitative computed tomography images. Bone 30, 842–848. https://doi.org/10.1016/S8756-3282(02)00736-6

Prasad, J., Wiater, B.P., Nork, S.E., Bain, S.D., Gross, T.S., 2010. Characterizing gait induced normal strains in a murine tibia cortical bone defect model. J. Biomech. 43, 2765–2770. https://doi.org/10.1016/j.jbiomech.2010.06.030

Quenneville, C.E., Dunning, C.E., 2011. Development of a finite element model of the tibia for short-duration high-force axial impact loading. Comput. Methods Biomech. Biomed. Engin. 14, 205–212. https://doi.org/10.1080/10255842.2010.548324

Razi, H., Birkhold, A.I., Zaslansky, P., Weinkamer, R., Duda, G.N., Willie, B.M., Checa, S., 2015. Skeletal maturity leads to a reduction in the strain magnitudes induced within the bone: A murine tibia study. Acta Biomater. 13, 301–310. https://doi.org/10.1016/j.actbio.2014.11.021

Renders, G.A.P., Mulder, L., Langenbach, G.E.J., van Ruijven, L.J., van Eijden, T.M.G.J., 2008. Biomechanical effect of mineral heterogeneity in trabecular bone. J. Biomech. 41, 2793–2798. https://doi.org/10.1016/j.jbiomech.2008.07.009

Robling, A.G., Burr, D.B., Turner, C.H., 2001. Skeletal loading in animals. J. Musculoskelet. Neuronal Interact. 1, 249–262.

Rogge, R.D., Adams, B.D., Goel, V.K., 2002. An analysis of bone stresses and fixation stability using a finite element model of simulated distal radius fractures. J. Hand Surg. 27, 86–92. https://doi.org/10.1053/jhsu.2002.29485

Scheid, V., Buzdar, A.U., Smith, T.L., Hortobagyi, G.N., 1986. Clinical course of breast cancer patients with osseous metastasis treated with combination chemotherapy. Cancer 58, 2589–2593. https://doi.org/10.1002/1097-0142(19861215)58:12<2589::AID-CNCR2820581206>3.0.CO;2-O

Slosky, L.M., Largent-Milnes, T.M., Vanderah, T.W., 2015a. Use of Animal Models in Understanding Cancer-induced Bone Pain. Cancer Growth Metastasis 8, 47–62. https://doi.org/10.4137/CGM.S21215

Slosky, L.M., Largent-Milnes, T.M., Vanderah, T.W., 2015b. Use of Animal Models in Understanding Cancer-induced Bone Pain. Cancer Growth Metastasis 8, 47–62. https://doi.org/10.4137/CGM.S21215

Spatz, J.M., Ellman, R., Cloutier, A.M., Louis, L., van Vliet, M., Suva, L.J., Dwyer, D., Stolina, M., Ke, H.Z., Bouxsein, M.L., 2013. Sclerostin Antibody Inhibits Skeletal Deterioration Due to Reduced Mechanical Loading. J. Bone Miner. Res. Off. J. Am. Soc. Bone Miner. Res. 28, 865–874. https://doi.org/10.1002/jbmr.1807

Tanck, E., van Aken, J.B., van der Linden, Y.M., Schreuder, H.W.B., Binkowski, M., Huizenga, H., Verdonschot, N., 2009. Pathological fracture prediction in patients with metastatic lesions can be improved with quantitative computed tomography based computer models. Bone 45, 777–783. https://doi.org/10.1016/j.bone.2009.06.009

Turner, C.H., Burr, D.B., 1993. Basic biomechanical measurements of bone: A tutorial. Bone 14, 595–608. https://doi.org/10.1016/8756-3282(93)90081-K

Urwin, G.H., Percival, R.C., Harris, S., Beneton, M.N., Williams, J.L., Kanis, J.A., 1985. Generalised increase in bone resorption in carcinoma of the prostate. Br. J. Urol. 57, 721–723.

Van der Linden, Y.M., Dijkstra, P.D.S., Kroon, H.M., Lok, J.J., Noordijk, E.M., Leer, J.W.H., Marijnen, C. a. M., 2004. Comparative analysis of risk factors for pathological fracture with femoral metastases. J. Bone Joint Surg. Br. 86, 566–573.

van Rietbergen, B., Ito, K., 2015. A survey of micro-finite element analysis for clinical assessment of bone strength: The first decade. J. Biomech., In Memory of Rik Huiskes 48, 832–841. https://doi.org/10.1016/j.jbiomech.2014.12.024

Verhulp, E., van Rietbergen, B., Huiskes, R., 2006. Comparison of micro-level and continuum-level voxel models of the proximal femur. J. Biomech. 39, 2951–2957. https://doi.org/10.1016/j.jbiomech.2005.10.027

Viceconti, M., Taddei, F., Van Sint Jan, S., Leardini, A., Cristofolini, L., Stea, S., Baruffaldi, F., Baleani, M., 2008. Multiscale modelling of the skeleton for the prediction of the risk of fracture. Clin. Biomech. Bristol Avon 23, 845–852. https://doi.org/10.1016/j.clinbiomech.2008.01.009

Wagner, D.W., Lindsey, D.P., Beaupre, G.S., 2011. Deriving tissue density and elastic modulus from microCT bone scans. Bone 49, 931–938. https://doi.org/10.1016/j.bone.2011.07.021

Wedin, R., Bauer, H.C.F., 2005. Surgical treatment of skeletal metastatic lesions of the proximal femur. J. Bone Joint Surg. Br. 87-B, 1653–1657. https://doi.org/10.1302/0301-620X.87B12.16629

Werbeck, J.L., Thudi, N.K., Martin, C.K., Premanandan, C., Yu, L., Ostrowksi, M.C., Rosol, T.J., 2014. Tumor Microenvironment Regulates Metastasis and Metastasis Genes of Mouse MMTV-PymT Mammary Cancer Cells In Vivo. Vet. Pathol. 51, 868–881. https://doi.org/10.1177/0300985813505116

Wernle, J.D., Damron, T.A., Allen, M.J., Mann, K.A., 2010. Local irradiation alters bone morphology and increases bone fragility in a mouse model. J. Biomech. 43, 2738–2746. https://doi.org/10.1016/j.jbiomech.2010.06.017

Wong, M., Pavlakis, N., 2011. Optimal management of bone metastases in breast cancer patients. Breast Cancer Targets Ther. 3, 35–60. https://doi.org/10.2147/BCTT.S6655

Wright, L.E., Ottewell, P.D., Rucci, N., Peyruchaud, O., Pagnotti, G.M., Chiechi, A., Buijs, J.T., Sterling, J.A., 2016. Murine models of breast cancer bone metastasis. Bonekey Rep. 5, UNSP 804. https://doi.org/10.1038/bonekey.2016.31

Yang, H., Butz, K.D., Duffy, D., Niebur, G.L., Nauman, E.A., Main, R.P., 2014. Characterization of cancellous and cortical bone strain in the in vivo mouse tibial loading model using microCT-based finite element analysis. Bone 66, 131–139. https://doi.org/10.1016/j.bone.2014.05.019

Yang, X., Matsuda, K., Bialek, P., Jacquot, S., Masuoka, H.C., Schinke, T., Li, L., Brancorsini, S., Sassone-Corsi, P., Townes, T.M., Hanauer, A., Karsenty, G., 2004. ATF4 Is a Substrate of RSK2 and an Essential Regulator of Osteoblast Biology: Implication for Coffin-Lowry Syndrome. Cell 117, 387–398. https://doi.org/10.1016/S0092-8674(04)00344-7

Yoneda, T., Sasaki, A., Mundy, G.R., 1994. Osteolytic bone metastasis in breast cancer. Breast Cancer Res. Treat. 32, 73–84.

Zapata, E., Rongieras, F., Pialat, J.-B., Follet, H., Mitton, D., 2017. An ex vivo experiment to reproduce a forward fall leading to fractured and non-fractured radii. J. Biomech. 63, 174–178. https://doi.org/10.1016/j.jbiomech.2017.08.013

Zysset, P., Qin, L., Lang, T., Khosla, S., Leslie, W.D., Shepherd, J.A., Schousboe, J.T., Engelke, K., 2015. Clinical Use of Quantitative Computed Tomography-Based Finite Element Analysis of the Hip and Spine in the Management of Osteoporosis in Adults: the 2015 ISCD Official Positions-Part

II. J. Clin. Densitom. Off. J. Int. Soc. Clin. Densitom. 18, 359–392. https://doi.org/10.1016/j.jocd.2015.06.011

Zysset, P.K., Dall'Ara, E., Varga, P., Pahr, D.H., 2013. Finite element analysis for prediction of bone strength. BoneKEy Rep. 2. https://doi.org/10.1038/bonekey.2013.120

R 3.5.1, R Development Core Team (2005). R: A language and environment for statistical computing. R Foundation for Statistical Computing, Vienna, Austria. ISBN 3-900051-07-0, URL: http://www.R-project.org